8-21-2014

Metabolism-oriented Lead Optimization of Propargyl-linked DHFR Inhibitors

Wangda Zhou
University of Connecticut - Storrs, wangda.zhou@uconn.edu

Metabolism-oriented Lead Optimization of Propargyl-linked DHFR Inhibitors

Wangda Zhou, Ph.D.

University of Connecticut, 2014

Dihydrofolate reductase (DHFR), a key enzyme within folate biosynthetic pathway, has been a popular drug target for over six decades. Trimethoprim (TMP) is the only FDA approved antibacterial DHFR inhibitor and remains clinically important. However, acquired resistance by point mutations and natural enzymatic insensitivity limit its use.

A library of novel propargyl-linked antifolates targeting DHFR from MSRA, *Candida* and *Klebsiella* species was developed. Early lead propargyl-linked antifolates were proven potent antibacterial and antifungal agents. Much effort was placed on evaluating the metabolism properties. A strategy of incorporating crystallographic insight and experimental evaluation of structure-activity relationships (SAR) to guide new compound generation was explored to optimize the drug likeliness while maintaining high antimicrobial potency. Exciting compounds with excellent antibacterial activity (MIC = 0.02 μg/mL against MRSA), moderate metabolic stability ($t_{1/2}$ = 99 min), low CYP inhibition (IC_{50} > 50 μM against CYP3A4 and CYP2D6) were designed and generated. These studies will lead to identification of promising candidate compounds that would be ready for further translational development.

Metabolism-oriented Lead Optimization of Propargyl-linked DHFR Inhibitors

Wangda Zhou

B.S., Fudan University, 2006

M.S., Georgia State University, 2009

A Dissertation

Submitted in Partial Fulfillment of the

Requirements for the Degree of

Doctor of Philosophy

University of Connecticut

2014

APPROVAL PAGE

Doctor of Philosophy Dissertation

Metabolism-oriented Lead Optimization of Propargyl-linked DHFR Inhibitors

Presented by

Wangda Zhou, M.S.

Major Advisor_____

Amy Anderson

Associate Advisor_____

Dennis Wright

Associate Advisor_____

Jose Manautou

University of Connecticut

2014

I dedicate this dissertation to my parents Xingdong and Guoying, my daughter Abigail and my beloved wife Weiling.

My parents: thank you for always believing in me and your unconditional support;

Abby: wish I can always be there for you;

Vivi: it is great to have you in my life, thank you for your love and support;

Table of Contents

List of common Abbreviations

ADME	Absorption, disposition, metabolism and excretion
AUC	Area under curve
CID	Collision induced dissociation
CYP450	Cytochrome P450s
DHF	Dihydrofolate
DHFR	Dihydrofolate reductase
DMPK	Drug metabolism and pharmacokinetics
dTMP	Deoxythymidine monophosphate
HLM	Human liver microsomes
HPMC	Hydroxypropyl methylcellulose
IC_{50}	Inhibition concentration at 50%
MIC	Minimum inhibition concentration
MLM	Mouse liver microsomes
MRSA	Methicillin-resistance *Staphylococcus aureus*
NADPH	Nicotinamide adenosine dinucleotide phosphate
SAR	Structure activity relationships
SPR	Structure property relationships
TMP	Trimethoprim
UCP	University of Connecticut patent for propargyl-linked DHFR inhibitors

Chapter 1

DHFR inhibitors as antimicrobial agents

1.1. Introduction

The folate biosynthetic pathway is responsible for the generation of deoxythymidine monophosphate (dTMP), purine nucleotides and the amino acids methionine and histidine in many species [1]. Inhibition of the folate pathway interrupts DNA replication and suppresses cell proliferation. Essential enzymes in this pathway have been popular drug targets since the 1930s [2].

1.2. DHFR and folate biosynthesis

Human folate biosynthesis starts from folic acid dietary uptake. Once consumed, folic acid is reduced to dihydrofolate (DHF) and subsequently tetrahydrofolate (THF) by dihydrofolate reductase (DHFR), coupled with oxidization of cofactor NADPH. With the presence of serine, THF is then converted to 5, 10-methylene tetrahydrofolate, which acts as C_1 donor for dTMP, purines, histidine and methionine generation (Fig. 1).

In contrast, bacteria, fungi and protozoa cannot sufficiently obtain environmental folate. These organisms pose a multi-step endogenous folate synthesis process which converts readily available guanosine triphosphate (GTP) to DHF. With the *de novo* DHF biosynthesis, nucleotides and amino acids are then generated with the same enzymatic process as in humans.

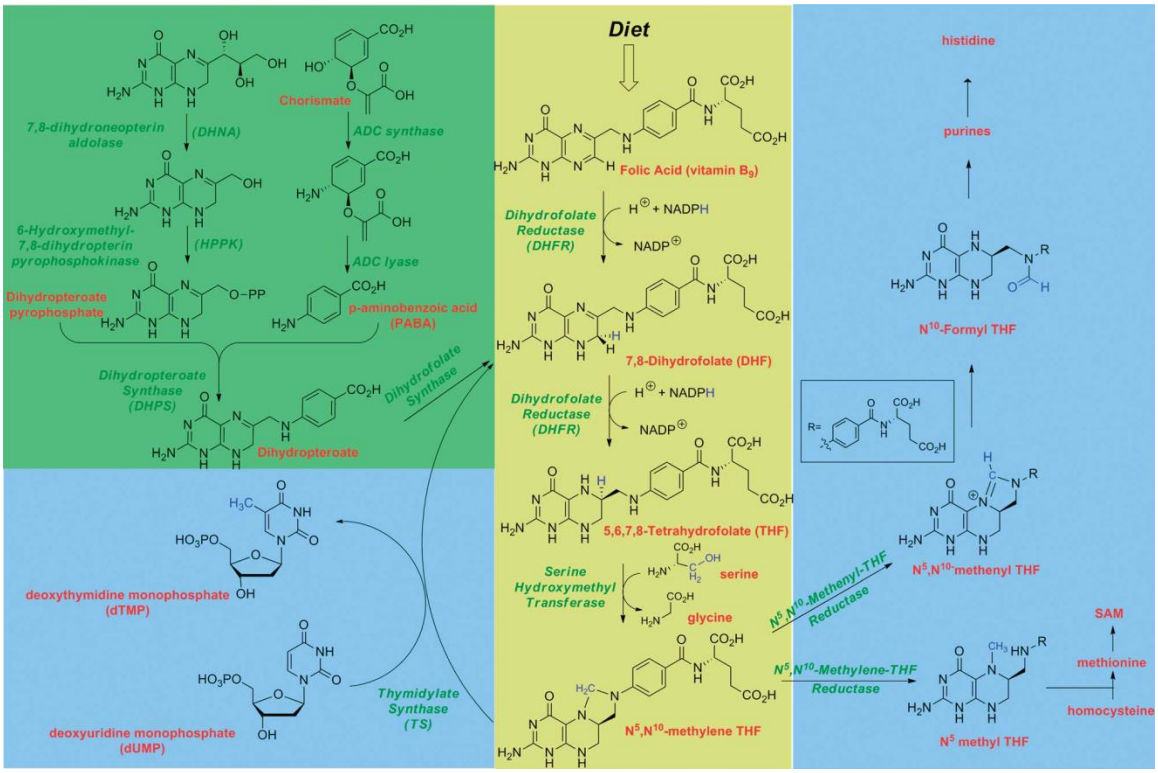

Figure 1. Folate biosynthetic pathway. The bacterial, fungal and protozoal specific biosynthetic reactions are highlighted in green while the essential pathway in all species is shown in yellow. Products of the path are shown in blue.

1.3. DHFR inhibitors and TMP resistance

For over six decades, DHFR inhibitors have been successfully used as antiprotozoal (cycloguanil, pyrimethamine), anticancer (methotrexate) and antibacterial (trimethoprim) therapeutics [3-5]. Despite the great success of DHFR inhibitors, trimethoprim (TMP) is the only FDA approved antibacterial antifolate and remains clinically important. However, acquired resistance by point mutations and natural resistant strains limit its use.

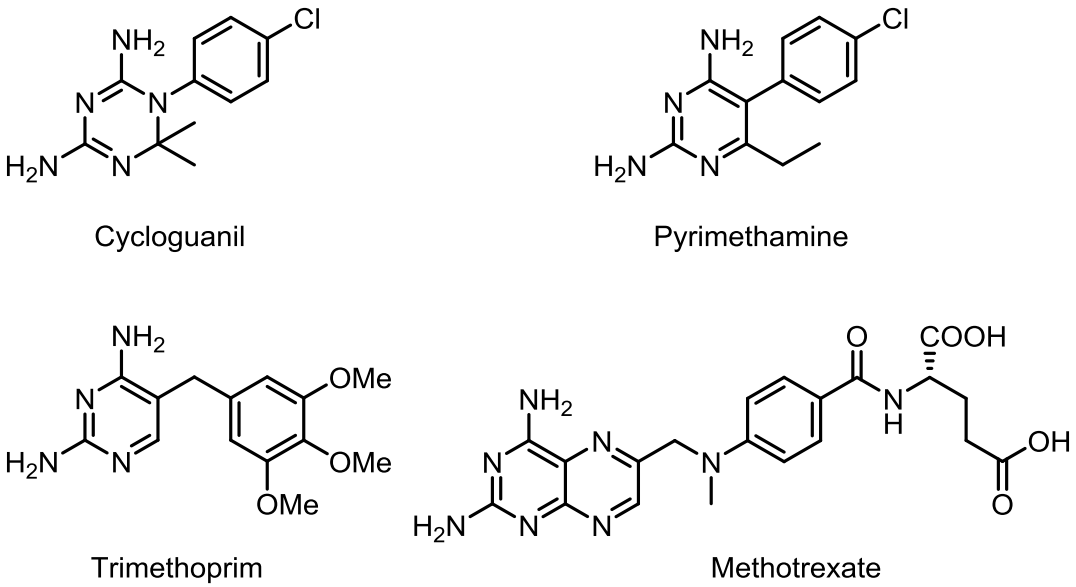

Figure 2. Structures of clinically used DHFR inhibitors

1.3.1 TMP resistance in MRSA

Staphylococcus aureus is a leading cause of bloodstream infections (BSI), skin and soft tissue infections (SSTI) and pneumonia worldwide [6]. Shortly after methicillin was introduced for *S. aureus* treatment, the first methicillin-resistant *Staphylococcus aureus* (MRSA) isolate was reported in England in 1961[7]. MRSA appeared in the US in 1968 [4] and had emerged by the early 1980s [8]. While MRSA remains a leading cause of hospital acquired infections, the incidence of community-acquired MRSA (CA-MRSA) has also rapidly increased since 1997, reaching over 14 million cases by 2005[9]. CA-MRSA isolates are likely susceptible to Bactrim (a TMP and sulfamethoxazole combination) [10], which is recommended as a first-line treatment for outpatient SSTIs [11-14].

TMP resistance in *S. aureus* was first found to be mediated by plasmid pSK1 in Australia [15]. The pSK1 plasmid was later shown to be encoded with the highly resistant type S1 DHFR [16]. Three years later, a similar TMP-resistant plasmid pABU1 was found in Switzerland [17]. The worldwide dissemination was explained through the spread of transposon Tn4003 [17-18]. Investigation of an international collection of strains suggested that 28% of MRSA strains are TMP-resistant [19]. Comparing to high-level resistance mediated transposons, the more common form of resistance involves mutations in the chromosomal DHFR gene, yielding intermediate levels of resistance (~250-fold). A common amino acid mutation from Phe to Tyr at position 98, which creates a greater than 70-fold loss of affinity for TMP, is believed to be the origin of TMP resistance in *S. aureus* [20]. High-resolution crystal structures of wild-type and F98Y mutant *S. aureus* DHFR bound to ligands explain that the decreased TMP binding may be due to the loss of conserved hydrogen bonding [20] or the displacement of cofactor NADPH [21].

1.3.2 TMP resistance in *E. coli*

Urinary tract infections (UTIs), primarily caused by gram-negative Enterobacteriaceae (for example *Escherichia coli*) [22], are among the most common bacterial infections in the US [23]. TMP-SMX is recommended as first-line medication for UTIs [24]. However, TMP-SMX resistance in *E. coli* substantially increased from 17.9% in 2000 to 24.2% in 2010 [25], making this combination therapy a poor choice for pediatric UTIs in many geographical areas [26]. TMP resistance in *E. coli* is caused by the acquisition of

modified dfr genes that carry out the catalytic function but are naturally resistant to the drug. About twenty different resistant dfr genes, found in Class 1 and Class 2 integrons [27], have been isolated [28-29]. dfrA1 and dfrA17 are found to be the most prevalent in clinical isolates [30]. The worldwide dissemination of TMP resistance in *E. coli* is primarily caused by horizontal gene transfer, while clonal expansion only plays a minor role [31-32].

1.3.3 Species with a natural insensitivity to TMP

Interestingly, despite the conservation of the sequence of DHFR over a long evolutionary period, TMP is selective for certain bacteria such as *S. aureus* and *E. coli* but does not inhibit the DHFR enzymes of many other important pathogenic bacteria. While its inability to inhibit human DHFR is an advantage in its use as an antimicrobial agent, it also does not inhibit DHFR from several pathogenic eukaryotic species such as fungi or protozoa, limiting its range of coverage.

Cryptosporidium spp, a parasitic protozoan with few effective therapeutics, can cause diarrhea lasting weeks in immunocompetent patients or severe enteritis in children, elderly and immunocompromised patients [33]. *Cryptosporidium hominis* is naturally resistant to TMP, exhibiting weak inhibition of the DHFR enzyme (IC_{50} = 14 μM) [34]. *Bacillus anthracis*, the bacterium responsible for anthrax, is one of the most serious organisms used as a biological weapon [35]. *B. anthracis* is also naturally resistant to TMP due to minimal inhibition of DHFR (IC_{50} = 77 μM) [36]. Candida species are the fourth ranked nosocomial bloodstream pathogen in the US and have the highest crude

mortality at 40% [37]. Among all the hospital-acquired BSI pathogenic *Candida spp, C. albicans* comprised 45% of the isolates, followed by *C. glabrata* at 24% [38]. TMP is an ineffective antifungal agent owing to lack of enzymatic inhibition (IC_{50} = 42 μM) for *C. albicans* [39] and (IC_{50}= 7 μM) for *C. glabrata* [40].

1.4. Conclusions

DHFR as one of the key enzymes from folate biosynthetic pathway has been an important drug target for more than sixty years. TMP, the sole FDA approved antibacterial antifolate, remains clinically important. Natural enzyme insensitivity and acquired resistance limit TMP usage. During the past two decades, many attempts have been made to develop TMP derivatives that are effective against TMP-resistant species and naturally insensitive species [41-44]. Novel antimicrobial agents targeting DHFR from TMP resistant strains would provide a much needed therapeutic fighting against infectious diseases.

1.5. References

1. Anderson, A.C., *Targeting DHFR in parasitic protozoa.* Drug Discov Today, 2005. **10**(2): p. 121-8.
2. Domagk, G., *A contribution to the chemotherapy of bacterial infections.* Deutsche medizinischbe Wochenschrift, 1935. **61**: p. 250-253.
3. Wilson, T. and J.F. Edeson, *Treatment of acute malaria with pyrimethamine.* Br Med J, 1953. **1**(4804): p. 253-5.
4. Bertino, J.R., *The Mechanism of Action of the Folate Antagonists in Man.* Cancer Res, 1963. **23**: p. 1286-306.
5. Gruneberg, R.N. and R. Kolbe, *Trimethoprim in the treatment of urinary infections in hospital.* Br Med J, 1969. **1**(5643): p. 545-7.
6. Diekema, D.J., et al., *Survey of infections due to Staphylococcus species: frequency of occurrence and antimicrobial susceptibility of isolates collected in the United States, Canada, Latin America, Europe, and the Western Pacific region for the SENTRY*

Antimicrobial Surveillance Program, 1997-1999. Clin Infect Dis, 2001. **32 Suppl 2**: p. S114-32.
7. Jevons., M.P., *"Celbenin" -resistant Staphylococci.* British Medical Journal, 1961.
8. Boyce, J.M. and W.A. Causey, *Increasing occurrence of methicillin-resistant Staphylococcus aureus in the United States.* Infect Control, 1982. **3**(5): p. 377-83.
9. Hersh, A.L., et al., *National trends in ambulatory visits and antibiotic prescribing for skin and soft-tissue infections.* Arch Intern Med, 2008. **168**(14): p. 1585-91.
10. Moran, G.J., et al., *Methicillin-resistant S. aureus infections among patients in the emergency department.* N Engl J Med, 2006. **355**(7): p. 666-74.
11. Stevens, D.L., et al., *Practice guidelines for the diagnosis and management of skin and soft-tissue infections.* Clin Infect Dis, 2005. **41**(10): p. 1373-406.
12. Sabol, K.E., K.L. Echevarria, and J.S. Lewis, 2nd, *Community-associated methicillin-resistant Staphylococcus aureus: new bug, old drugs.* Ann Pharmacother, 2006. **40**(6): p. 1125-33.
13. Liu, C., et al., *Clinical practice guidelines by the infectious diseases society of america for the treatment of methicillin-resistant Staphylococcus aureus infections in adults and children: executive summary.* Clin Infect Dis, 2011. **52**(3): p. 285-92.
14. Diaz, E., et al., *Is methicillin-resistant Staphylococcus aureus pneumonia epidemiology and sensitivity changing?* Am J Med Sci, 2012. **343**(3): p. 196-8.
15. Lyon, B.R., J.W. May, and R.A. Skurray, *Tn4001: a gentamicin and kanamycin resistance transposon in Staphylococcus aureus.* Mol Gen Genet, 1984. **193**(3): p. 554-6.
16. Young, H.K., R.A. Skurray, and S.G. Amyes, *Plasmid-mediated trimethoprim-resistance in Staphylococcus aureus. Characterization of the first gram-positive plasmid dihydrofolate reductase (type S1).* Biochem J, 1987. **243**(1): p. 309-12.
17. Burdeska, A., et al., *Identical genes for trimethoprim-resistant dihydrofolate reductase from Staphylococcus aureus in Australia and central Europe.* FEBS Lett, 1990. **266**(1-2): p. 159-62.
18. Dale, G.E., et al., *Characterization of the gene for the chromosomal dihydrofolate reductase (DHFR) of Staphylococcus epidermidis ATCC 14990: the origin of the trimethoprim-resistant S1 DHFR from Staphylococcus aureus?* J Bacteriol, 1995. **177**(11): p. 2965-70.
19. Huovinen, P., et al., *Trimethoprim and sulfonamide resistance.* Antimicrob Agents Chemother, 1995. **39**(2): p. 279-89.
20. Dale, G.E., et al., *A single amino acid substitution in Staphylococcus aureus dihydrofolate reductase determines trimethoprim resistance.* J Mol Biol, 1997. **266**(1): p. 23-30.
21. Frey, K.M., et al., *Crystal structures of wild-type and mutant methicillin-resistant Staphylococcus aureus dihydrofolate reductase reveal an alternate conformation of NADPH that may be linked to trimethoprim resistance.* J Mol Biol, 2009. **387**(5): p. 1298-308.
22. Gupta, K., et al., *International clinical practice guidelines for the treatment of acute uncomplicated cystitis and pyelonephritis in women: A 2010 update by the Infectious Diseases Society of America and the European Society for Microbiology and Infectious Diseases.* Clin Infect Dis, 2011. **52**(5): p. e103-20.
23. Warren, J.W., et al., *Guidelines for antimicrobial treatment of uncomplicated acute bacterial cystitis and acute pyelonephritis in women. Infectious Diseases Society of America (IDSA).* Clin Infect Dis, 1999. **29**(4): p. 745-58.
24. Stamm, W.E., *Estrogens and urinary-tract infection.* J Infect Dis, 2007. **195**(5): p. 623-4.

25. Sanchez, G.V., et al., *In vitro antimicrobial resistance of urinary Escherichia coli isolates among U.S. outpatients from 2000 to 2010.* Antimicrob Agents Chemother, 2012. **56**(4): p. 2181-3.
26. Edlin, R.S., et al., *Antibiotic resistance patterns of outpatient pediatric urinary tract infections.* J Urol, 2013. **190**(1): p. 222-7.
27. Brolund, A., et al., *Molecular characterisation of trimethoprim resistance in Escherichia coli and Klebsiella pneumoniae during a two year intervention on trimethoprim use.* PLoS One, 2010. **5**(2): p. e9233.
28. Skold, O., *Resistance to trimethoprim and sulfonamides.* Vet Res, 2001. **32**(3-4): p. 261-73.
29. White, P.A., C.J. McIver, and W.D. Rawlinson, *Integrons and gene cassettes in the enterobacteriaceae.* Antimicrob Agents Chemother, 2001. **45**(9): p. 2658-61.
30. Seputiene, V., et al., *Prevalence of trimethoprim resistance genes in Escherichia coli isolates of human and animal origin in Lithuania.* J Med Microbiol, 2010. **59**(Pt 3): p. 315-22.
31. Blahna, M.T., et al., *The role of horizontal gene transfer in the spread of trimethoprim-sulfamethoxazole resistance among uropathogenic Escherichia coli in Europe and Canada.* J Antimicrob Chemother, 2006. **57**(4): p. 666-72.
32. Landgren, M., et al., *Diversity among 2481 Escherichia coli from women with community-acquired lower urinary tract infections in 17 countries.* J Antimicrob Chemother, 2005. **55**(6): p. 928-37.
33. Neill, M.A., et al., *Cryptosporidiosis: an unrecognized cause of diarrhea in elderly hospitalized patients.* Clin Infect Dis, 1996. **22**(1): p. 168-70.
34. Pelphrey, P.M., et al., *Highly efficient ligands for dihydrofolate reductase from Cryptosporidium hominis and Toxoplasma gondii inspired by structural analysis.* J Med Chem, 2007. **50**(5): p. 940-50.
35. Inglesby, T.V., et al., *Anthrax as a biological weapon, 2002: updated recommendations for management.* JAMA, 2002. **287**(17): p. 2236-52.
36. Barrow, E.W., P.C. Bourne, and W.W. Barrow, *Functional cloning of Bacillus anthracis dihydrofolate reductase and confirmation of natural resistance to trimethoprim.* Antimicrob Agents Chemother, 2004. **48**(12): p. 4643-9.
37. Edmond, M.B., et al., *Nosocomial bloodstream infections in United States hospitals: a three-year analysis.* Clin Infect Dis, 1999. **29**(2): p. 239-44.
38. Hajjeh, R.A., et al., *Incidence of bloodstream infections due to Candida species and in vitro susceptibilities of isolates collected from 1998 to 2000 in a population-based active surveillance program.* J Clin Microbiol, 2004. **42**(4): p. 1519-27.
39. Paulsen, J.L., et al., *In vitro biological activity and structural analysis of 2,4-diamino-5-(2'-arylpropargyl)pyrimidine inhibitors of Candida albicans.* Bioorg Med Chem, 2009. **17**(14): p. 4866-72.
40. Liu, J., et al., *Towards new antifolates targeting eukaryotic opportunistic infections.* Eukaryot Cell, 2009. **8**(4): p. 483-6.
41. Locher, H.H., et al., *Antibacterial activities of epiroprim, a new dihydrofolate reductase inhibitor, alone and in combination with dapsone.* Antimicrob Agents Chemother, 1996. **40**(6): p. 1376-81.
42. Hawser, S.P., *Antibacterial drug discovery and development--SRI's 11th Annual Summit.* IDrugs, 2006. **9**(6): p. 390-3.
43. Sincak, C.A. and J.M. Schmidt, *Iclaprim, a novel diaminopyrimidine for the treatment of resistant gram-positive infections.* Ann Pharmacother, 2009. **43**(6): p. 1107-14.

44. Schneider, P., S. Hawser, and K. Islam, *Iclaprim, a novel diaminopyrimidine with potent activity on trimethoprim sensitive and resistant bacteria.* Bioorg Med Chem Lett, 2003. **13**(23): p. 4217-21.

Chapter 2

Development of novel propargyl-based DHFR inhibitors

2.1. Introduction

Over the past several years, a library of novel DHFR inhibitors have been designed and synthesized under a robust collaboration between the laboratories of Drs. Amy Anderson and Dennis Wright. These DHFR inhibitors are characterized by a conserved diaminopyrimidine ring linked through a propargylic spacer to a variable hydrophobic domain. Early lead compounds in this library exhibit promising inhibition of DHFR and antimicrobial activity against *Staphylococcus aureus* [1], *Candida glabrata* [2] and *Candida albicans* [3].

2.2. Development of propargyl-linked antifolates

The need for therapeutic agents against trimethoprim (TMP) insensitive species such as protozoa *Cryptosporidium* and *Toxoplasma* inspired the development of a series of novel DHFR inhibitors that feature an acetylenic linker [4]. Crystallographic insight of DHFR from *Cryptosporidium hominis* and *Toxoplasma gondii* suggested that extended TMP analogues with a three-carbon propargylic linkage between the diaminopyrimidine and phenyl rings should improve ligand and protein interaction. Initial docking of TMP and early propargyl-linked antifolate UCP100A (Fig 1.) into the binding site of *C. hominis* DHFR (ChDHFR) illustrated that with prolonged propargylic linker, trimethoxyphenyl

moiety of UCP100A was deeper positioned into the hydrophobic pocket comparing to TMP.

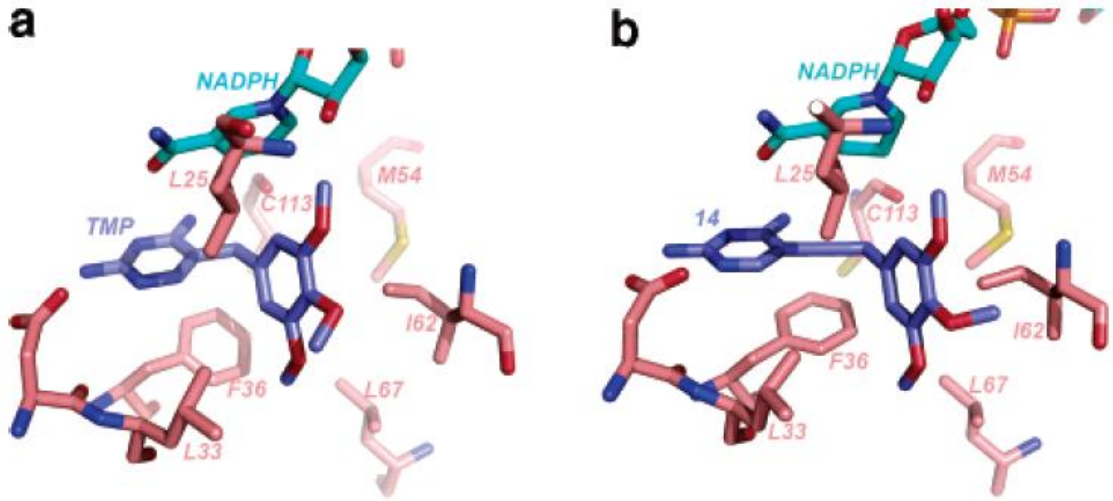

Figure 1. a, TMP docked into the active site of ChDHFR. b, UCP100A docked into the active site of ChDFHR

Experimental analysis of ChDHFR inhibition also confirmed that first generation lead compound UCP111A (IC_{50} = 38 nM) is over 300 folds more potent than TMP (IC_{50}=14 µM) (Scheme 1.). The generation of UCP111D, a lead compound with phenyl substitution at distal position, showed further improved potency with an IC_{50} of 1.8 nM. With this proof of concept, extensive efforts have been made to characterize and optimize propargyl-lined DHFR inhibitors as effective therapeutic agents against *Bacillus anthracis*, *Staphylococcus aureus, Klebsiella* and *Candida* species.

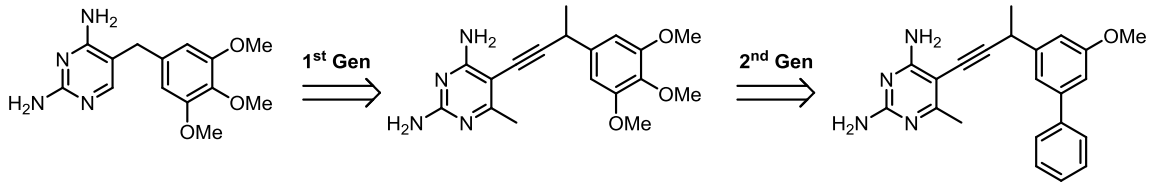

*Ch*DHFR IC_{50}: 14 μM
TMP

*Ch*DHFR IC_{50}: 38 nM
1st Generation
UCP111A

*Ch*DHFR IC_{50}: 1.8 nM
2nd Generation
UCP111D

Scheme 1. Progression of propargyl-linked antifolates effective against ChDHFR

2.3. Evolution of propargyl-based antifolates

The first generation propargyl-linked DHFR inhibitors featuring a pyrimidine ring with methyl or ethyl substituted C6 position and a single substitute benzene ring adjacent to the propargyl position. Lead compounds in this generation exhibited promising enzymatic inhibitory activity, however, they are not active at the cellular level [5]. Crystal structures of ChDHFR complexed with these early propargyl-linked antifolates suggested that potency can be gained by adding hydrophobic interaction with the second hydrophobic pocket [1, 3, 6]. With this hypothesis, the second generation inhibitors with a substituted biphenyl moiety were designed and synthesized.

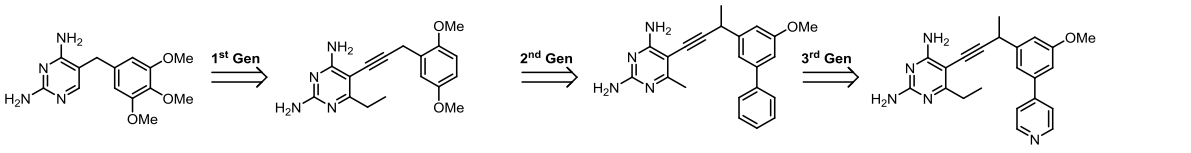

*Sa*DHFR IC_{50}: 23 nM F98Y IC_{50}: 1.7μM
MIC: 625 ng/mL Bactrim^R MIC:1.5 μg/mL
w/SMX 30.5 μg/mL
TMP

*Sa*DHFR IC_{50}: 68 nM F98Y IC_{50}: 0.67μM
Bactrim^R MIC: 312 ng/mL
UCP120B

*Sa*DHFR IC_{50}: 61 nM F98Y IC_{50}: 0.19μM
Bactrim^R MIC: 720 ng/mL
UCP111D

*Sa*DHFR IC_{50}: 19 nM F98Y IC_{50}: 0.17μM
MIC: 78 ng/mL Bactrim^R MIC: 90 ng/mL
UCP1006

Scheme 2. Progression of compounds targeting *S. aureus* DHFR.

These second generation compounds are excellent inhibitors of both TMP-sensitive and resistant DHFR enzymes. Moreover, lead compounds exhibited marked antibacterial [7] and antifungal activity [8]. Nevertheless, with increased molecular weight and hydrophobicity, most compounds in this series have poor water solubility [9]. It is well accepted that water solubility is critical drug likeliness parameter which affects both drug distribution and metabolism [10-11]. Therefore, with the goal to balance the compound polarity and improve water solubility, a series of analogues with heterocycles substituted at para of the adjacent phenyl ring were designed and synthesized as the third generation of inhibitors. Lead compounds in the third generation inhibitors are generally equal or more potent than the biphenyl inhibitors in both enzymatic and cell based inhibitory assays [7, 12]. UCP1006, a key compound in the heterocyclic series, also showed encouraging efficacy against mutant SaDHFR and TMP resistant MRSA stains [13].

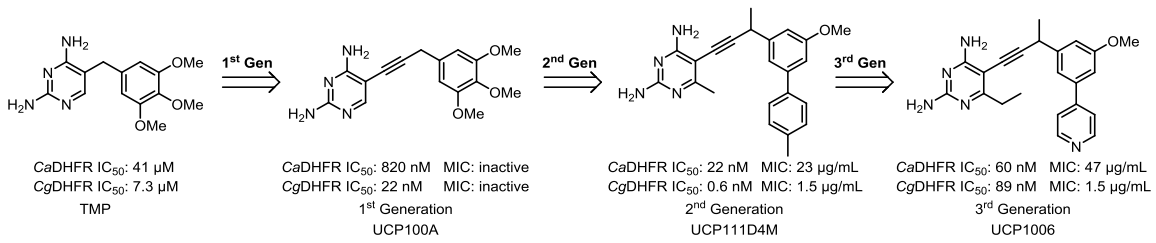

Scheme 3. Compounds evolution against DHFR from *C. albicans* and *C. glabrata*.

2.4. Conclusions

Novel antifolates characterized with a rare acetylenic scaffold targeting TMP insensitive pathogenic DHFR from MRSA, *C. albicans* and *C. glabrata* were developed. Lead

biphenyl series compounds exhibited potent enzymatic inhibition and antiproliferative activity. To improve the water solubility and drug likeliness of these compounds, more polarity balanced heterocyclic compounds were synthesized. Lead compounds in this generation are potent MSRA and fungal inhibitors. To move this drug discovery effort forward, more detailed drug like properties of propargyl-linked antifolates will be explored.

2.5. References

1. Frey, K.M., et al., *Crystal structures of wild-type and mutant methicillin-resistant Staphylococcus aureus dihydrofolate reductase reveal an alternate conformation of NADPH that may be linked to trimethoprim resistance.* J Mol Biol, 2009. **387**(5): p. 1298-308.
2. Liu, J., et al., *Towards new antifolates targeting eukaryotic opportunistic infections.* Eukaryot Cell, 2009. **8**(4): p. 483-6.
3. Paulsen, J.L., et al., *In vitro biological activity and structural analysis of 2,4-diamino-5-(2'-arylpropargyl)pyrimidine inhibitors of Candida albicans.* Bioorg Med Chem, 2009. **17**(14): p. 4866-72.
4. Pelphrey, P.M., et al., *Highly efficient ligands for dihydrofolate reductase from Cryptosporidium hominis and Toxoplasma gondii inspired by structural analysis.* J Med Chem, 2007. **50**(5): p. 940-50.
5. Zhou, W., et al., *Antifolates as effective antimicrobial agents: new generations of trimethoprim analogs.* MedChemComm, 2013.
6. Liu, J., et al., *Probing the active site of Candida glabrata dihydrofolate reductase with high resolution crystal structures and the synthesis of new inhibitors.* Chem Biol Drug Des, 2009. **73**(1): p. 62-74.
7. Viswanathan, K., et al., *Toward new therapeutics for skin and soft tissue infections: propargyl-linked antifolates are potent inhibitors of MRSA and Streptococcus pyogenes.* PLoS One, 2012. **7**(2): p. e29434.
8. Paulsen, J.L., et al., *Structural analysis of the active sites of dihydrofolate reductase from two species of Candida uncovers ligand-induced conformational changes shared among species.* Bioorg Med Chem Lett, 2013. **23**(5): p. 1279-84.
9. Zhou, W., et al., *Acetylenic linkers in lead compounds: a study of the stability of the propargyl-linked antifolates.* Drug Metab Dispos, 2012. **40**(10): p. 2002-8.
10. Wu, C.Y. and L.Z. Benet, *Predicting drug disposition via application of BCS: transport/absorption/ elimination interplay and development of a biopharmaceutics drug disposition classification system.* Pharm Res, 2005. **22**(1): p. 11-23.

11. Benet, L.Z., *The role of BCS (biopharmaceutics classification system) and BDDCS (biopharmaceutics drug disposition classification system) in drug development.* J Pharm Sci, 2013. **102**(1): p. 34-42.
12. N, G.D., et al., *Propargyl-Linked Antifolates are Dual Inhibitors of Candida albicans and Candida glabrata.* J Med Chem, 2014. **57**(6): p. 2643-56.
13. Frey, K.M., et al., *Prospective screening of novel antibacterial inhibitors of dihydrofolate reductase for mutational resistance.* Antimicrob Agents Chemother, 2012. **56**(7): p. 3556-62.

Chapter 3

Initial physicochemical and stability evaluation of DHFR inhibitors

3.1. Introduction

Drug discovery and development has become increasingly risky, costly and time inefficient [1]. Estimates for the average cost and cycle time of bringing a new drug to market is 1.8 billion dollars and 13.5 years [2]. One of the biggest challenges of drug discovery is high attrition rate. In the early 1990s, adverse drug metabolism and pharmacokinetics (DMPK) properties ranked first and accounted for about 40% of all drug attrition [3]. This number dropped to less than 10% in 10 years with early DMPK screening and optimization [4]. Detailed understanding of how structure-property relationships (SPR) relate to major DMPK weaknesses is critical to support lead identification and optimization for pharmacological potency [5].

Drug metabolism research plays a particularly important role in the hit-to-lead stage of drug discovery, where many new chemical entities exhibit poor metabolic stability in liver microsomes [6]. Throughout the early drug discovery stage, *in vitro* drug metabolism assays mainly focus on the role of cytochrome P450s (CYP), which is responsible for about 80% of known oxidative drug metabolism reactions [7]. Microsomal stability assay using liver microsomes is commonly used and recommended to be applied to all discovery compounds as soon as they are synthesized [8]. Quantitative metabolic stability data are often used to evaluate the extent of

metabolism, rank order compounds for *in vivo* studies and prioritize discovery activities [9]. A single-point metabolism assay with 15 min incubation time would allow accurate measurement of highly unstable compounds ($t_{1/2}$ <5 min) with a proper detection upper limit of 30 min [10]. Concerns of microsomal stability decrease at $t_{1/2}$ greater than 30 min. CYP inhibition is the major cause of drug-drug interactions and early CYP inhibition measurement would provide warning of protential safety liability [11]. CYP inhibition data is useful to select lead compounds and develop structure-CYP inhibiton property relationships, which enables the medicinal chemist to overcome CYP inhibition by structural modification [12]. Evaluation of other drug-like properties (permeability, solubility, solution staibliy etc.) should be also considered based on the scafold of a compound series [13].

3.2. Drug-like properties evaluation of propargyl-linked antifolates

3.2.1 Introduction

The novel propargyl-linked antifolates developed in the Anderson/Wright labs are potent antimicrobial against MRSA and *Candida spp* [14-16]. Preliminary physicochemical evaluation suggested that changes in the lead compounds in the biphenyl series greatly increased hydrophobicity and imbalanced the polarity of the molecule. Initial assessment also suggested that these lead compounds have poor water solubility. It is important to understand the detailed physicochemical properties and to examine the drug likeliness of the lead compounds. In this chapter, membrane permeability, kinetic water solubility, solution stability and metabolic stability of lead

propargylic-linked DHFR inhibitors will be described. By incorporating the crystallographic structural insight, lead compounds with better absorption, disposition, metabolism and excretion (ADME) properties that maintain potency will be developed.

3.2.2 Membrane permeability testing of lead compounds

A parallel artificial membrane permeability assay (PAMPA) was used to evaluate the membrane permeability of lead propargyl-linked antifolates [17]. The second generation biphenyl serial propargyl-linked antifolates generally exhibited high hydrophobicity; therefore, compounds with different polarity functional groups (UCP114B, UCP113A and UCP10003) were chosen for PAMPA testing, with TMP and dihydrofolate (DHF) as controls. Compounds UCP1003 and UCP114B, highlighted with propargylic methyl and hydrophobic substitutions at the adjacent phenyl ring, both show high permeability at 45 and 21 $*10^{-6}$ cm/sec (Table 1.), equivalent to 10 and 4.7 fold higher than TMP control, respectively. In contrast, compound UCP113A, characterized with a polar hydroxyl group at the propargyl position, cannot pass through the artificial membrane showing no permeability, similar to the negative control, DHF. Combined with the fact that most potent lead compounds contain a hydrophobic biphenyl or phenyl-heterocyclic system adjacent to acetylenic linker, membrane permeability seems to be a minor ADME weakness for this class of antifolates.

Table 1. Structure and permeability of propargyl-linked antifoltes

Compounds	Structure	Permeability (10^{-6} cm/sec)

UCP114B	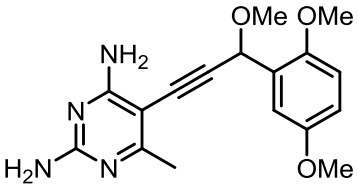	45.0
UCP113A	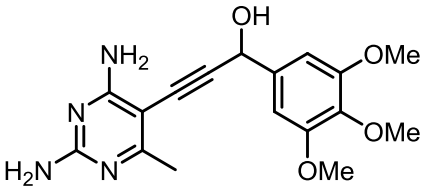	0
UCP1003	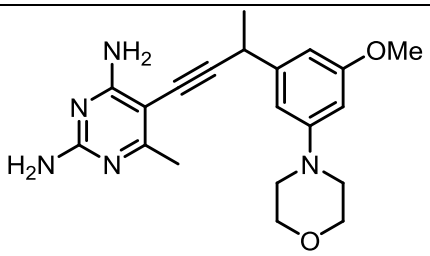	20.9
DHF	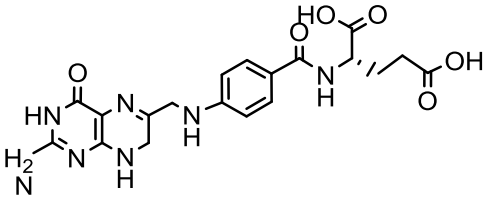	0
TMP	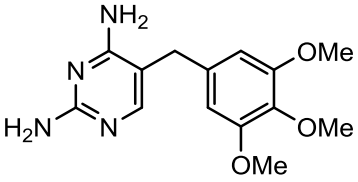	4.5

3.2.3 Kinetic solubility evaluation of biphenyl series inhibitors

Introduction of the biphenyl functional group better accommodated the secondary hydrophobic binding pocket from DHFR and increased potency. However, it also sharply increased the hydrophobicity and decreased water solubility of the compounds. To evaluate and improve the kinetic water solubility without losing potency, the structure-

activity relationship (SAR) of lead compounds were carefully evaluated. A crystal structure of lead biphenyl compound UCP111D bound to *C. glabrata* DHFR (Fig 1.) revealed that the meta and para positions of the distal phenyl ring are generally solvent exposed [18]. Therefore, substitution of more polar functional groups at this area is likely to be tolerated.

a,

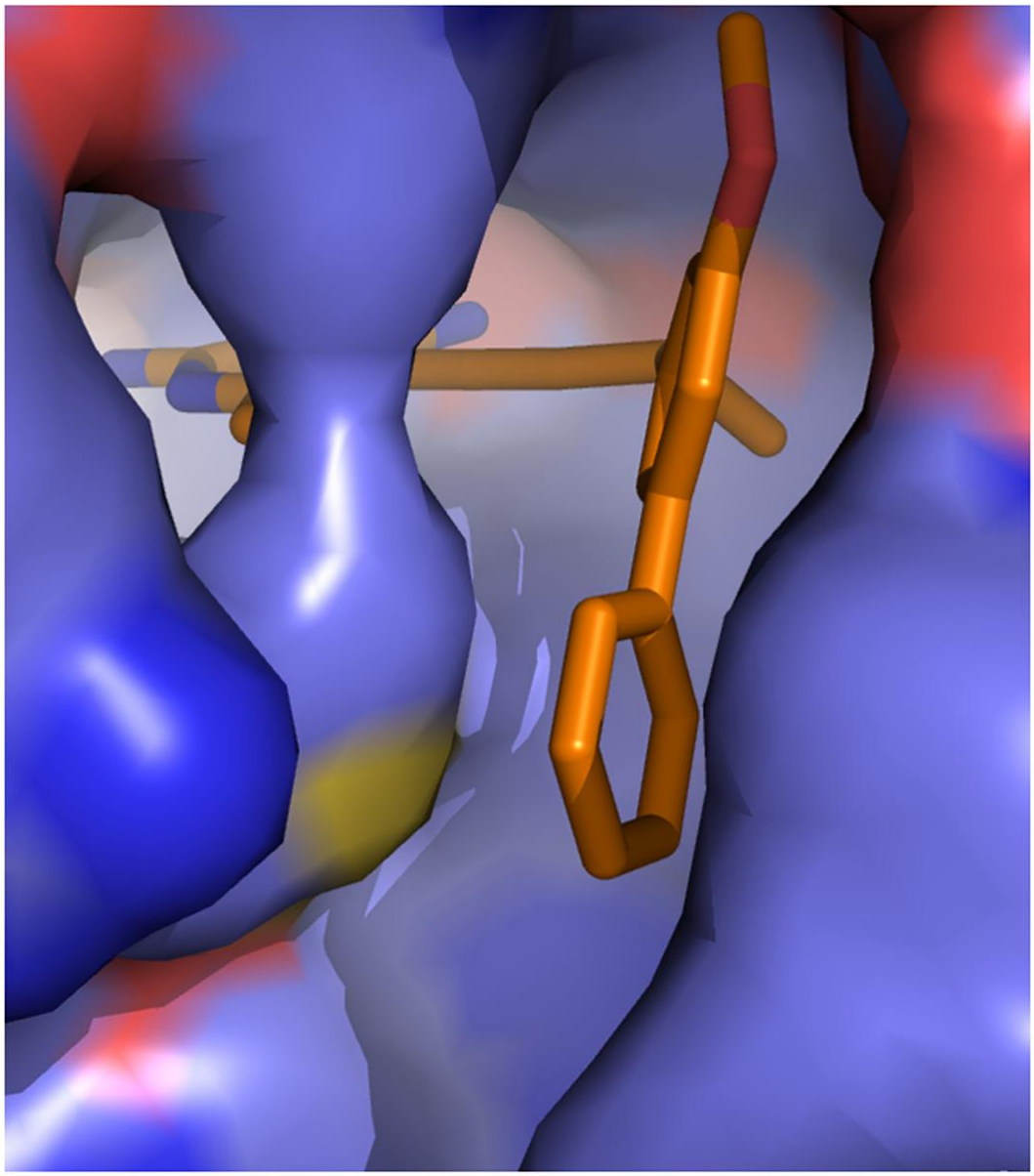

b,

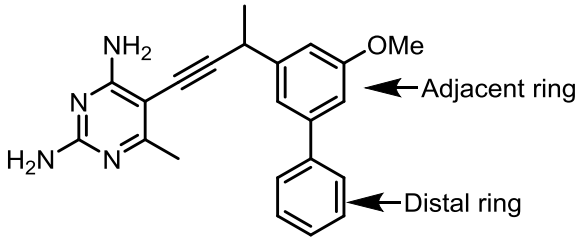

UCP111D

Figure 1. a, UCP111D bound to *C. glabrata* DHFR (from Protein Data Bank identifier 3EEJ), b, and structure of lead compound UCP111D.

With this hypothesis, analogues with six member meta or para heterocyclic rings at the distal position were designed and synthesized. The LogD values at pH7.4 were calculated *in silico* using software ChemAxon and the experimental solubility were also determined.

With a substitution of morpholine or pyridine, UCP1004 and UCP1006 (Fig 2.) exhibited reduced cLogD7.4 values at 2.90 and 3.44, respectively. Experimentally tested kinetic water solubility with the presence of 0.02% hydroxypropyl methylcellulose (HPMC) also confirmed the solubility increase from 20 μg/mL for UCP111D to over 80 μg/mL and 40 μg/mL, respectively. The use of HPMC as a stabilizing agent in solubility testing effectively prevented compound precipitation in solution and eliminated day to day variation. More impressively, both UCP1004 and UCP1006 were potent against *S. aureus* DHFR with IC_{50} values of 19 nM and 26 nM, respectively. In addition, UCP1006 also exhibited excellent antibacterial activity against *S. aureus* with MIC = 0.08 μg/ml and was considered as key lead compound in the heterocyclic series. UCP1004 was not

active against MRSA, likely due to the poor bacterial membrane penetration and therefore not further developed.

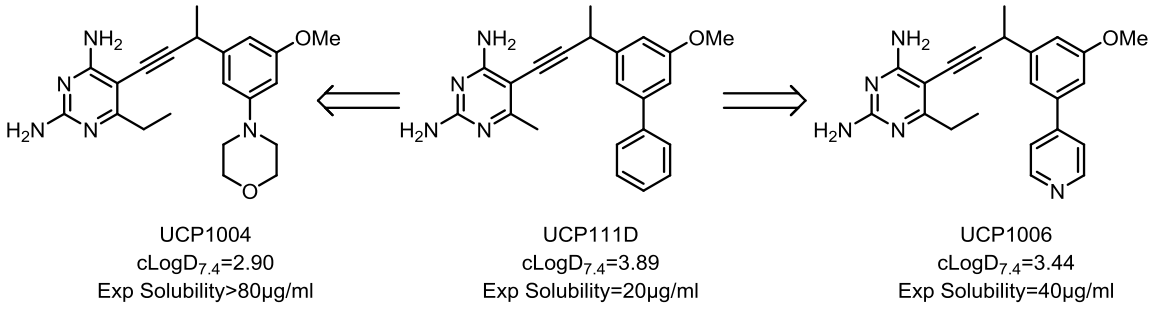

Figure 2. Structures and solubility values of propargyl-linked antifolates

3.2.4 Solution and metabolic stability analysis of lead compounds

To investigate the solution and metabolic stability of the lead propargyl-linked antifolates, compounds UCP1005, UCP1006, UCP1015 and UCP1021 were chosen for analysis. The structure of testing compounds show as figure 3. The testing compounds feature substitution patterns at C_6 position at the pyrimidine ring (R_1, UCP1005 versus UCP1006), propargylic position (R_p, UCP1006 versus UCP1015) and methoxyl substitution position (R_2 and R_3, UCP1015 versus UCP1021).

The set of four testing compounds was first evaluated for solution stability in simulated intestinal fluid (pH7.4), simulated gastric fluid (pH1.2) and water at 37 °C for 24 hours[19]. Testing concentration was 5 μg/mL. The HPLC-UV assessment showed that there is no change in area under curve (AUC) or peak shape after incubation in any of the fluids. This suggested that compounds are stable under all tested conditions.

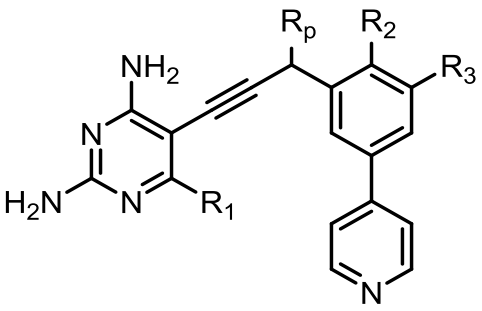

UCP1005: R_1=Me, R_p=Me, R_2=H, R_3=OMe
UCP1006: R_1=Et, R_p=Me, R_2=H, R_3=OMe
UCP1015: R_1=Et, R_p=H, R_2=H, R_3=OMe
UCP1021: R_1=Et, R_p=H, R_2=OMe, R_3=H

Figure 3. Structures of UCP1005, UCP1006, UCP1015 and UCP1021

To evaluate the phase I metabolic stability, all four compounds were incubated for 1 hour with commercially available mouse liver microsomes (MLM) with the presence of an NADPH regenerating system [20]. The percentage of parent compound remaining after incubation relative to the starting concentration was calculated using a standard curve. The metabolic half-life was calculated following a first order kinetics. Compounds UCP1005 and UCP1006, which vary in substitution at the R_1 position both exhibit moderate and similar stability with values of 33 and 29% remaining, respectively. However, analogue UCP1015 with a hydrogen at propargylic position (R_p) showed sharply reduced metabolic stability with only trace amount of parent compound left after 1 hour. Surprisingly, substituting the methoxy group from R_2 to R_3 position (UCP1021) retained the metabolic stability resulting 27% of the parent remaining after incubation. Collectively, it is evident that the metabolic stability of these compounds is

extremely sensitive to substitutions at the propargylic position and the 2' and 3' positions on the adjacent phenyl ring [18].

Table 2. Metabolic half-life of propargyl-linked antifolates

Compound	Percentage Remaining after 1h	Half-Life (min)
UCP1005	34	38
UCP1006	29	34
UCP1015	0	<10
UCP1021	27	31

3.3. Conclusions

Previous studies have validated that propargyl-linked antifolates are potent inhibitors against MRSA, *C. albicans and C. glabrata*. Initial physicochemical property and solution stability evaluation suggested that lead DHFR inhibitors are low to moderately water soluble, highly membrane permeable and stable in various simulated solutions. Metabolic stability studies indicated that some lead propargyl-linked antifolates are quickly metabolized by MLM. In addition, microsomal stability is highly sensitive to substitutions at the propargylic and adjacent phenyl positions. To further understand and potentially improve the ADME properties of propargyl-linked antifolates, primary routes of metabolism will be characterized and strategies to reduce hepatic metabolism will be explored.

3.4. References

1. Orloff, J., et al., *The future of drug development: advancing clinical trial design.* Nat Rev Drug Discov, 2009. **8**(12): p. 949-57.
2. Paul, S.M., et al., *How to improve R&D productivity: the pharmaceutical industry's grand challenge.* Nat Rev Drug Discov, 2010. **9**(3): p. 203-14.
3. Kennedy, T., *Managing the drug discovery/development interface.* Drug Discov Today, 1997. **2**(10): p. 436-444.
4. Kola, I. and J. Landis, *Can the pharmaceutical industry reduce attrition rates?* Nat Rev Drug Discov, 2004. **3**(8): p. 711-5.
5. Ballard, P., et al., *The right compound in the right assay at the right time: an integrated discovery DMPK strategy.* Drug Metab Rev, 2012. **44**(3): p. 224-52.
6. Stepan, A.F., et al., *Evaluating the differences in cycloalkyl ether metabolism using the design parameter "lipophilic metabolism efficiency" (LipMetE) and a matched molecular pairs analysis.* J Med Chem, 2013. **56**(17): p. 6985-90.
7. Wienkers, L.C. and T.G. Heath, *Predicting in vivo drug interactions from in vitro drug discovery data.* Nat Rev Drug Discov, 2005. **4**(10): p. 825-33.
8. Kerns, E.H. and D. Li, *Drug-like Properties: Concepts, Structure Design and Methods.* Academic Press;, 2008.
9. Ansede, J.H. and D.R. Thakker, *High-throughput screening for stability and inhibitory activity of compounds toward cytochrome P450-mediated metabolism.* J Pharm Sci, 2004. **93**(2): p. 239-55.
10. Di, L., et al., *Experimental design on single-time-point high-throughput microsomal stability assay.* J Pharm Sci, 2004. **93**(6): p. 1537-44.
11. Rodrigues, A.D. and J.H. Lin, *Screening of drug candidates for their drug--drug interaction potential.* Curr Opin Chem Biol, 2001. **5**(4): p. 396-401.
12. Kerns, E.H. and L. Di, *Pharmaceutical profiling in drug discovery.* Drug Discov Today, 2003. **8**(7): p. 316-23.
13. Di, L. and E.H. Kerns, *Profiling drug-like properties in discovery research.* Curr Opin Chem Biol, 2003. **7**(3): p. 402-8.
14. Viswanathan, K., et al., *Toward new therapeutics for skin and soft tissue infections: propargyl-linked antifolates are potent inhibitors of MRSA and Streptococcus pyogenes.* PLoS One, 2012. **7**(2): p. e29434.
15. Paulsen, J.L., et al., *Structural analysis of the active sites of dihydrofolate reductase from two species of Candida uncovers ligand-induced conformational changes shared among species.* Bioorg Med Chem Lett, 2013. **23**(5): p. 1279-84.
16. Liu, J., et al., *Towards new antifolates targeting eukaryotic opportunistic infections.* Eukaryot Cell, 2009. **8**(4): p. 483-6.
17. Kansy, M., F. Senner, and K. Gubernator, *Physicochemical high throughput screening: parallel artificial membrane permeation assay in the description of passive absorption processes.* J Med Chem, 1998. **41**(7): p. 1007-10.
18. Zhou, W., et al., *Acetylenic linkers in lead compounds: a study of the stability of the propargyl-linked antifolates.* Drug Metab Dispos, 2012. **40**(10): p. 2002-8.
19. Di, L. and E.H. Kerns, *Solution stability--plasma, gastrointestinal, bioassay.* Curr Drug Metab, 2008. **9**(9): p. 860-8.
20. Di, L., et al., *High throughput microsomal stability assay for insoluble compounds.* Int J Pharm, 2006. **317**(1): p. 54-60.

Chapter 4

Metabolite identification of lead propargyl-linked DHFR inhibitors

4.1. Introduction

Understanding the relation of structure-property relationship (SPR) to major drug metabolism and pharmacokinetics (DMPK) weaknesses is critical to support lead optimization for pharmacological potency [5]. Initial physicochemical and stability assessment of propargyl-linked DHFR inhibitors indicated that some lead compounds are associated with poor metabolic stability. It is important to thoroughly investigate their metabolic routes.

In this chapter, metabolites of lead compounds will be identified and characterized. The distribution of major metabolites will be quantified. The primary metabolites will also be also validated through synthesized standards. SPR between leads and metabolic stability will be carefully analyzed and potent antifolates with increased metabolic stability will be designed, synthesized and evaluated.

4.2. Metabolite identification and characterization

Initial testing for lead compounds UCP1005, UCP1006, UCP1015 and UCP1021 indicated that the metabolic stability of these compounds is sensitive to substitutions at the propargylic and 2' and 3' positions at the adjacent phenyl ring. The same set of four compounds was also chosen for metabolite identification. Testing compounds at 10

μg/mL were incubated with MLM in the presence of a NADPH regenerating system for two hours. The reactions were terminated by ice cold acetonitrile and the proteins were precipitated through centrifugation. Samples were further purified and concentrated with a HLB Oasis column and analyzed with a LC-MS/MS [21]. Mass spectrometry results showed the presence of metabolic products at mass corresponding to M-14, M+16 and M+32 (where M is mono isotopic molecular weight). For all four testing compounds, M-14 metabolites were easily assigned as the *O*-demethylation product at the 2' or 3' position at the adjacent phenyl ring. Assignment of the M+16 metabolites was difficult because of the multiple potential oxidation sites including open aromatic systems, the propargylic position, C6 benzylic position, the acetylenic linker, and the endocyclic basic nitrogens of the pyrimidine and pyridine systems. To assign the major mono-oxidation metabolites, both mass spectrum analysis and organic synthesis approaches were attempted.

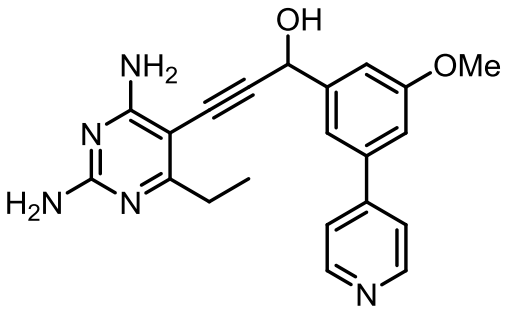

UCP1030

Figure 1. Structure of UCP1030

Compound UCP1015 exhibited sharply reduced metabolic stability compared to UCP1006. The two compounds feature variations of hydrogen and methyl groups at the propargylic position only. Quantification of the major metabolites by area under curve (AUC) from LC-MS spectrum also indicated that the primary mono-oxidation for UCP1015 accounted for 70.5% of the total metabolites, which is significantly higher than the corresponding metabolite of UCP1006 (45.8%). Considering the shorter half life, metabolism of UCP1015 through mono-hydroxylation is predicted to be much more than UCP1006. Incorporating the SAR assessment, the difference in metabolic stability of the two compounds may be explained by the proposal that oxidation of the unsubstituted propargyl carbon (UCP1015) to a secondary alcohol would occur faster than a methyl substituted carbon (UCP1006) to a tertiary alcohol. With this hypothesis in mind, UCP1030 (as Fig 1.) was synthesized to match the major metabolite of UCP1015. However, the fragment pattern in LC-MS/MS of UCP1030 did not match any of the mono-oxidation metabolite of UCP1015. Therefore, propargylic oxidation appeared not to be the major metabolic route for these compounds.

Table 1. Metabolite distribution of lead propargyl-linked antifolates. Percentages based on total AUC.

Compound	Pyridyl N-Oxidation (+16)	Demethylation (-14)	Oxidation on Pyrimidinyl Substructure (+16)	Bis-Oxidation (+32)
UCP1005	60%(M2-1)	16%(M2-2)	14%(M2-3)	10%
UCP1006	45%(M3-1)	28%(M3-2)	26%(M3-3) <5%(M3-4)	10%

UCP1015	71%(M7-1)	6%(M4-2)	5%(M7-3)	15%
UCP1021	74%(M8-1)	20%(M8-2)	6%(M8-3)	2%

Metabolites of compound UCP1021 provided helpful information for assigning biotransformation routes. Three major metabolites identified are *O*-demethylation product (named M8-2, 19.7%) and two mono-oxidation products (M8-1 74.2% and M8-3 6.3%). The collision induced dissociation (CID) spectrum of the parent compound UCP1021 (noted as 8 in Scheme 1.) showed cleavage at either the a-b bond or the b-c bond, generating two primary fragments F1 and F2 (Scheme 1a.). The ion F1 at m/z = 198.1 was assigned as a benzylic cation, whereas ion F2 at m/z = 175.1 was assigned as the propargylic cation. The appearance of either m/z = 198.1 fragment or m/z =175.1 fragment in the CID spectrum of metabolite M8-1 or M8-3 was used to assign the oxidation position to either the F1 or the F2 moieties of the inhibitor. The CID spectrum of the primary metabolite M8-1 showed a fragment at m/z = 175.1, indicating that the oxidation is on the 4-phenylpyridyl subunit. The minor metabolite M8-3 shows the presence of the strong fragment at m/z = 198.1, signifying that the biaryl domain was unchanged and thus oxidation on the pyrimidine moiety. Although the fragmentation pattern was also observed for other testing inhibitors UCP1005, UCP1006 and UCP1015, these diagnostic ions did not appear in the CID spectra of the metabolites.

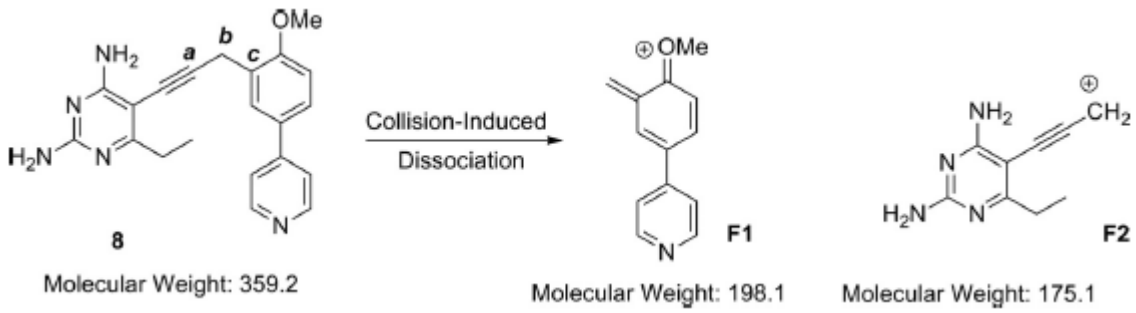

Scheme 1. Diagnostic fragments derived from the ionization of compound 8 (UCP1021).

Both *C*- and *N*-oxidation are possible biotransformation routes for propargyl-linker antifolates, generating pyrimidine-*N*-oxides, which was also observed for TMP [22], pyridine-*N*-oxides, as well as various phenols and alcohols. The CID spectrum of pyridine-*N*-oxides derived from desloratodine [23] showed that two diagnostic fragments were generated by a loss of 17 and 18 mass units from the parent ion. Because similar fragmentation patterns were also observed for CID spectra of M3-1 (Fig 3.) and M3-4 (two metabolites for UCP1006) and clearly not related by isotopic effects (estimated to be 22.8%), the formation of *N*-oxides as a major metabolic pathway seemed probable. Whereas, the CID spectra of M3-3 showed two peaks with loss of 17 and 18 mass units, the integration is close to the expected isotopic effect (23%), therefore the presence of *N*-oxide cannot be unambiguously assigned. In addition, the peaks associated with the *N*-oxides M3-1 and M3-4 eluted with retention time longer than that of the parent compounds, while the demethylation product M3-2 and the unassigned oxidation product M3-3 eluted with shorter retention times than the parent.

The difference in the retention time is likely due to the loss of one of the basic nitrogens, an effect that would be expected with acid mobile phase.

To further verify the identity of these metabolites, synthetic standards of *N*-oxidation products were prepared. It appeared that using controlled oxidation condition of UCP1006 with *m*-chloroperoxybenzoic acid at low temperature generated a mixture of three characteristic *N*-oxides, which were assigned as two regioisomeric pyrimidine-*N*-oxides and the pyridine-*N*-oxide by nuclear magnetic resonance (NMR) (Fig 4.).

a.

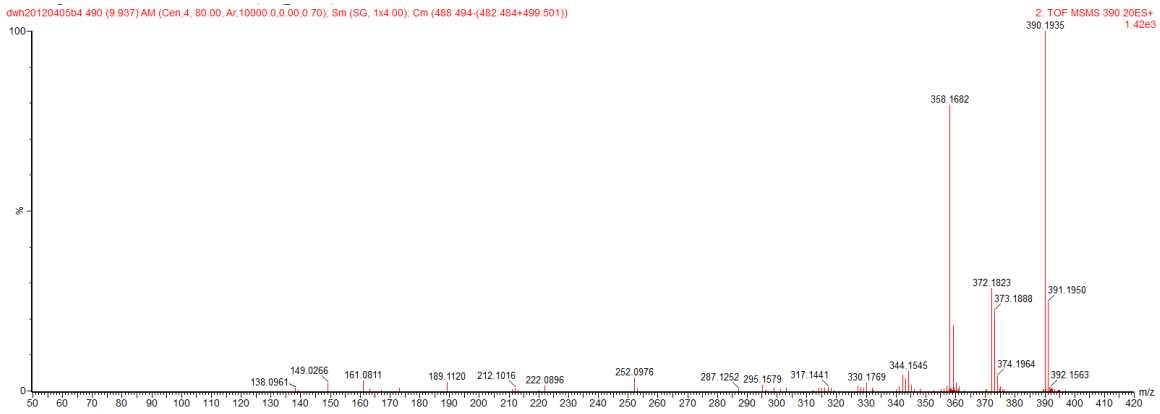

b.

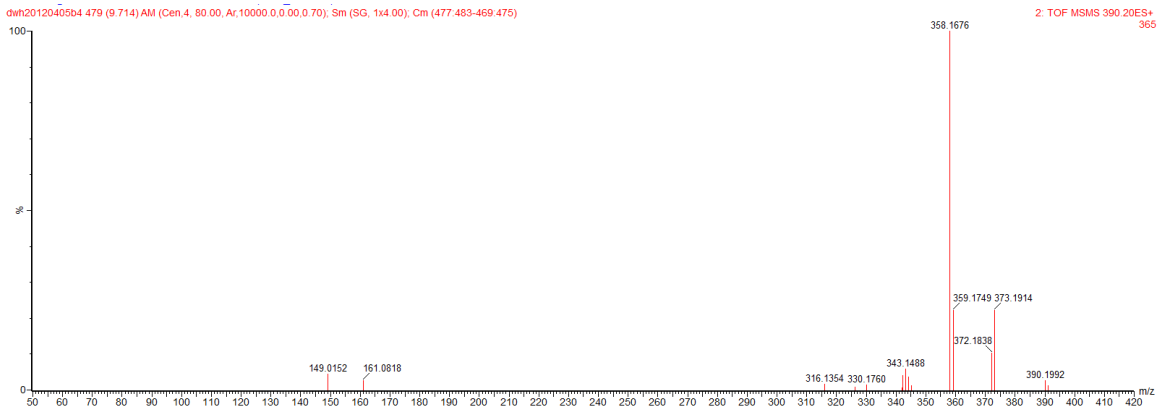

c.

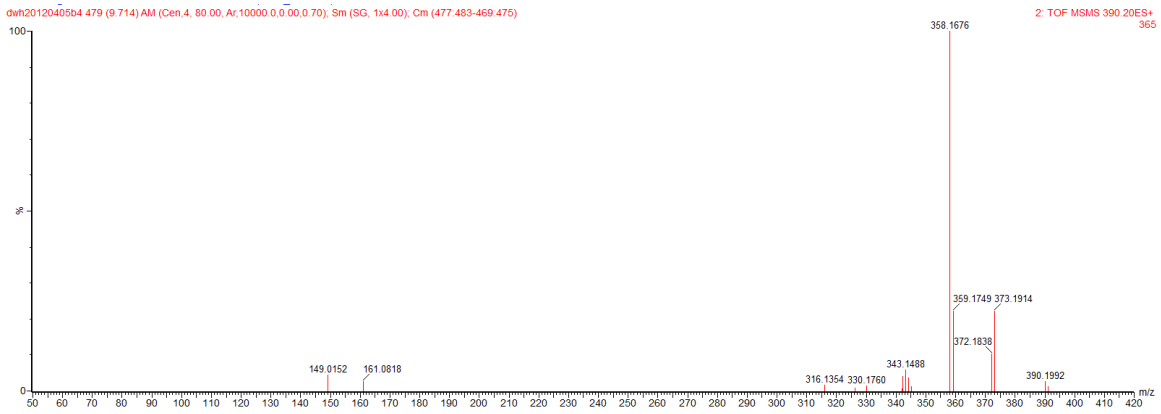

Figure 3. CID spectra of metabolites of UCP1006 a. M3-1, b. M3-3, and c. M3-4.

Careful separation of the pyridine-*N*-oxide from the two pyrimidine-*N*-oxides was performed using HPLC. LC-MS/MS assessment of the synthetic mixture and the metabolic products confirmed that two of the three chemical oxidation products exactly matched two of the metabolites formed during microsomal incubation. Taken together, we were able to unambiguously assign the structure of M3-1 as the pyridine-*N*-oxide using both retention time and CID spectra. Additionally, one of the two isomeric pyrimidine-*N*-oxide also matched with another minor metabolite M3-4. The remaining mono-oxidation product (M3-3) has not been assigned, despite that the fragmentation pattern clearly suggested that the oxidation has occurred on the pyrimidine moiety of the inhibitor and likely to be the product of benzylic oxidation at C6 pyrimidine position.

Using the retention time and CID spectrum, the remaining metabolites from testing compounds UCP1005, UCP1015 and UCP1021 were assigned on the basis of analogy to the metabolite identification process with UCP1006. Despite the difference in metabolic

stability, all three compounds are metabolized primarily through pyridine-*N*-oxidation. Only a trace amount pyrimidine-*N*-oxide was detected for these compounds. Metabolites M2-3, M7-3 and M8-3 appear to be oxidation products on the pyrimidine moiety, such as C6 side chain oxidation or hydroxylamine formation.

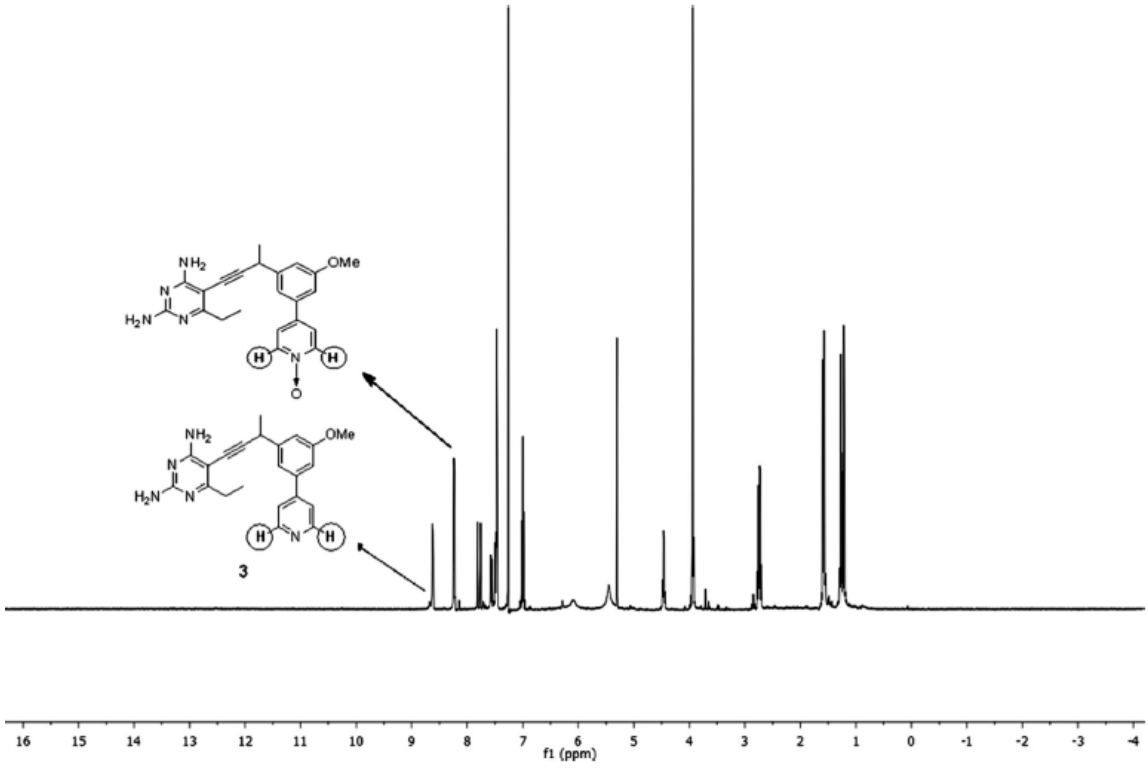

Figure 4. Proton NMR spectra of UCP1006 and the associated pyridine-N-oxide.

4.3. Metabolic stability improvement

Combining the metabolic half-life and metabolite distribution results of compounds UCP1005, UCP1006, UCP1015 and UCP1021, substitutions at the propargylic position and the adjacent aromatic phenyl ring exhibits remote control influence on compound

metabolism on the distal sites. Specifically, metabolic profile of UCP1006 and UCP1015 show that incorporation of branching at the propargyl position increases the half-life by reducing the pyridyl-*N*-oxide rate. Similarly, comparison of UCP1015 and UCP1021 suggests that the placement of a 2' methoxy substituent increases metabolic half-life, although the relative metabolite distribution is largely unaffected. Taken together, substitution near the acetylenic linker, at either the propargylic or the C2' position, slows down the metabolism at the distal pyridine nitrogen likely due to the altering the presentation of the pyridyl nitrogen to the cytochrome P450s active site [14].

It was foreseen that incorporation of both of these design elements may extend the overall metabolic stability of lead compounds while maintaining the pharmacological potency. A hybrid compound, UCP1040, was predicted to fit into the binding pocket of DHFR. A model of UCP1040 bound to *S. aureus* DHFR suggested conservation of the hydrogen bonds between the pyrimidine and active site residues as well as hydrophobic interactions between the C6 ethyl and propargyl group with surrounding residues Val 31, Leu28, Leu54, Ile51, and Phe92. The 2' methoxy group may form positive van der Waals interactions with Met42 or Thr46. Thus, UCP1040 was synthesized and tested [18].

Table 2. Predicted mass, diagnostic ions and assignment of metabolites for compounds 3, 8 and 10 (UCP1006, UCP1021 and UCP1040).

Compound Identifier	Predicted M+H	Diagnostic Daughter Ions	Notes
3	374.1976	175.1; 212.1;	Parent

M3-1[b]	390.1925	373.1888;	Pyridine-*N*-oxide [a]
M3-2	360.1819	175.1; 198.1;	Demethylation
M3-3[b]	390.1925	213.1141; 372.1836;	Alternative oxidation on the pyrimidinyl substructure
M3-4[b]	390.1925	373.1914;	Pyrimidinyl *N*-oxide [a]
8	360.1819	175.1; 198.1;	Parent
M8-1	376.1768	175.1; 214.1;	Pyridine-*N*-oxide [a]
M8-2	346.1663	175.1; 184.1;	Demethylation
M8-3	376.1768	198.1;	Alternative oxidation on the pyrimidinyl substructure
10[b]	374.1976	175.1008; 197.0862;	Parent
M10-1[b]	390.1925	175.0974; 228.1016; 373.1907	Pyridine-*N*-oxide [a]
M10-2[b]	360.1819	175.1021; 184.0792;	Demethylation
M10-3[b]	390.1925	174.0863; 228.1010; 372.1768;	Alternative oxidation on the pyrimidinyl substructure
M10-4[b]	390.1925	175.0955; 228.1010; 373.1862;	Pyridine-*N*-oxide [a]
M10-5[b]	390.1925	212.1076; 372.1859	Alternative oxidation on the pyrimidinyl substructure

[a] Structure confirmed by synthesized standards.

[b] Analyte masses were accurate to 10ppm.

A metabolic stability study of UCP1040 with similar testing conditions showed significantly improvement with doubled half-life ($t_{1/2}$ = 65 min) relative to the initial lead series. LC-MS/MS analysis of the microsomal mixture revealed five major metabolites (Fig. 5; Table 2). M10-2 (20.3%) was again easily assigned as the *O*-demethylation product. The other four products (M10-1, M10-3, M10-4 and M10-5) show 16 mass unit increases compared the parent compounds, indicating mono-oxidation. With similar fragmentation pattern, the 2'-methoxy donor promoted dissociation together with the propargylic linker, generating diagnostic daughter ions to assign pyrimidinyl and 4-phenylpyridinyl oxidation. Synthetic pyridinyl and pyrimidinyl *N*-oxidation products were also used for metabolite verification. Semi-quantitative analysis of metabolite distribution revealed that the pyridine-*N*-oxide remained the predominant metabolite (M10-1), accounting for 54.3% of the total metabolite. Another chemically matched product pyrimidine-N-oxide (M10-4) was present at 7.2%. The CID spectrum of the remaining two identified mono-oxidation products (M10-3 and M10-5) suggested oxidation on the pyrimidinyl moiety and were tentatively assigned to the C6 position of the pyrimidine.

Insight from the crystal structure of UCP1006 bound to wild type *S. aureus* DHFR [24]clearly shows that the pyridyl nitrogen is solvent exposed and does not directly interact with the enzyme, suggesting that its major metabolite pyridine-*N*-oxide may retain the enzymatic inhibition activity. Chemically synthesized pyridine-*N*-oxide of UCP1040 (M10-1) was purified by HPLC and the weight was determined using a UCP1040 standard curve generated by LC-MS (assuming the same ionization efficiency).

The residual activity of M10-1 was evaluated with a *Candida glabrata* DHFR inhibition assay [15]. Excitingly, M10-1 shows promising *C. glabrata* DHFR inhibition (IC_{50} = 45 nM), indicating the formation of an active metabolite.

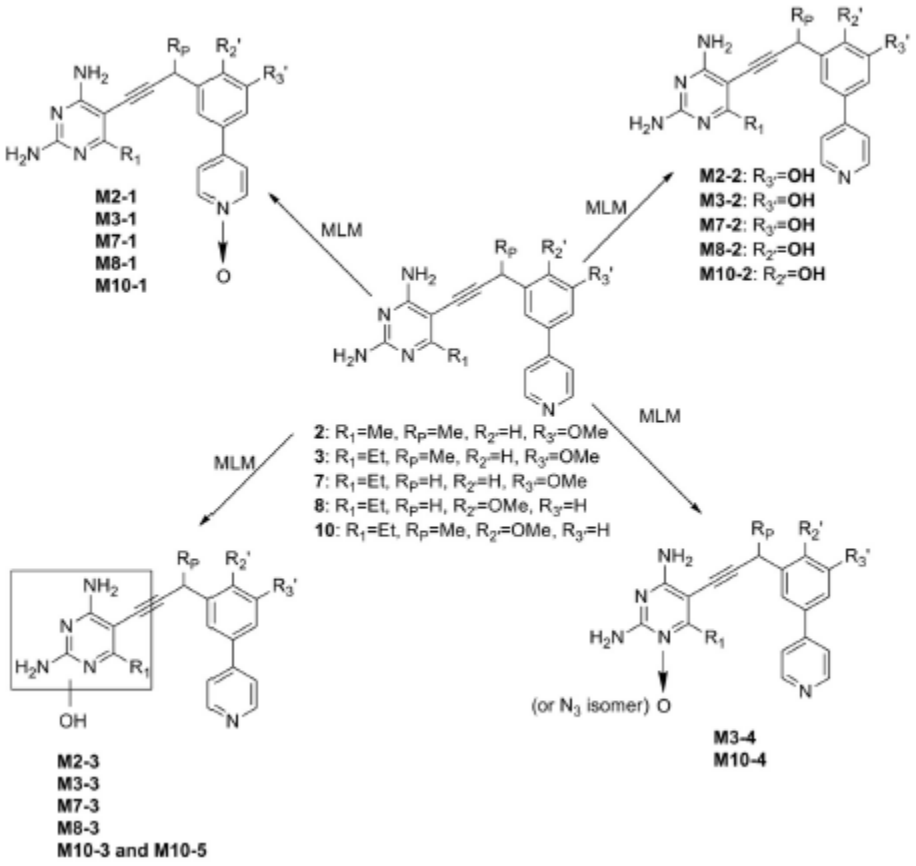

Figure 5. Major metabolites derived from compounds 2, 3, 7, 8, and 10 (UCP1005, UCP1006, UCP1015, UCP1021 and UCP1040).

4.4. Conclusions

The metabolite identification study of lead pyridine serial propargyl-linked antifolates revealed that the major metabolic routes are pyridine-*N*-oxidation and demethylation

on the phenyl methoxy group. SPR analysis suggested that the propargylic methyl and 2' methoxy at adjacent phenyl substitutions increased metabolic stability. A hybrid compound UCP1040 was therefore synthesized and exhibited marked half-life improvement. The increase in metabolic stability likely resulted from the lower *N*-oxidation rate at the distal pyridine position. The major UCP1040 metabolite also shows potent antifungal activity. To further understand potential ADME weaknesses and improve the drug likeliness of propargyl-linked antifolates, additional strategies to optimize water solubility and metabolic stability will be investigated.

4.5. Acknowledgements

I gratefully acknowledge Dr. Kishore Viswanathan for his work on compound synthesis, preparation and NMR characterization of pyridine-*N*-oxide standards. Special thanks to Dr. Janet Paulsen for her CgDHFR inhibition testing for the active metabolite of UCP1040. I would also like to thank Dr. Dennis Hill for his initial training on LC-MS/MS analysis and data analysis.

4.6. References

1. Orloff, J., et al., *The future of drug development: advancing clinical trial design.* Nat Rev Drug Discov, 2009. **8**(12): p. 949-57.
2. Paul, S.M., et al., *How to improve R&D productivity: the pharmaceutical industry's grand challenge.* Nat Rev Drug Discov, 2010. **9**(3): p. 203-14.
3. Kennedy, T., *Managing the drug discovery/development interface.* Drug Discov Today, 1997. **2**(10): p. 436-444.
4. Kola, I. and J. Landis, *Can the pharmaceutical industry reduce attrition rates?* Nat Rev Drug Discov, 2004. **3**(8): p. 711-5.
5. Ballard, P., et al., *The right compound in the right assay at the right time: an integrated discovery DMPK strategy.* Drug Metab Rev, 2012. **44**(3): p. 224-52.

6. Stepan, A.F., et al., *Evaluating the differences in cycloalkyl ether metabolism using the design parameter "lipophilic metabolism efficiency" (LipMetE) and a matched molecular pairs analysis.* J Med Chem, 2013. **56**(17): p. 6985-90.
7. Wienkers, L.C. and T.G. Heath, *Predicting in vivo drug interactions from in vitro drug discovery data.* Nat Rev Drug Discov, 2005. **4**(10): p. 825-33.
8. Kerns, E.H. and D. Li, *Drug-like Properties: Concepts, Structure Design and Methods.* Academic Press;, 2008.
9. Ansede, J.H. and D.R. Thakker, *High-throughput screening for stability and inhibitory activity of compounds toward cytochrome P450-mediated metabolism.* J Pharm Sci, 2004. **93**(2): p. 239-55.
10. Di, L., et al., *Experimental design on single-time-point high-throughput microsomal stability assay.* J Pharm Sci, 2004. **93**(6): p. 1537-44.
11. Rodrigues, A.D. and J.H. Lin, *Screening of drug candidates for their drug--drug interaction potential.* Curr Opin Chem Biol, 2001. **5**(4): p. 396-401.
12. Kerns, E.H. and L. Di, *Pharmaceutical profiling in drug discovery.* Drug Discov Today, 2003. **8**(7): p. 316-23.
13. Di, L. and E.H. Kerns, *Profiling drug-like properties in discovery research.* Curr Opin Chem Biol, 2003. **7**(3): p. 402-8.
14. Viswanathan, K., et al., *Toward new therapeutics for skin and soft tissue infections: propargyl-linked antifolates are potent inhibitors of MRSA and Streptococcus pyogenes.* PLoS One, 2012. **7**(2): p. e29434.
15. Paulsen, J.L., et al., *Structural analysis of the active sites of dihydrofolate reductase from two species of Candida uncovers ligand-induced conformational changes shared among species.* Bioorg Med Chem Lett, 2013. **23**(5): p. 1279-84.
16. Liu, J., et al., *Towards new antifolates targeting eukaryotic opportunistic infections.* Eukaryot Cell, 2009. **8**(4): p. 483-6.
17. Kansy, M., F. Senner, and K. Gubernator, *Physicochemical high throughput screening: parallel artificial membrane permeation assay in the description of passive absorption processes.* J Med Chem, 1998. **41**(7): p. 1007-10.
18. Zhou, W., et al., *Acetylenic linkers in lead compounds: a study of the stability of the propargyl-linked antifolates.* Drug Metab Dispos, 2012. **40**(10): p. 2002-8.
19. Di, L. and E.H. Kerns, *Solution stability--plasma, gastrointestinal, bioassay.* Curr Drug Metab, 2008. **9**(9): p. 860-8.
20. Di, L., et al., *High throughput microsomal stability assay for insoluble compounds.* Int J Pharm, 2006. **317**(1): p. 54-60.
21. Hill, D.W., et al., *Mass spectral metabonomics beyond elemental formula: chemical database querying by matching experimental with computational fragmentation spectra.* Anal Chem, 2008. **80**(14): p. 5574-82.
22. Sigel, C.W. and D.A. Brent, *Identification of trimethoprim 3-oxide as a new urinary metabolite of trimethoprim in man.* J Pharm Sci, 1973. **62**(4): p. 694-5.
23. Ramanathan, R., ed. *Mass Spectrometry in Drug Metabolism and Pharmacokinetics*. 2011, John Wiley & Sons, Hoboken.
24. Frey, K.M., et al., *Prospective screening of novel antibacterial inhibitors of dihydrofolate reductase for mutational resistance.* Antimicrob Agents Chemother, 2012. **56**(7): p. 3556-62.

Chapter 5

Solubility and metabolic stability optimization

5.1. Introduction

Lead propargyl-linked antifolates have been proven to be potent inhibitors against *Staphylococcus aureus* and *Candida spp* [1-4]. However, potent ligands are not necessarily efficacious drug molecules. To further precede these drug discovery efforts, lead compounds with optimal drug like properties, which will translate to good drug exposure *in vivo* need to be developed.

Initial ADME assessment of lead propargyl-linked antifolates revealed poor water solubility and metabolic stability. Preliminary efforts to modify biphenyl series compounds by introducing heterocyclic functional groups reduced hydrophobicity, balanced overall molecule polarity and increased water solubility [5]. In addition, early metabolic stability evaluation and metabolite identification studies also provided helpful strategies to prolong *in vitro* microsomal half-live. To effectively deliver high doses of drug and achieve good drug exposure *in vivo*, improved lead compounds with less metabolic “soft spots” and better water solubility are warranted.

In this chapter, a strategy to incorporate crystallographic insight and improve water solubility by substituting more hydrophobic groups with polar functionality while maintaining antimicrobial potency will be implemented. Detailed SPR analysis will also be performed to increase metabolic stability by blocking the key metabolic oxidation

sites. New lead compounds with better ADME properties will be designed, synthesized and evaluated.

5.2. Optimizing the water solubility of propargyl-linked antifolates

The evolution of propargyl-linked antifolates has led to a significant increase in hydrophobicity. As described in chapter 3, preliminary assessment indicates that biphenyl series lead compounds precipitate from DMSO and biological buffers over time. Initial attempt to improve water solubility of biphenyl lead compounds by introducing heterocyclic functionality effectively reduced $cLogD_{7.4}$ values and increased experimental solution solubility with the presence of HPMC. To further increase the polarity of the lead compounds and select better drug-like antifolates for animal based efficacy testing, multiple modification approaches were attempted.

5.2.1 Substitution of the adjacent aromatic ring

The search for effective dual inhibitors against *C. glabrata* and *C. albicans* has lead to the discovery of para- linked compounds (distal aromatic ring on the para position of the adjacent aromatic ring, e.g. UCP111H and UCP111E, Fig. 1.), that exhibited excellent potency in both enzymatic and fungal growth inhibition [4, 6]. Similar to their meta-linked analogues (UCP111D, UCP111D4M etc), these para-linked biphenyl lead compounds are also associated with poor water solubility. To improve water solubility, substituting the distal phenyl ring (UCP1043) with more polar pyridine functionality (UCP1044) significantly decreased the calculated LogD value at pH7.4 from 4.66 to 3.44. UCP1044 is potent against DHFR from *C. grabrata* and *C. albicans*, with IC_{50} values at

19nM and 33nM, (Fig 1.) respectively. However, despite UCP1044 being a potent *C. grabrata* inhibitor (MIC=0.78 µg/mL), it doesn't effectively inhibit *C. albicans* growth (MIC=25 µg/mL) [6]. The loss of antifungal activity is likely due to the poor membrane permeability through *C. albicans* outer membrane [7].

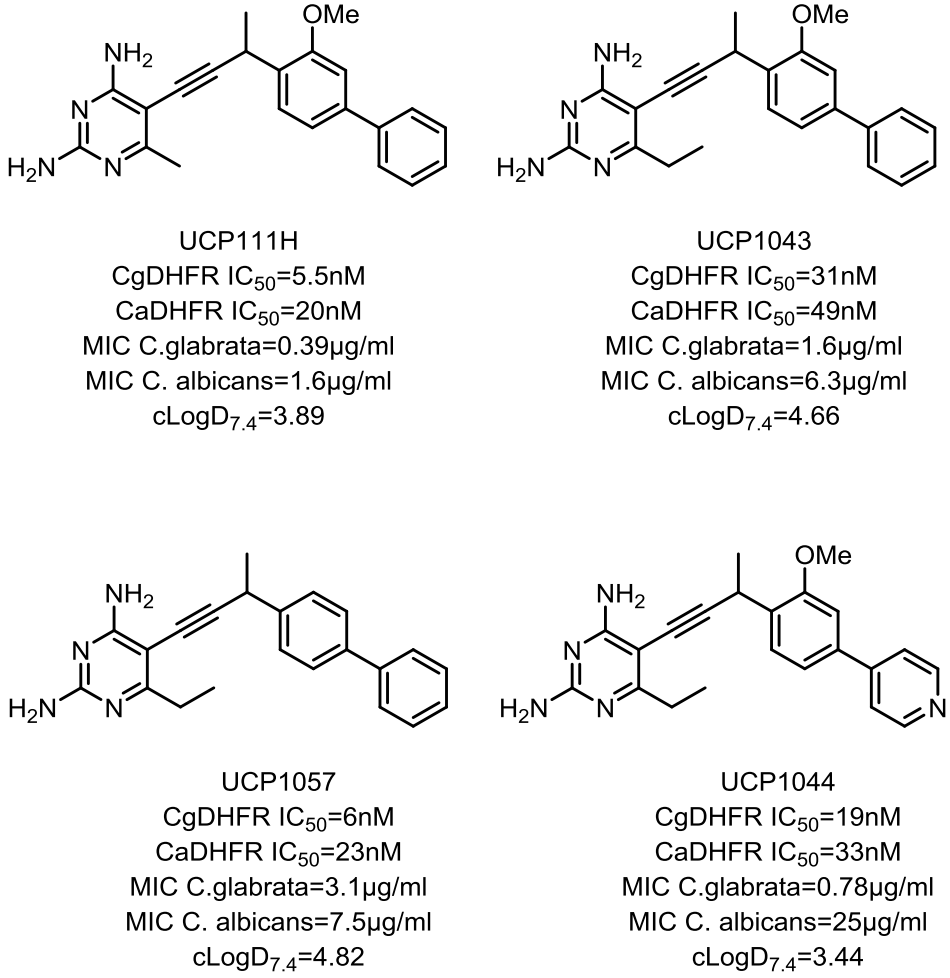

Figure 1. Enzymatic inhibition and antifungal activity of para-linked inhibitors.

Comparisons of the activity of UCP1043 and UCP1057 (Fig 1.) indicate that the methoxy substitution is well tolerated at the 2' position of the adjacent phenyl ring but not required for potency. Therefore, adding a polar basic nitrogen to the adjacent ring may

increase the water solubility and balance the overall polarity of the molecule, without losing the dual antifungal potency. In contrast to distal pyridines, incorporating pyridine at the adjacent position (UCP1051) did not significant increase water solubility, comparing to UCP111H (Fig 2), 25 µg/mL versus 20 µg/mL. However, UCP1055 featuring a much more polar pyrimidine substitution at the adjacent position exhibited a sharp improvement to 60 µg/mL. More excitingly, UCP1055 also show potent antifungal activity with MIC value of 0.78 µg/mL and 0.19 µg/mL against *C. glabrata* and *C. albicans*, respectively.

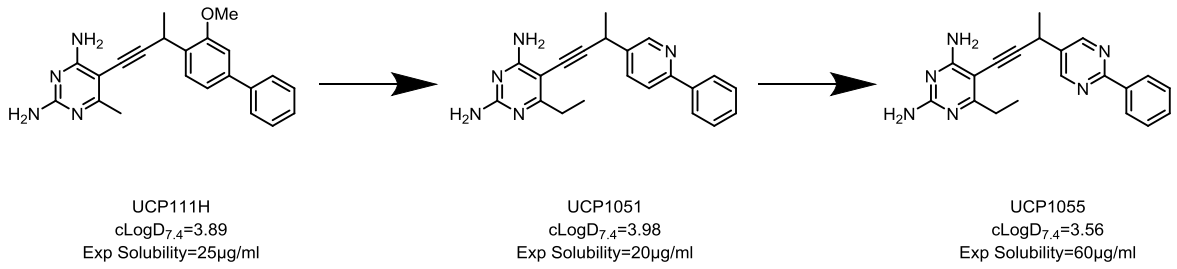

Figure 2. Structure and solubility of para-linked lead compounds.

5.2.2 Double pyridine analogues

To prove *in vivo* efficiency against MRSA or fungal infection, good drug exposure is desired. To ensure high dosage delivery, further improvement in water solubility is needed. Previous approaches to modify hydrophobic phenyl rings to polar heterocyclic functional group significant decreased cLogD values at pH7.4 and increased water solubility. It is reasonable to assume that changing both phenyl rings to nitrogen-containing pyridine will further increase solubility. *In silico* calculation also supported that with double pyridines, cLogD values at pH7.4 of analogues UCP1093 and UCP1094

(Fig 3.) decreased to 2.77 and 2.38, respectively. Crystallographic insight also suggested that both of the compounds should fit in the SaDHFR binding site with similar or improved affinity (data not shown). However, surprisingly, UCP1094 was not soluble even at 1 mg/mL in DMSO, which inhibited efficient solubility testing. UCP1093 was soluble at 20 mg/mL in DMSO stock, but lost its antibacterial activity with MIC values of 2.5 μg/mL (over 30 folds less potent than UCP1006) against wild type *S. aureus*.

Noticeably, UCP1094 DMSO stock at 20 mg/mL was turbid at room temperature; however, it solubilized when heated with a flame for a few seconds. This temperature driven phenomenon likely indicated that the low solubility of UCP1094 was because of crystallization within the aqueous solution instead of low solubility. Taken together, future solubility optimization should focus on preventing the stacking or crystallization effect instead of reducing hydrophobicity alone.

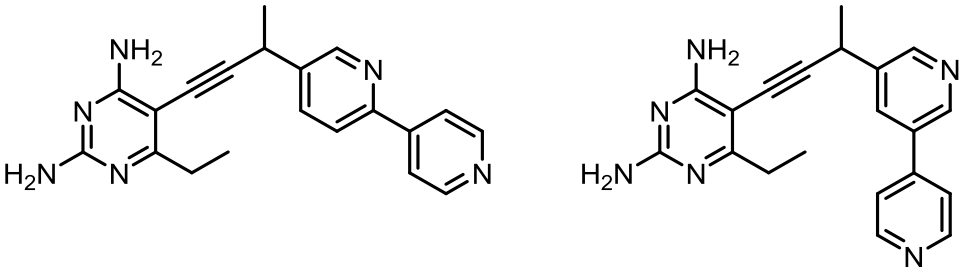

UCP1093
$cLogD_{7.4}$=2.77

UCP1094
$cLogD_{7.4}$=2.38

Figure 3. Structure and $cLogD_{7.4}$ value of double pyridine analogues

5.3. Optimizing the metabolic stability of propargyl-linked antifolates

Initial assessment (chapter 4) suggested that the metabolic stability of lead pyridine series antifolates are sensitive to the substitutions around the propargylic position and the 2’ or 3’ position of the adjacent phenyl ring. The hybrid compound UCP1040 with propargyl methyl and 2’ methoxy shows improved metabolic half-life *in vitro* with mouse liver microsomes (MLM). Metabolite identification study indicated that despite the metabolic half-life difference between UCP1006 (35 mins) and UCP1040 (65 mins), two compounds share similar metabolic routes. To further improve *in vitro* metabolic stability and potentially improve *in vivo* drug exposure, several strategies were implemented in this section.

5.3.1 Improving metabolic stability with dioxolane

Metabolic stability and metabolite identification study of UCP1006 and UCP1040 indicated that introduction of 2’ methoxy group significantly increased the metabolic half-life by reducing the N-oxidation rate on the distal pyridine. The remotely controlled effect of the positioning of the methoxy is likely due to a change in the conformation of the minimal energy form (data not shown). A 3’ 4’ dioxolane on the adjacent phenyl ring is hypothesized to have a similar effect with low N-oxidation rate on the distal pyridine. At the same time, the dioxolane should further prolong the metabolic half-life by blocking the demethylation, which is the second predominant metabolic route for both UCP1006 and UCP1040. Furthermore, structural evaluation using crystal structure of wild type SaDHFR bound to UCP1006 indicated that the binding pocket of SaDHFR is large enough to accommodate the 5 member ring (data not shown). With the

hypothesis that the dioxolane analogue will retain antibacterial activity while improving metabolic stability, UCP1038 was then synthesized and evaluated.

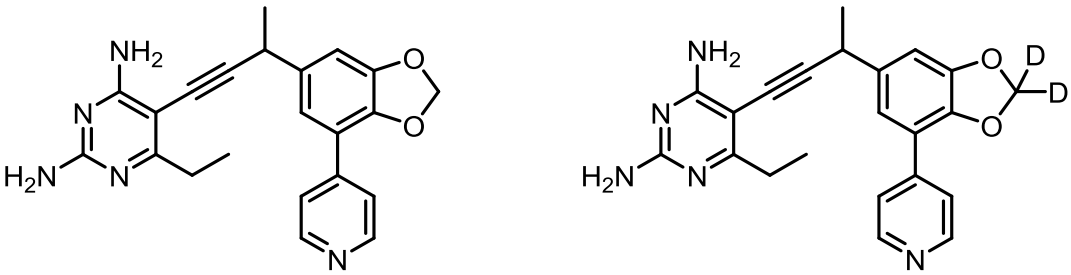

UCP1038
MIC *S.aureus*=0.78μg/ml
MLM $T_{1/2}$=79mins
HLM $T_{1/2}$=270mins

UCP1070
MIC *S.aureus*=0.78μg/ml
MLM $T_{1/2}$=91mins

Figure 4. Structure, metabolic stability, and antibacterial activity of dioxolane analogues

UCP1038 exhibited excellent antibacterial potency with an IC_{50} value of 17 nM against SaDHFR and a MIC value of 0.078 μg/mL. In addition, the metabolic stability of UCP1038 significantly improved with a half-life of 79mins in MLM and over 270mins in human liver microsomes (HLM). To understand the mechanism of the enhancement of metabolic stability and the metabolic routes of UCP1038, a metabolite identification study was performed with MLM by LC-MS/MS in a similar testing condition as described before. Surprisingly, despite the observation of parent compound loss during the incubation, no obvious metabolite was detected. It was speculated that UCP1038 might have covalently bound to cytochrome P450s (CYP) during the incubation with MLM and therefore acted as a suicide inhibitor. Literature suggested that 1, 3-Benzodioxoles analogues commonly act as quasi-irreversible CYP450 inhibitors, the mechanism of which is described in Figure 5 [8-9]. As shown, bioactivation of 1, 3-benzodioxole

derivatives are initiated via hydrogen atom abstraction from the methylene carbon or by elimination of water from a hydroxymethylene intermediate, generating a reactive carbene intermediate, which subsequently forms a metabolite-intermediate (MI) complex with ferrous iron from the CYP450s. The hydroxymethylene intermediate can also undergo demethylenation, yielding a catechol intermediate, which may covalently bind to the CYP apoprotein. To further validate this hypothesis, a glutathione (GSH) trapping assay with MLM was pursued as reported [10]. However, no GSH-adduct was detected by tandem MS. In addition, the metabolic stability was unchanged with the presence of GSH.

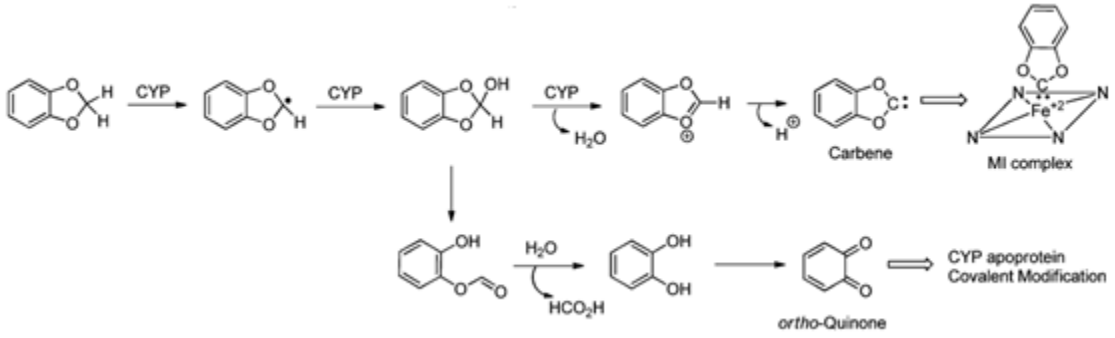

Figure 5. Mechanism-based CYP inhibition and formation of MI complex by 1, 3-Benzodioxoles[8]

A well-accepted strategy to reduce potential reactive intermediate formation is to replace the dioxolane hydrogens with deuterium [11-13]. Thus, UCP1070, a deuterium substituted analogue of UCP1038 was synthesized. UCP1070 retained potent antibacterial activity with a MIC value of 0.078 µg/mL and superb metabolic stability with $T_{1/2}$ of 91 min with MLM and 102 min with HLM. A metabolite identification study

of UCP1070 with MLM shows only one major phase I metabolite with m/z at 376 (-14 mass unit comparing to protonated parent compound). The CID spectrum of the metabolite indicated a loss of 14 mass units on the benzodioxolane-pyridinyl moiety of the molecule. The metabolite structure (P1 metabolite) was tentatively assigned as loss of the methylene group (shown in Fig 6). Metabolic incubation with mouse liver S9 fractions in the presence of both phase I and II cofactors for UCP1070 also suggested that the phase I metabolite can also undergo phase II glucuronidation. The glucuronidation product was tentatively assigned as *O*-glucuronide conjugation on the 3' or 4' position of the phenyl hydroxyl (shown in Fig 6).

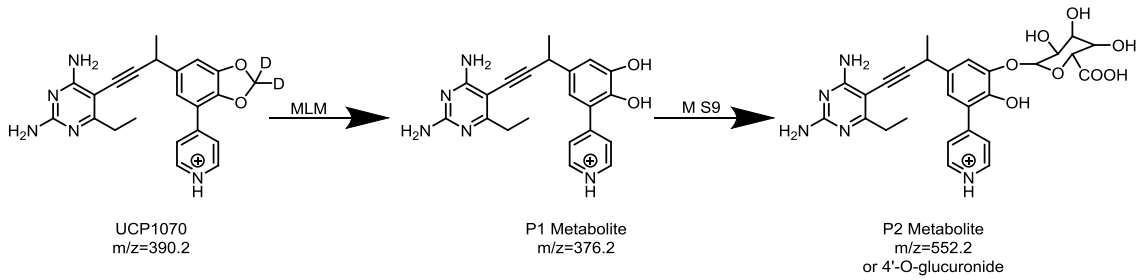

Figure 6. Structure and m/z values of UCP1070 and proposed metabolites

UCP1070 exhibited potent antibacterial activity and exceptional metabolic stability *in vitro*. Different from UCP1038, the deuterium substitution likely reduced the formation of the reactive metabolite, which may translate into decreased covalent binding burden *in vivo*. Overall, UCP1070 is a promising lead compound that should be further characterized for other *in vitro* ADME properties and evaluated for *in vivo* pharmacokinetics and efficacy.

5.3.2 Improving metabolic stability with single enantiomers

Initial testing for lead propargyl-linked antifolates indicated that the propargylic methyl substitution is important to retain metabolic stability. The crystal structure of UCP1006 bound to wild type SaDHFR also suggested that only one of the racemic molecules is present. To explore the stereo chemistry of the propargyl position and its relationship to antibacterial activity, three pairs of single enantiomers UCP1006 (UCP1061 and UCP1062), UCP1040 (UCP1063 and UCP1064), and UCP1038 (UCP1098 and UCP1099) were synthesized and evaluated (Fig 7.).

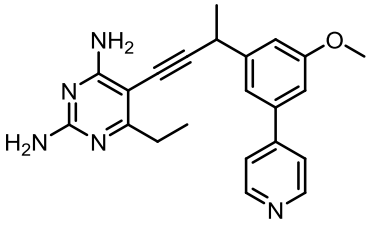

UCP1006
MIC *S. aureus*=0.078µg/ml
MLM $T_{1/2}$=35min
HLM $T_{1/2}$=95min

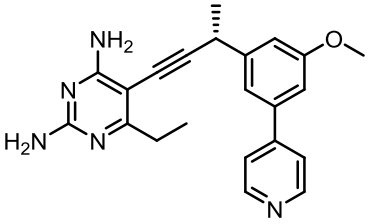

UCP1061
MIC *S. aureus*=0.3125µg/ml
MLM $T_{1/2}$=37min
HLM $T_{1/2}$=100min

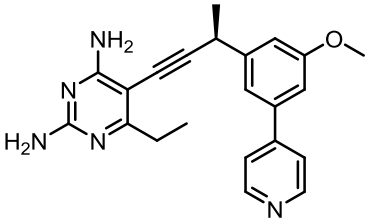

UCP1062
MIC *S. aureus*=0.0391µg/ml
MLM $T_{1/2}$=37min
HLM $T_{1/2}$=75min

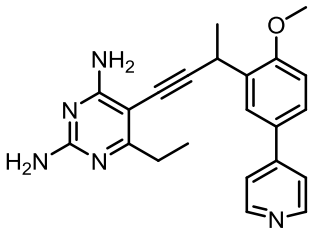

UCP1040
MIC *S. aureus*=0.625µg/ml
MLM $T_{1/2}$=65min
HLM $T_{1/2}$=87min

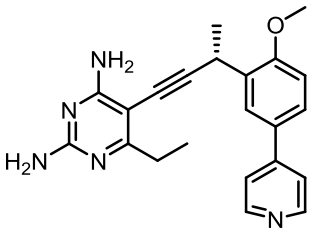

UCP1063
MIC *S. aureus*=0.0195µg/ml
MLM $T_{1/2}$=97min
HLM $T_{1/2}$=146min

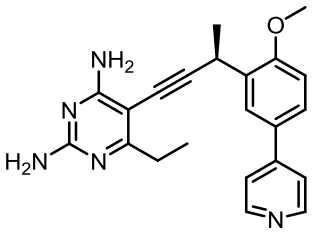

UCP1064
MIC *S. aureus*=0.3125µg/ml
MLM $T_{1/2}$=61min
HLM $T_{1/2}$=135min

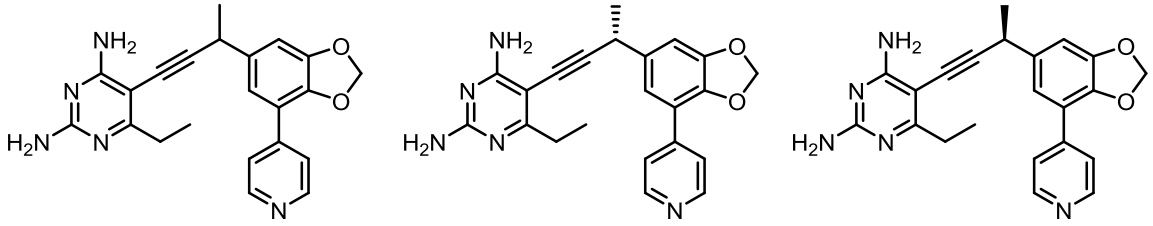

UCP1038
MIC *S. aureus*=0.0781μg/ml
MLM $T_{1/2}$=79min
HLM $T_{1/2}$=270min

UCP1098
MIC *S. aureus*=0.3125μg/ml
MLM $T_{1/2}$=106min
HLM $T_{1/2}$=N/A

UCP1099
MIC *S. aureus*=0.0195μg/ml
MLM $T_{1/2}$=139min
HLM $T_{1/2}$=N/A

Figure 7. Structure, antibacterial activity and metabolic half-life of UCP1006, UCP1040, UCP1038 and its single enantiomers.

Strikingly, UCP1063, the *R*-enantiomer of UCP1040 was 16 fold more potent than its racemic mixture with a MIC value of 0.0195 μg/mL against *S. aureus* (compared to MIC value of 0.625 μg/mL for racemic mixture). UCP1064, the *S*-enantiomer of UCP1040 also exhibited improved antibacterial activity with MIC value of 0.3125 μg/mL. Comparing to the racemic mixture, UCP1063 also showed improvement in metabolic stability with a half-life of 97 minutes and 146 minutes with MLM and HLM, respectively. UCP1064 exhibited a similar metabolic half-life with MLM (61 min) compared to UCP1040. A metabolite identification study with UCP1063 and UCP1064 with MLM indicated that UCP1064 generates one more metabolite with retention time at 8.74 min compared to UCP1063, which may explain the difference in metabolic half-life. Combining the CID spectrum of UCP1064 and UCP1040 metabolites, it appeared that the unique metabolite for UCP1064 was the hydroxylation product on the pyrimidyl moiety of the molecule (shown as Fig 8).

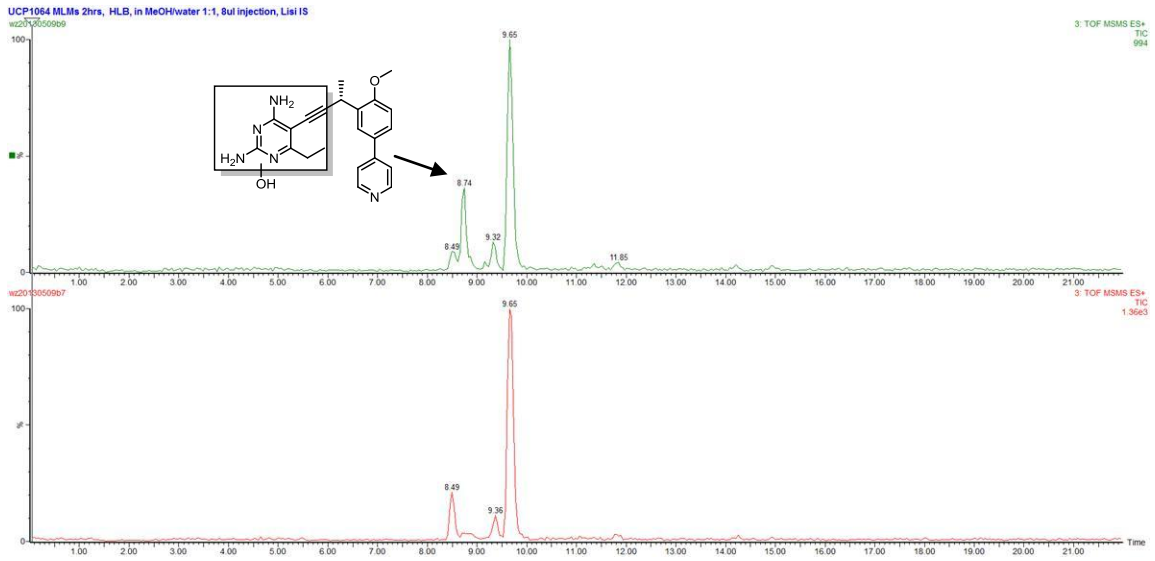

Figure 8. Upper panel chromatogram of UCP1064 after 2hr MLM incubation at m/z=390; lower panel chromatogram of UCP1063 after 2hr MLM incubation at m/z=390;

Similar to UCP1040 and its single enantiomers, the other two pairs of compounds exhibited differences in antibacterial activities. The *S*-enantiomer of UCP1006 (UCP1063) and the *R*-enantiomer of UCP1038 (UCP1099) both were 16 fold more potent than the other enantiomers. It was hypothesized that the two enantiomers may antoginize each other, resulting in a lower potency of the racemic compounds. However, detailed mechanism of this is still under investigation.

5.3.3 Improving metabolic stability with a modified pyridine ring

Previous metabolite identification studies revealed that the predominant route of metabolism for lead propargyl-linked antifolates is *N*-oxidation on the distal pyridine ring. To block the reaction, several analogues with modified distal functionality were synthesized and tested. UCP1066 is characterized by a distal pyrazine group with two basic nitrogen atoms. It was proposed that the second nitrogen would balance the

electron density of the aromatic ring and result in decreased binding to CYP450 metabolism and prolonged half-life. UCP1071 featured a 2'-pyridine, instead of a 4'-pyridine in UCP1040. The rotation of the pyridine ring aimed to reduce the accessibility of basic nitrogen to CYPs and therefore reduce the *N*-oxidation. UCP1076 and UCP1077 highlighted protected 4'-pyridine distal substitution. The addition of hydrophobic functionality next to the pyridine nitrogen should limit the binding to CYP, shield the pyridine nitrogen and block the pyridine N-oxide formation.

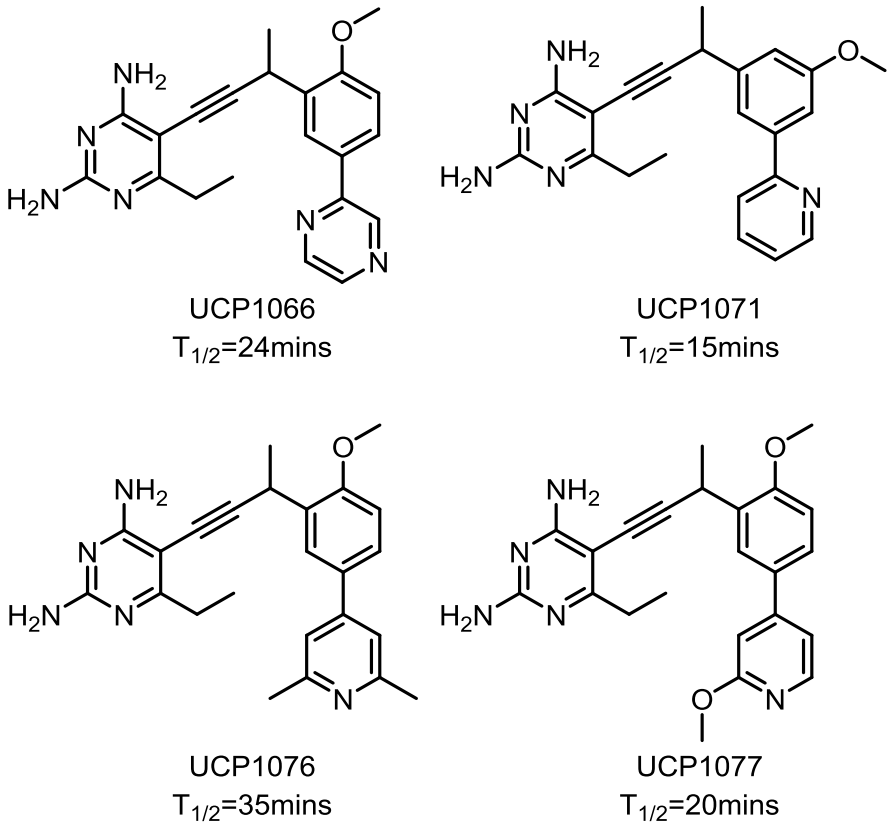

Figure 9. Structure and *in vitro* MLM metabolic half-life of UCP1066, UCP1071, UCP1076 and UCP1077.

Surprisingly, none of the four newer compounds show improved metabolic stability compared to UCP1040. The metabolite identification study of UCP1076 with MLM indicated that the dimethyl pyridine completely eliminated N-oxidation formation observed with in exposed pyridine (UCP1006 and UCP1040). The only major phase I metabolite detected after MLM incubation was a demethylation product; only a trace amount of mono-hydroxylation product was detected. When incubated in the presence of both phase I and phase II cofactors uridine diphosphate glucuronic acid (UDT-GA), acetyl-CoA and 3'-phosphoadenosine-5'-phosphosulfate (PAPS), the phase I demethylation metabolite likely underwent phase II conjugations, generating two additional metabolites with m/z=564.2 and 404.2. The metabolites structures were tentatively assigned as shown in figure 10. However, despite the elimination of the predominant metabolic route, the overall metabolic half-life with MLM did not improve ($t_{1/2}$=35 mins) compared to UCP1040 ($t_{1/2}$=65 mins). Therefore, more quantitative evaluation for metabolite formation is needed in the future.

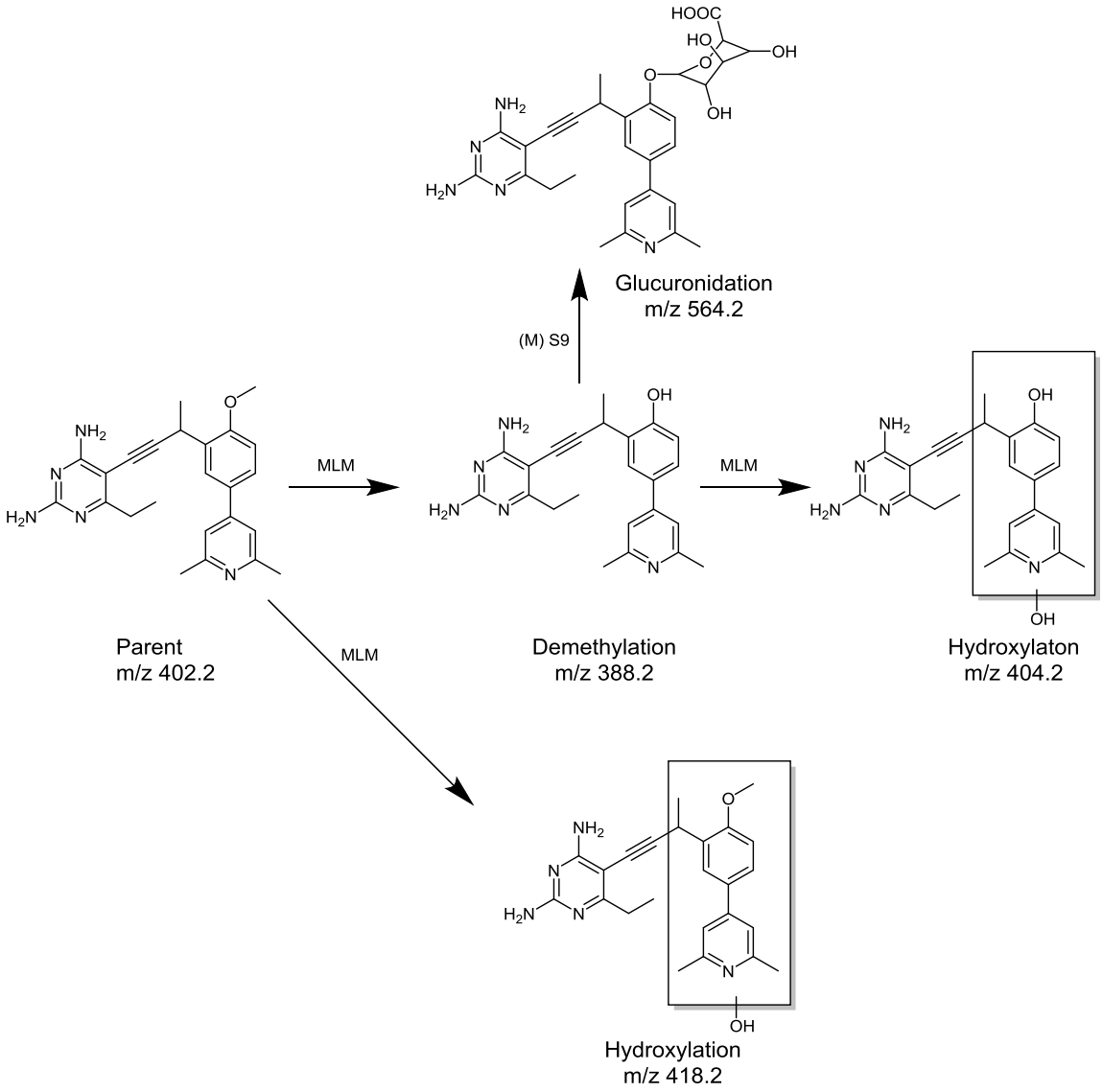

Figure 10. Structure and m/z values of UCP1076 and proposed metabolites

5.4. Conclusions

To improve the water solubility of the lead propargyl-linked compounds while maintaining potent antimicrobial activity, several approaches to introduce more polar functional groups were explored. However, the decrease in lipophilicity did not effectively translate into increased water solubility, indicating that the low water

solubility of several lead compounds likely results from crystallization in solution instead of high hydrophobicity. Metabolic stability optimization efforts were also implemented. Analogues with deuterated benzodioxoles at the adjacent position and single enantiomers at the propargylic position exhibited potent antibacterial activity and promising metabolic stability. Additional substitutions at the distal ring position were also investigated. Although less stable with MLM, dimethypyridine analogue UCP1076 completely blocked the pyridine-*N*-oxidation formation in microsomes. To better support the development of propargyl-linked antifolates and rank order metabolically stable lead compounds, quantitative analysis of multiple time-point microsomal stability testing at low testing concentration will be performed. CYP inhibition of lead compounds will be also evaluated to assess the potential to induce drug-drug interactions. Candidate compounds with exceptional in vitro antimicrobial activity and excellent ADME properties will be selected for *in vivo* PK and efficacy evaluation.

5.5. Acknowledgements

Special thanks to Narendran Dayanan, Dr. Kishore Viswanathan and Dr. Santosh Keshipeddy for compounds synthesis. I would like to thank Drs. Janet Paulsen and Mike Lombardo for antifungal activity testing and Stephanie Reeve for the antibacterial potency testing against *S. aureus*.

5.4. References

1. Frey, K.M., et al., *Towards the understanding of resistance mechanisms in clinically isolated trimethoprim-resistant, methicillin-resistant Staphylococcus aureus dihydrofolate reductase.* J Struct Biol, 2010. **170**(1): p. 93-7.

2. Liu, J., et al., *Towards new antifolates targeting eukaryotic opportunistic infections.* Eukaryot Cell, 2009. **8**(4): p. 483-6.
3. Viswanathan, K., et al., *Toward new therapeutics for skin and soft tissue infections: propargyl-linked antifolates are potent inhibitors of MRSA and Streptococcus pyogenes.* PLoS One, 2012. **7**(2): p. e29434.
4. Paulsen, J.L., et al., *Structural analysis of the active sites of dihydrofolate reductase from two species of Candida uncovers ligand-induced conformational changes shared among species.* Bioorg Med Chem Lett, 2013. **23**(5): p. 1279-84.
5. Zhou, W., et al., *Antifolates as effective antimicrobial agents: new generations of trimethoprim analogs.* MedChemComm, 2013.
6. N, G.D., et al., *Propargyl-Linked Antifolates are Dual Inhibitors of Candida albicans and Candida glabrata.* J Med Chem, 2014. **57**(6): p. 2643-56.
7. Ziegelbauer, K., et al., *High throughput assay to detect compounds that enhance the proton permeability of Candida albicans membranes.* Biosci Biotechnol Biochem, 1999. **63**(7): p. 1246-52.
8. Orr, S.T., et al., *Mechanism-based inactivation (MBI) of cytochrome P450 enzymes: structure-activity relationships and discovery strategies to mitigate drug-drug interaction risks.* J Med Chem, 2012. **55**(11): p. 4896-933.
9. Tung, R., *The development of deuterium-containing drugs*, in *Concert Pharmaceuticals*. 2005.
10. Yu, L.J., et al., *Identification of a novel glutathione adduct of diclofenac, 4'-hydroxy-2'-glutathion-deschloro-diclofenac, upon incubation with human liver microsomes.* Drug Metab Dispos, 2005. **33**(4): p. 484-8.
11. Nelson, S.D. and W.F. Trager, *The use of deuterium isotope effects to probe the active site properties, mechanism of cytochrome P450-catalyzed reactions, and mechanisms of metabolically dependent toxicity.* Drug Metab Dispos, 2003. **31**(12): p. 1481-98.
12. Xu, G., et al., *Design, synthesis, and biological evaluation of deuterated C-aryl glycoside as a potent and long-acting renal sodium-dependent glucose cotransporter 2 inhibitor for the treatment of type 2 diabetes.* J Med Chem, 2014. **57**(4): p. 1236-51.
13. Eldrup, A.B., et al., *Structure-based optimization of arylamides as inhibitors of soluble epoxide hydrolase.* J Med Chem, 2009. **52**(19): p. 5880-95.

Chapter 6

In vivo efficacy and pharmacokinetics evaluation

6.1. Introduction

UCP1006 is a third generation propargyl-linked antifolates that potently inhibits the dihydrofolate reductase (DHFR) enzymes from *S. aureus* (SaDHFR) and *C. glabrata* (CgDHFR) and inhibits the growth of these species *in vitro* [1-2]. To evaluate the *in vivo* effectiveness of UCP1006, an established murine model of *S. aureus* bacteremia caused by a community-acquired MRSA isolate and an established murine model of invasive candidiasis caused by *C. glabrata* were used through collaboration with Dr. Nathan Wiederhold's research group in The University of Texas Health Science Center at San Antonio (UTHSCSA). Initial dose tolerability/pharmacokinetic experiments in which UCP1006 is administered by intraperitoneal injection were conducted. The *in vivo* antibacterial activity of UCP1006 was compared to vancomycin and the *in vivo* antifungal efficacy of UCP1006 was compared to fluconazole and caspofungin.

6.2. Evaluate UCP1006 as treatment for MRSA bacteremia

6.2.1 *S. aureus* isolate preparation and murine bacteremia model

LAC300, a USA300 community-acquired MRSA strain, was used in this study. This is a well-characterized clinical isolate that is known to cause lethal, disseminated disease when inoculated intravenously [3-4]. BALB/c mice were inoculated via the lateral tail

vein in order to establish *S. aureus* bacteremia. Each animal was challenged with ~6 x 10^7 bacterial cells in the survival arm and ~1 x 10^7 cells in the tissue burden arm. These two different inocula sizes were used as the higher inoculum results in a rapid but consistently lethal infection, while the lower inoculum allows for the comparison of tissue burden reductions among different groups at a predetermined time point. Following inoculation, mice were monitored until day 21 to assess survival.

6.2.2 Preparation of UCP1006 HCl salt

UCP1006 was prepared by dissolving the monohydrochloride salt powder in DMSO to concentrations of 25, 50 and 100 mg/mL. The DMSO stocks were diluted 50-fold into a sodium acetate buffer that is isotonic with 157 mM Na^+ and 16 mM acetate containing 0.1% hydroxypropylmethylcellulose (HPMC) (157 mM Na^+ = 141 mM NaCl and 16 mM NaAcetate) to final concentrations of 2, 1 and 0.5 mg/mL, and the final concentration of DMSO was 2%. These concentrations (0.5, 1, and 2 mg/mL) correspond to dosages of 4, 8, and 16 mg/kg. The DMSO stocks of UCP1006 were frozen and shipped on dry ice to UTHSCSA along with the sodium acetate buffer. For each day of dosing UTHSCSA was freshly prepare the dilutions of UCP1006 in the sodium acetate buffer to the concentrations listed above. In the infection model, the commercially available intravenous preparation of vancomycin was used and prepared according to the package insert.

6.2.3 Antibacterial activity testing strategy

UCP1006 as monotherapy for *S. aureus* bacteremia was evaluated with vancomycin serveing as the positive control. This vancomycin treatment regimen has been shown to improve survival in the murine model of staphylococcal bacteremia and mimic the pharmacokinetics (AUC and Cmax) achieved with the commonly used dose of 1 g every 12 hours in humans, respectively [5]. Treatment was administered 4 hours post intravenous challenge, and mice were randomized into one of five treatment groups as described below and listed in Table 1:

1) Placebo controls – 0.1% HPMC IP injection twice daily

2) UCP1006 4 mg/kg by IP injection twice daily

3) UCP1006 8 mg/kg by IP injection twice daily

4) UCP1006 16 mg/kg by IP injection twice daily

5) Vancomycin 110 mg/kg by SC injection twice daily

Survival and tissue burden arms were included. In the survival arm, antibacterial therapy was continued through day 6 post-inoculation. Mice were then monitored off therapy at least twice daily to prevent and minimize unnecessary pain or distress until day 21 post-inoculation. Moribund animals were identified by the criteria listed above, and any animal demonstrating > 1 of these will be humanely euthanized.

In the tissue burden arm, treatment was continued for four days. One day post-treatment, mice were humanely euthanized, and the target organs (e.g., kidneys, liver, and brains) were harvested, weighed, and homogenized in sterile saline. Ten-fold serial

dilutions of the homogenates were prepared in sterile saline and plated onto TSA plates. The plates were incubated at 37°C for 24 hours, and the CFU/g of each tissue was determined. In addition, organs were also collected from mice as they succumb to infection and in those that survive to day 21 and tissue burden were measured as described above.

Table 1. Number of mice per group for the survival and tissue burden arms.

Group	Survival Arm	Tissue Burden Arm
Placebo Controls	10	10
UCP1006 4 mg/kg IP BID	10	10
UCP1006 8 mg/kg IP BID	10	10
UCP1006 16 mg/kg IP BID	10	10
Vancomycin 110 mg/kg SC BID	10	10
Total Animals	**50**	**50**

6.2.4 Pharmacokinetics analysis of UCP1006 after pre-exposure

To evaluate the tolerability/pharmacokinetics of UCP1006, a preliminary experiment was conducted using uninfected mice. Unlikely traditional pharmacokinetics evaluation, due to the limit availability of drug, a PK assessment using a tolerability experiment setup with 5 days pre-drug exposure was performed. There were 18 animals in each dosage group. Mice were administered UCP1006 at doses of 4, 8, or 16 mg/kg twice

daily IP injection for 5 days same as the tissue burden assay. At specific time points following the last dose (0.5, 1, 2, 4, 8 and 12 hours), blood and kidneys were collected from 3 mice per time point in each group. The blood was collected into EDTA tubes by cardiac puncture, and within 15 minutes, the blood samples were centrifuged (3000 g x 5 minutes) and the plasma separated and frozen. Plasma and kidney samples were maintained at -80°C and shipped frozen to the University of Connecticut. UCP1006 concentration in mice plasma samples was determined by LC-MS. Pharmacokinetics parameters of UCP1006 were estimated by compartmental analysis using the program WINNONLIN.

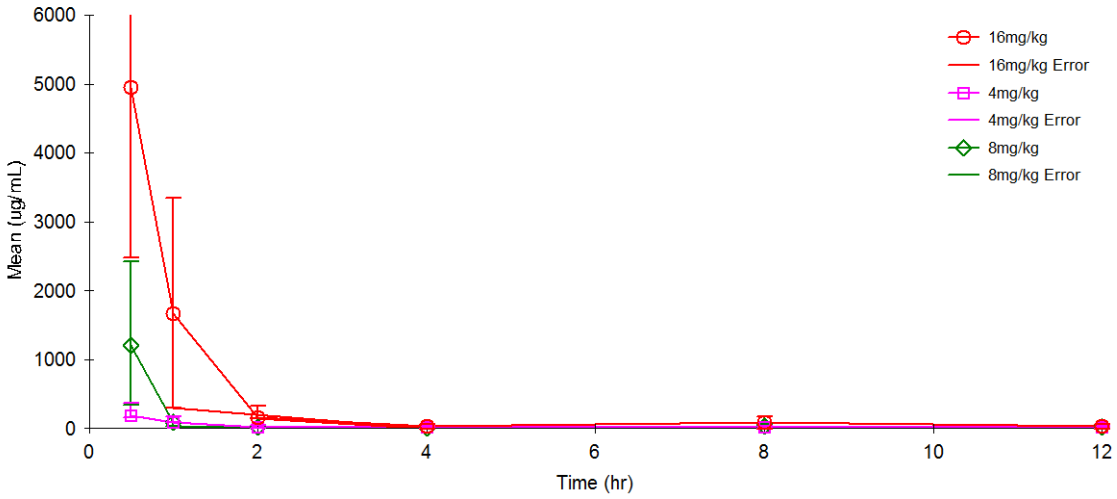

Figure 1. Profile of plasma concentration versus time of UCP1006 in mice

UCP1006 was well tolerated at all testing dosages and no significant adverse effects were observed. The pharmacokinetic parameters of UCP1006 following IP injections after 7days bi-daily exposure at 4mg/kg, 8mg/kg and 16mg/kg in mice are summarized in figure 1 and table 2. Overall, UCP1006 underwent fast clearance in mice. Whole

body clearance of UCP1006 also exhibited a dose dependant pattern, with CL value 254.91 mL/min/kg, 89.36 mL/min/kg and 39.4 mL/min/kg at 4, 8 and 16 mg/kg dosages, respectively. The dose dependent difference in drug intrinsic clearance might result from potent CYP inhibition (discussed in later chapters). The intrinsic half-life of UCP1006 is short and is similar despite different dosages (0.32~0.5hr). A separated PK study using UCP1006 without drug pre-exposure at 2 mg/kg using IV administration suggested similar (comparing 4 mg/kg IP with 7 days drug exposure) intrinsic half-life (0.41hour). However, slower clearance was observed (32.3 mL/min/kg). Therefore, a significant CYP induction or non-CYP mediated drug clearance may play an important role.

Due to the unexpected fast clearance and relative long sampling interval, a plasma concentration error was observed. The estimated Cmax of UCP1006 at 16 mg/kg is 14.78 μg/mL, about 190 fold higher than the *in vitro* MIC value against *S. aureus*. Therefore, even with relative low drug exposure, UCP1006 is still selected for later *in vivo* efficacy testing in MRSA infection murine model.

Table 2. Pharmacokinetics of UCP1006 in mice at 4, 8 and 16mg/kg

Dosage	4mg/kg	8mg/kg	16mg/kg
Half-life (hr)	0.50	0.34	0.32
AUC[a] (hr*μg/mL)	0.26	1.49	6.77

Cmax[b] (μg/mL)	0.37	3.03	14.78
Clearance (mL/min/kg)	254.91	89.36	39.40
Vss[c] (L/kg)	10.84	2.64	1.08

[a] Area under curve

[b] Estimated max concentration

[c] Steady state volume of distribution

6.2.5 *In vivo* antibacterial activity evaluation of UCP1006

UCP1006 was evaluated in MSRA infected mouse model as described above. However, the testing compound did not effectively clear the bacterial infection at any dosage tested. None of the animals in either survival or tissue burden arm survived. Possible reasons for UCP1006 this lack of potent antibacterial activity *in vivo* are low drug exposure due to the fast intrinsic clearance or the high level of thymidine in mouse. The plasma thymidine concentration in mice is around 1μM, over 10 times higher than human [6]. High levels of thymidine can be converted to TMP via thymidine kinase, therefore, bypassing DHFR inhibition blockade of folate biosynthesis pathway in mice [7].

6.3. Evaluate UCP1006 as treatment for candidiasis

Similar to antibacterial activity testing, antifungal potency of UCP1006 was assessed using a developed murine model of invasive candidiasis caused by *C. glabrata* in

collaboration with Dr. Wiederhold at UTHSCSA. With improved formulation, a higher administration dosage was achieved at 16, 32 and 48 mg/kg. A preliminary PK and tolerability experiment was conducted with uninfected immunosuppressed mice. The testing strategy and animal numbers were similar as described above. Previous study indicated that UCP1006 has a short intrinsic half-life in mouse. Therefore, short initial sampling time points were selected to achieve better PK estimation accuracy. Blood samples were collected at 0.17, 0.5, 1, 2, 4 and 12 hours after the last dose and plasma samples were isolated for drug quantification.

UCP1006 was well tolerated at the 16 mg/kg in the new formulation. However, mild to moderate toxicity (ruffled fur and altered locomotion after dosing) was observed at 32 and 48 mg/kg. One animal in the 48mg/kg group died during the tolerability testing. At 32mg/kg, UCP1006 posed a similar intrinsic clearance value (50.06mL/min/kg) as observed before in 16mg/kg dosage group, with 0.38 hr half-life and steady state volume of distribution (Vss) 1.78 L/kg. The calculated AUC and Cmax both increased to 9.68 hr* μg/mL and 17.84 μg/mL, respectively. However, at 48mg/kg, the PK profile did not fit in the one compartment IV bolus model as before. Significant drug accumulation was observed up to 4hours after dosing.

UCP1006 at 32mg/kg was selected for *in vivo* efficacy evaluation. The efficacy was determined by a kidney fungal burden assay similar to the tissue burden arm testing as described above. However, no statistical significance was achieved when the treatment and control groups were compared, suggesting UCP1006 failed to clear the *C. glabrata*

infection. Possible reasons are similar as described before due to the low drug exposure and high thymidine level in mouse. To better assess the *in vivo* efficacy of propargyl-linked compounds, better drug exposure and eliminated high thymidine salvage effects are both critical.

6.4. Evaluate the tolerability and PK profile of UCP1063

With extended *in vitro* microsomal metabolic stability ($t_{1/2}$=135mins with MLM) and improved antibacterial potency (MIC=0.02μg/ml agasint MRSA), UCP1063 was expected to have better drug exposure and selected as a new investigational agent for *in vivo* efficacy testing. A similar testing approach using the LAC300 MRSA strain generating bacteremia in murine model was conducted. A pilot PK and tolerability testing was also included for investigating the novel delivery formulation and high dosage (up to 128mg/kg). Instead of using IP injection, oral gavage administration was used to achieve highest possible dosages at 16, 64 and 128 mg/kg (18, 5 and 5 animals each). Another group of 18 mice using IP injection at 16 mg/kg was also included for bioavailability determination.

UCP1063 was well tolerated at 16 mg/kg. At 64 mg/kg, all five animals survived the 7 days treatment. However, significant weight loss was observed for the animals, suggesting the dosage cannot be used for efficacy testing. At 128 mg/kg, one mouse died after two doses and the other four animals experienced severe adverse effects and had to be euthanized shortly after the third dose.

Table 3. Pharmacokinetics of UCP1063 in mice at 16 mg/kg through IP and PO administration

Administration	IP	PO
Half-life (hr)	0.33	0.19
AUC (hr*μg/mL)	4.90	0.41
Cmax (μg/mL)	10.16	1.44
Clearance (mL/min/kg)	54.37	658.42
Vss (L/kg)	1.57	11.10

The pharmacokinetic parameters of UCP1063 at 16mg/kg through IP and PO administration are summarized in Table 3. Although UCP1063 exhibited higher metabolic stability than UCP1006 *in vitro*, the two compounds have similar intrinsic half-lives in the mouse (around 0.3 hour at 16mg/kg IP). This suggests that the improvement of *in vitro* metabolic stability with microsomes is an artifact and may be due to CYP inhibition at relatively high concentrations. The bioavailability of UCP1063 is 8.3 %, significantly lower than UCP1006 (82.5 % in rats). Due to unexpected short metabolic half-life, initial sampling time points were long. The first sampling time was determined

at 30 minutes after last dosage. With calculated intrinsic half-life shorter than 20 minutes, data collected for the oral administration group did not detect the initial phase of drug exposure and therefore, may have poor estimation. Even with potent antibacterial activity *in vitro*, UCP1063 showed similar drug exposure at 16mg/kg as UCP1006. At higher testing dosage (64 and 128mg/kg), UCP1063 was not tolerated in animals, which suggested no increased drug exposure can be achieved through high dosage administration. Therefore, additional efficacy study in MRSA infected murine model for UCP1063 was not pursued at this moment.

6.5. Conclusions

To evaluate the *in vivo* efficacy of UCP1006 against bacteremia and candidiasis caused by MRSA and *C. glabrata*, murine infectious models were used with the collaboration with Dr. Wiederhold's group in UTHSCSA. UCP1006 exhibited good tolerability at 32mg/kg and lower dosages. PK evaluation after 7 days bi-daily IP administration suggested that UCP1006 was quickly cleared in mouse with an intrinsic half-life of 0.3 hours. Due to the low drug exposure and high level thymidine level in murine animals, UCP1006 did not effectively eliminate bacteremia and candidiasis in infected animals. However, an independent study using similar murine infection model with thymidine kinase knockout MRSA strain showed efficacy of UCP1021 with an ED_{50} value around 4mg/kg (data not shown).

UCP1063 exhibited better metabolic stability and enhanced antibacterial activity compard to UCP1006 *in vitro*. Nevertheless, no significant drug exposure improvement

was observed *in vivo*. In addition, UCP1063 was less orally bioavailable and less tolerated. Therefore, additional efficacy testing of UCP1063 in MRSA infected animals was discontinued.

Although highly potent and tolerable propargyl-linked antifolates with excellent PK properties are still under development, our knowledge of improving potency and ADME performance is constantly improving. The research described here has led to identification of compounds with good aquous solubility, *in vitro* metabolic stability and low CYP inhibition. Next steps should incorporate more quantitative analysis of *in vitro* clearance and establish better *in vitro* and *in vivo* correlation for compound rank ordering and drug candidate selection.

6.6. Acknowledgements

I would like to Narendran Dayanan, Dr. Kishore Viswanathan and Dr. Santosh Keshipeddy for compound synthesis. Also special thanks to Dr. Michael Lombardo for animal plasma sample preparation.

6.7. References

1. Viswanathan, K., et al., *Toward new therapeutics for skin and soft tissue infections: propargyl-linked antifolates are potent inhibitors of MRSA and Streptococcus pyogenes.* PLoS One, 2012. **7**(2): p. e29434.
2. N, G.D., et al., *Propargyl-Linked Antifolates are Dual Inhibitors of Candida albicans and Candida glabrata.* J Med Chem, 2014. **57**(6): p. 2643-56.
3. Spellberg, B., et al., *The antifungal vaccine derived from the recombinant N terminus of Als3p protects mice against the bacterium Staphylococcus aureus.* Infect Immun, 2008. **76**(10): p. 4574-80.
4. Lin, L., et al., *Th1-Th17 cells mediate protective adaptive immunity against Staphylococcus aureus and Candida albicans infection in mice.* PLoS Pathog, 2009. **5**(12): p. e1000703.

5. Reyes, N., et al., *Efficacy of telavancin in a murine model of bacteraemia induced by methicillin-resistant Staphylococcus aureus.* J Antimicrob Chemother, 2006. **58**(2): p. 462-5.
6. Jackman, A.L., et al., *Modulation of anti-metabolite effects. Effects of thymidine on the efficacy of the quinazoline-based thymidylate synthetase inhibitor, CB3717.* Biochem Pharmacol, 1984. **33**(20): p. 3269-75.
7. Jackman, A.L., *Antifolate Drugs in Cancer Therapy*. 1999: Humana Press.

Chapter 7

CYP inhibition and *in vivo* drug exposure optimization

7.1. Introduction

Cytochrome P450 (CYP) enzymes play a critical role in xenobiotic metabolism [1]. Out of many different isoforms within the CYP superfamily, CYP3A4 and CYP2D6 are particularly important and contribute to the metabolism of about 58% of common drugs on the market [2]. Drugs that inhibit CYP may impact the pharmacokinetic profile of other drugs and can result in serious drug-drug interactions [3]. Therefore, it is important to monitor CYP inhibition during the drug discovery process. During the initial CYP inhibition assessment, it is commonly accepted that compounds with IC_{50} values higher than 10 μM against major CYP isoforms are weak CYP inhibitors; compounds with 3 μM $<IC_{50}<$ 10 μM are moderate CYP inhibitors; while compounds with $IC_{50}<$ 3 μM are strong CYP inhibitors [4].

Previous chapters described that early lead propargyl-linked antifolates were associated with fast metabolic clearance. Initial lead optimization effort significantly increased the metabolic stability. However, the *in vivo* PK testing suggested no drug exposure improvement even though UCP1063 exhibited a 3 fold longer half-life when compared to UCP1006 *in vitro*. The experimental conditions used were metabolic incubation with mouse or human liver microsomes with a relatively high concentration of testing compounds (5 μg/mL). With potent CYP inhibition, the improved *in vitro* metabolic

stability may likely be due to the artificial effects of self inhibition to metabolic CYP enzymes. In this chapter, the CYP inhibition of lead propargyl-linked compounds to two major CYP isoforms (CYP3A4 and CYP2D6) will be tested. *In vitro* metabolic half-lives will be further evaluated at a lower compound testing concentration (0.5µg/mL). Careful structure-property relationship (SPR) analysis will lead to the identification of candidate compounds with better metabolic stability and lower CYP inhibitory activity for future *in vivo* testing.

7.2. Evaluate CYP inhibition of lead propargyl-linked antifolates

CYP inhibition of lead compounds was tested against CYP3A4 and CYP2D6 using a fluorescent based assay. Non-fluorescent isoform specific substrate 3-[2-(N, N-diethyl-N-methylammonium) ethyl]-7-methoxy- 4- methyl-coumarin (AMMC) was incubated with baculovirus insect cells (BTI-TN-5B1-4) expressed human CYP2D6 enzyme (Supersomes^{TM}) generating fluorescent metabolite 3-[2-(N,N-diethylamino)ethyl-7-hydroxy-4-methylcoumarin (AHMC) (Fig 1A.)[5]. With the presence of testing compounds as CYP2D6 inhibitors, the metabolism of AMMC is suppressed and will generate the less fluorescent metabolite AHMC. The CYP inhibition was quantified by comparing a negative control (without testing compounds) in a dose dependent manner (Fig 1B.). Similarly, the CYP3A4 inhibition assay was performed using Supersomes^{TM} with fluorogenic substrate 7-benzyloxyquinoline (BQ) and fluorescent metabolite 7-hydroxyquinoline (HQ)[6]. The IC_{50} value was calculated with standard curve generated with fluorescent metabolite AHMC or HQ.

a.

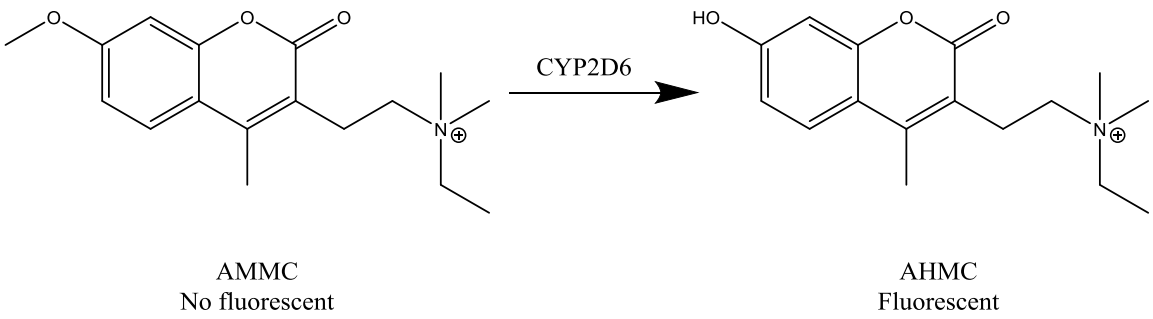

b.

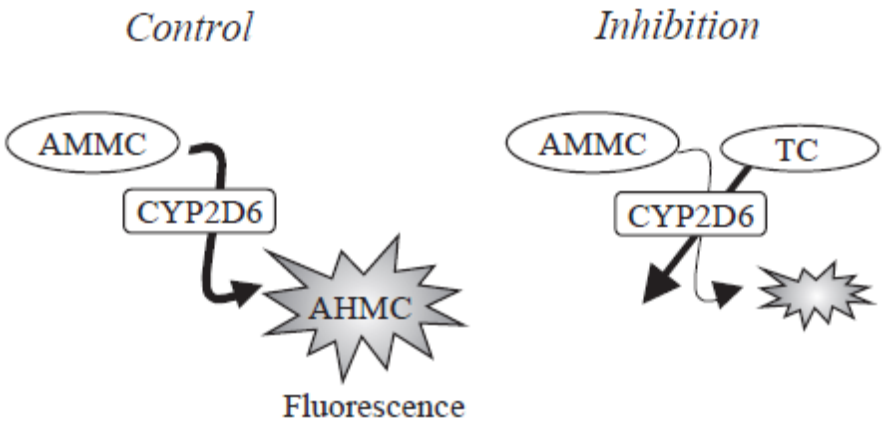

Figure 1. a, structures of AMMC and AHMC; b, inhibition pattern in the incubation medium including recombinant CYP2D6 supersomes with TC (test compound) as inhibitor.

Table 1 lists the CYP3A4 and CYP2D6 IC_{50} values and *in vitro* microsomal metabolic half-life values with MLM and HLM of lead propargyly-linked antifolates at 5µg/mL. Most of these compounds (23 compounds total) are potent CYP inhibitors against CYP3A4 with IC_{50} values ranging from <0.01 µM to 0.56 µM (excluding UCP1031, UCP1055, UCP1076 and UCP1077) and moderate CYP2D6 inhibitors with IC_{50} values ranging from 1.41 µM to >29 µM (excluding UCP1038, UCP1070 and UCP1075). Noticeably, UCP1038 exhibited potent CYP inhibition against both CYP3A4 (100% inhibition at 0.02 µM) and

CYP2D6 (IC_{50}=0.07 μM). This is likely related to a potential for covalent binding to the heme group from CYP after bioactivation [7]. UCP1070, the deuterium substituted analogue, was designed to slow down bioactivation of the C-H bond at the dioxolane and ideally should reduce the CYP inhibition potential. Despite the fact that UCP1070 significantly reduced the CYP3A4 inhibition (IC_{50}=0.04 μM), it is a more potent CYP2D6 inhibitor (IC_{50}=0.01 μM) than UCP1038.

Table 1. Structure, CYP inhibition and *in vitro* microsomal metabolic half-life of lead propargyl-linked DHFR inhibitors.

Cmpd#	Structure	CYP3A4 IC_{50} (μM)	CYP2D6 IC_{50} (μM)	$t_{1/2}$ MLM (min)	$t_{1/2}$ HLM (min)
UCP1021	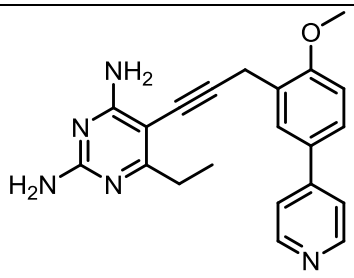	0.21	1.55	31	81
UCP1031	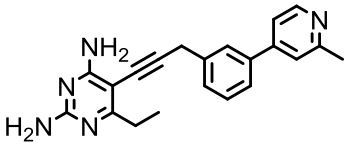	2.4	N/A	N/A	N/A
UCP1038	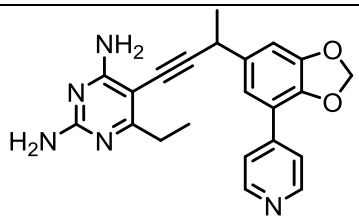	<0.02	0.07	79	270

UCP1040	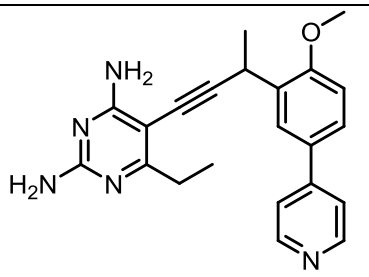	0.02	1.65	65	87
UCP1047	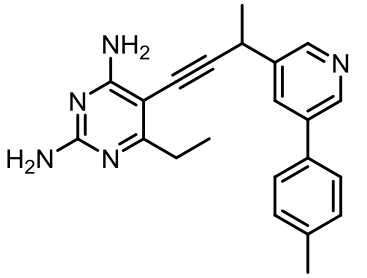	0.17	N/A	N/A	N/A
UCP1052	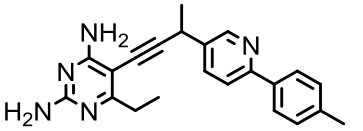	0.56	>5.6	68	N/A
UCP1055	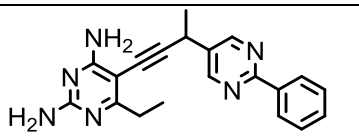	5.76	>29	101	N/A
UCP1061	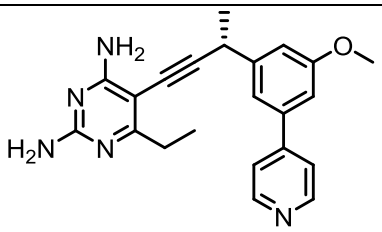	0.06	N/A	37	100
UCP1062	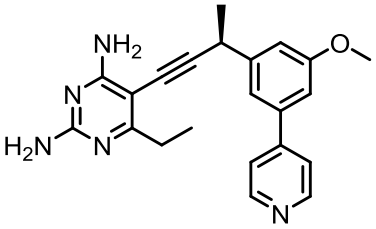	0.02	1.41	37	75

UCP1063	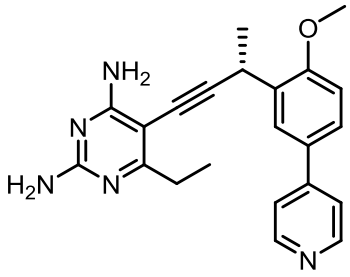	0.05	N/A	135	146
UCP1064	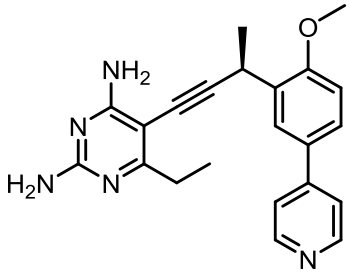	0.07	N/A	69	135
UCP1066	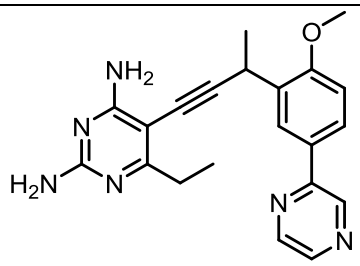	0.45	8.17	24	69
UCP1067	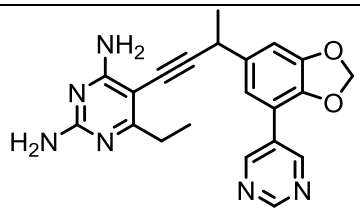	0.04	N/A	15	N/A
UCP1070	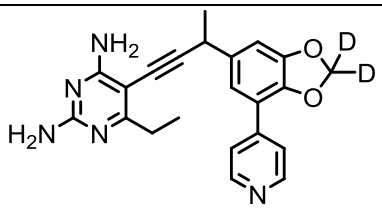	0.04	0.01	91	101
UCP1072	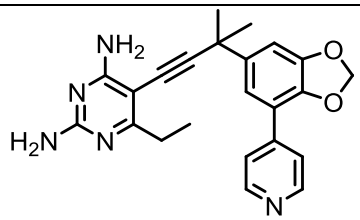	0.02	N/A	N/A	N/A

UCP1074	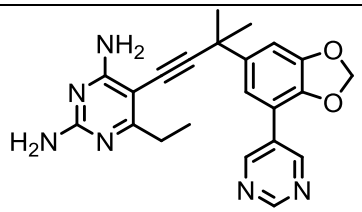	0.02	N/A	N/A	N/A
UCP1075	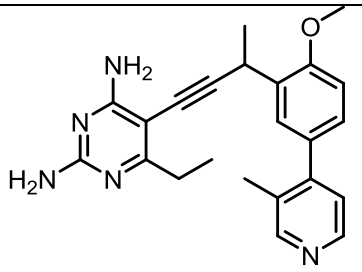	<0.01	0.16	N/A	N/A
UCP1076	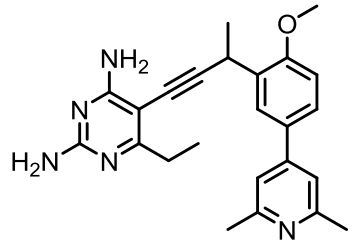	3.65	9.81	35	82
UCP1077	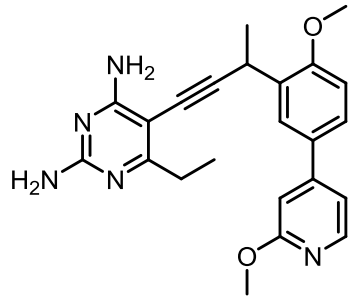	2.65	13.21	20	340
UCP1079	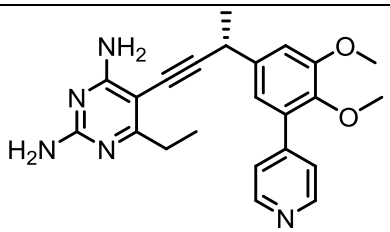	0.21	9.25	260	N/A
UCP1080	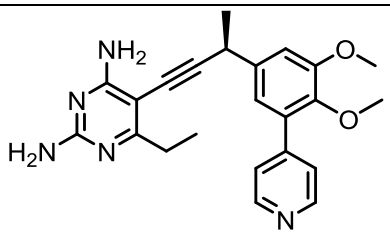	0.29	3.82	71	N/A

UCP1082	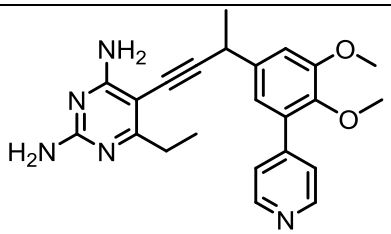	0.20	2.54	213	N/A
UCP1084	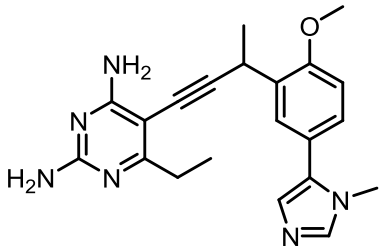	<0.01	N/A	N/A	N/A

It is well accepted that compounds that contain the heme-ligating pyridine group are common CYP inhibitors [8]. UCP1075, UCP1076 and UCP1077 were designed to reduce the CYP inhibition potential with diminished heme binding by adding bulky hydrophobic groups on the exposed pyridine ring. Surprisingly, UCP1075 exhibited even stronger CYP inhibition of both CYP3A4 (IC_{50}<0.01 μM) and CYP2D6 (IC_{50}=0.16 μM) compard to UCP1040 (CYP3A4 IC_{50}=0.02 μM and CYP2D6 IC_{50}=1.65 μM). The 2' methy substitution on the pyridine may have reduced the flexibility of the distal pyridine ring or enhanced the CYP binding with increased hydrophobicity, therefore resulting in a better fit the molecule into the CYP3A4 and CYP2D6 binding pocket and stronger CYP inhibition. In contrast, dimethyl (UCP1076) and methoxy (UCP1077) protected pyridine significantly reduced both CYP3A4 (IC_{50}=3.65 μM and IC_{50}=2.65 μM) and CYP2D6 (IC_{50}=9.81 μM and IC_{50}=13.21 μM) inhibition. UCP1031, featuring a single methyl protected pyridine, also shows weaker CYP3A4 inhibition (IC_{50}=2.4 μM). Despite the difference at the linker region and exposed phenyl B-ring, a single methyl group next to a pyridine nitrogen

atom seems to sufficiently reduce the heme binding propensity. Overall, blocking the open distal pyridine with bulky hydrophobic functional groups next to the nitrogen atom seems a viable strategy to reduce CYP3A4 and CYP2D6 inhibition for propargyl-linked antifolates.

Evidently, the improvement in CYP inhibition for UCP1076 and UCP1077 also associates with decreased metabolic half-life ($t_{1/2}$=35 min and 20 mins, respectively). A metabolite identification study of UCP1076 also suggested that the dimethyl protection eliminated pyridine *N*-oxdiation, one of the two predominant metabolic routes. With major metabolic route blocked and decrease in microsomal stability, it implicates that the previous described metabolic improvement at high testing concentration may be an artificial effect from self inhibition of CYPs. This is also consistent with *in vivo* PK testing results of UCP1006 and UCP1063 (chapter 6). To justify this hypothesis, the metabolic half-life of lead compounds will be further evaluated at a lower concentration (0.5μg/mL) with MLM and HLM.

7.3. Determine metabolic half-life at low testing concentration

Single time point metabolic stability testing as previously described is a common experimental approach to rank order lead compounds [9]. Due to instrumental restraints, the more accessible HPLC-UV system poses a detection limit at ~0.5μg/mL. Therefore, the initial testing concentration was selected at 5 μg/mL. CYP inhibition testing indicated that several lead compounds are potent CYP3A4 and CYP2D6 inhibitors.

Therefore, a more comprehensive metabolic half-life evaluation approach with lower compound testing concentration is needed. To achieve low testing concentration detection, a UHPLC-MS bioanalytical method to quantify testing compounds in a time dependent manner was adopted. The new MS based detection limit can reach as low as 10 ng/mL.

Table 2. *In vitro* microsomal metabolic half-life of lead propargyl-linked DHFR inhibitors at 5 µg/ml and 0.5 µg/ml.

Cmpd#	Structure	$t_{1/2}$ MLM @5µg/ml (min)	$t_{1/2}$ MLM @0.5µg/ml (min)
UCP1038	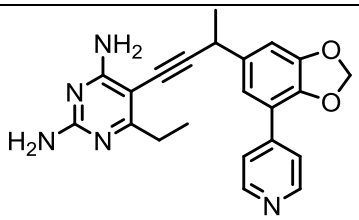	79	14
UCP1063	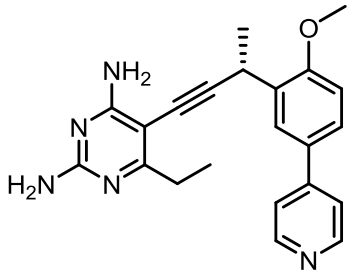	135	14
UCP1064	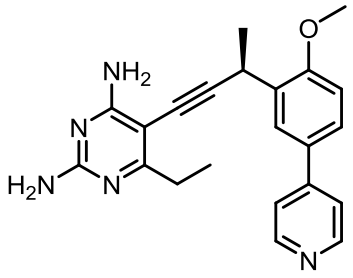	69	5

UCP1070	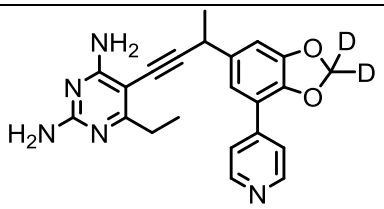	91	13
UCP1076	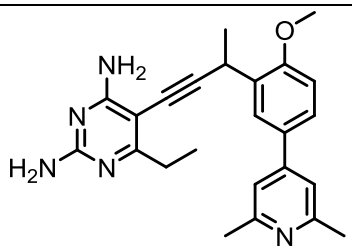	35	8
UCP1079	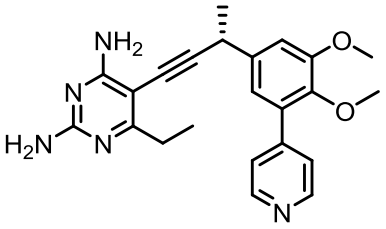	260	13
UCP1080	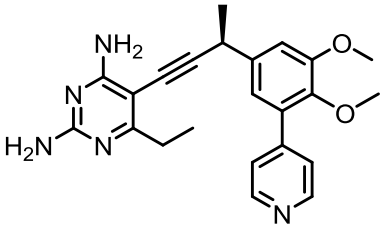	71	7

Several lead compounds with promising metabolic half-life at 5 µg/ml were selected for metabolic stability testing at a lower concentration (Table 2.). All the testing compounds exhibited a dramatic decrease in metabolic half-life at lower concentration (5~14 mins). For example, UCP1063 showed a metabolic half-life of 14 minutes at 0.5 µg/mL compared with 134 minutes at 5 µg/mL. No difference in metabolic stability between UCP1038 and UCP1070 was observed; suggesting that the deuterium substitution on the dioxolane methylene group may have only slowed the reactive intermediate formation rather than increased the overall microsomal stability. Two

pairs of single enantiomers were tested; UCP1063 and UCP1079 (both S-enantiomers) exhibited better metabolic stability compared to their R- enantiomers. However, the margin of difference was relatively small and the mechanism is still to be determined.

It is noticeable that the previously recognized improvement in metabolic stability was likely an artificial effect from the strong CYP inhibition and this improvement was not repeated when tested at a lower substrate concentration. This also explained that UCP1063 had similar *in vivo* metabolic half-life and drug exposure compared to UCP1006, despite their significant *in vitro* half-life differences. Even with one major metabolic route diminished, UCP1076 also showed a significantly shorter metabolic half-life at lower concentration. Taken together, blocking the primary metabolic route (pyridine-*N*-oxidation) of these propargyl-linked antifolates is not sufficient to greatly improve their overall intrinsic metabolic stability. Therefore, further metabolism optimization to block multiple metabolic "soft spots" and decrease CYP binding through reducing hydrophobicity will be explored.

7.4. Optimization of metabolic stability at lower testing concentration

Previous CYP inhibition testing suggested that with the presence of the exposed pyridine, most lead compounds were potent CYP3A4 or CYP2D6 inhibitors. With low testing concentrations of 0.5 μg/mL, phase I metabolic half-life of all lead compounds were equal or lower than 14 mins. To further optimize the metabolic stability of lead propargyl-linked antifolates while minimizing the CYP inhibitory propensity, approaches to block the metabolism "soft spots" and decrease lipophilicity were implemented.

7.4.1 Increase metabolic stability using deuterated dioxolane and dioxane

The early dioxolane compound UCP1038 exhibited potent antibacterial activity against MSRA (MIC=0.08 μg/mL). However, it was also a strong CYP inhibitor with 100% CYP3A4 inhibition at 0.02μM and IC_{50} values of 0.07 μM against CYP2D6. Aiming to reduce the CYP inhibition, the deuterium substituted derivative UCP1070 was synthesized [10]. Despite the improvement of CYP3A4 inhibition (IC_{50}=0.04 μM), UCP1070 retained potent CYP2D6 inhibitory activity (IC_{50}=0.01 μM). To further investigate the mechanism of CYP inhibition of these dioxolane containing compounds and potentially develop better lead compounds, UCP1112 and UCP1114 were designed and synthesized (Fig 2.).

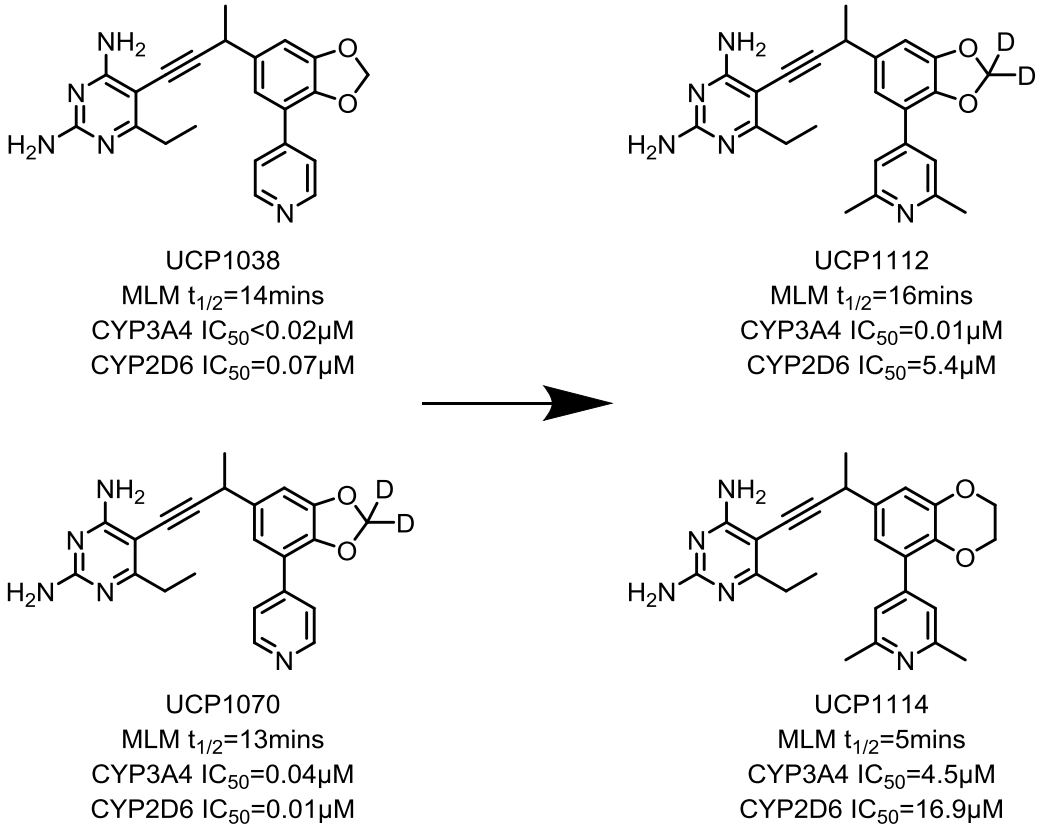

Figure 2. Structure, MLM half-life and CYP inhibition activity of UCP1038, UCP1070, UCP1112 and UCP1114.

As previously described, pyridine containing compounds are common CYP inhibitors due to the metal chelating activity and this CYP inhibition tendency can be weakened with hydrophobic decoration next to pyridine nitrogen atom. Dimethyl pyridinyl substituted UCP1112 was designed to probe the CYP inhibition liability of deuterated dioxolane. Comparing to its pyridinyl analogue, UCP1112 exhibited over 500 fold reduction of CYP2D6 inhibition. Surprisingly, UCP1112 remained a potent CYP3A4 inhibitor (IC_{50}=0.01 μM). Despite high structural similarity to the dioxolane, dioxane substituted UCP1114 showed only moderate CYP3A4 and CYP2D6 inhibition (IC_{50}=4.5 μM and 16.9 μM, respectively). In addition, UCP1114 also characterized with high antibacterial potency with MIC value lower than 0.08 μg/mL against MRSA. SPR analysis clearly illustrated that the strong CYP3A4 inhibition of UCP1038 is likely a result from bioactivation of benzyl dioxolane to carbene and subsequently covalent interaction to the heme group from CYPs. The deuterium effects on the dioxolane methylene (UCP1070) effectively reduced this quasi-irreversible interaction and therefore decreased CYP3A4 inhibition was observed. With a protected pyridine, UCP1112 had a CYP3A4 IC_{50} of 0.01 μM, which suggested even the mechanism-based inactivation of benzyl dioxolane was dwindled by deuterium effects, likely strong non-covalent interactions still resulted in potent CYP3A4 inhibition. The moderate CYP3A4 and CYP2D6 inhibition of UCP1114 also supported this hypothesis. Despite the promising antibacterial activity and encouraging CYP inhibition values, UCP1114 was quickly metabolized by MLM. Additional metabolite identification studies will be important to

understand the metabolism routes and further improvement of metabolic stability is warranted.

7.4.2 Improve metabolic half-life by blocking demethylation

Lead compounds containing a 2' or 3' methoxyl group on the adjacent phenyl (UCP1006, UCP1063 and UCP1076, etc) were excellent antibacterial agents against MRSA. However, previous studies indicated poor metabolic stability. To eliminate the demethylation, one of the primary biotransformation routes, and potentially increase *in vitro* microsomal half-life, several UCP1076 analogues were synthesized.

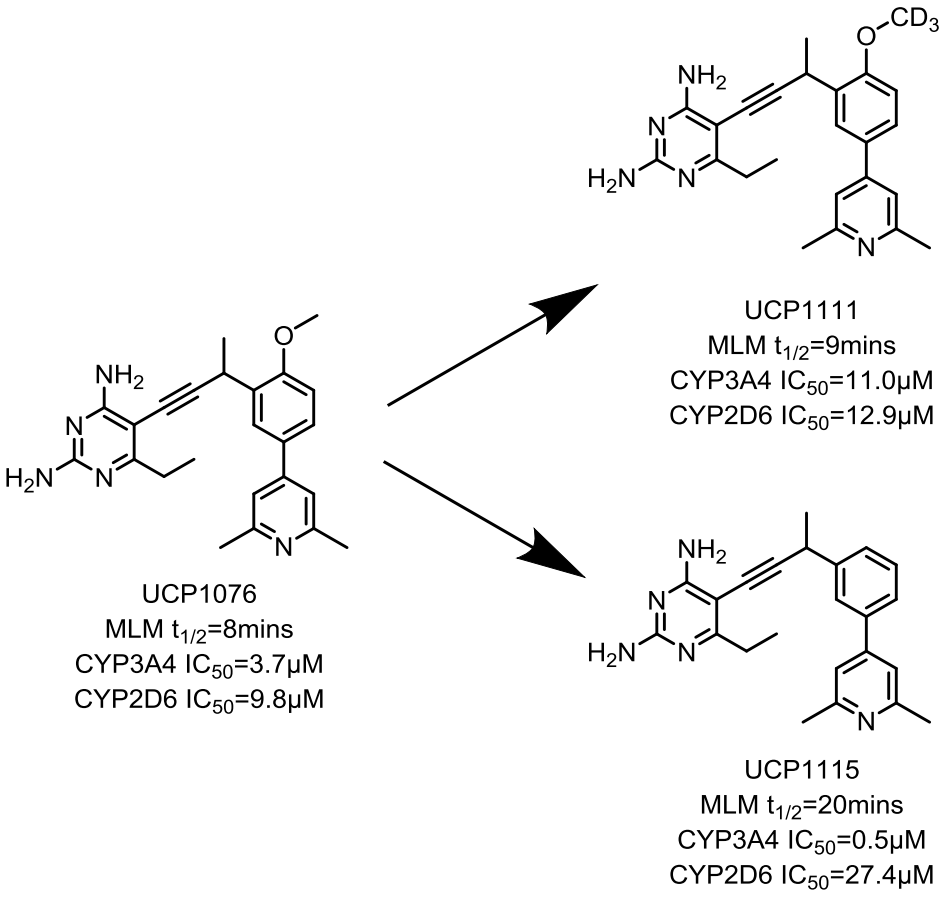

Figure 3. Structure, MLM half-life and CYP inhibition activity of UCP1076, UCP1111 and UCP1115.

Metabolite identification results suggested the only major metabolic route of UCP1076 was through demethylation on the 2' position of the adjacent phenyl ring. The deuterium substituted derivative UCP1111 was designed to reduce this reaction with a more rigid C-D bond [11-12]. Little effect of increasing metabolic half-life was observed (8 and 9 minutes), while the IC_{50} values against CYP3A4 increased from 3.7 μM to 11.0 μM. Therefore, the deuterium substitution seems to not be strong enough to drastically slow the demethylation. In the mean time, UCP1111 derivative with trifluoro methoxy or fluorine substitutions were under development. Additionally, UCP1115 with an unsubstituted adjacent phenyl group showed marginal improvement with MLM (half-life of 20 mins); however, stronger CYP3A4 inhibition (IC_{50}=0.5 μM) was also detected. Hydroxylation on the phenyl ring is likely the primary metabolic route for UCP1115, a detailed metabolite identification assessment will be performed and the hydroxylation position will be assigned with LC-MS/MS. Analogues with reduced benzyl hydroxylation will be synthesized and evaluated.

7.4.3 Optimize microsomal stability through reducing hydrophobicity

Decreased hydrophobicity usually reduces the binding of small molecule drugs to cytochrome P450s and therefore increases metabolic stability [13]. Previously described crystallographic insight of lead propargyl-linked DHFR antifolates bound to SaDHFR revealed the para and meta positions of the distal phenyl ring are solvent exposed and may tolerate polar substitutions. Two new compounds with hydrophilic

functional groups on the distal rings were therefore synthesized with the goal of prolonging metabolic half-life.

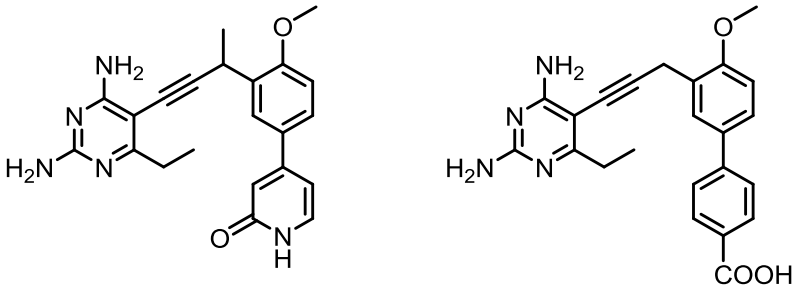

UCP1104
$LogD_{7.4}$=2.57
MLM $t_{1/2}$=16mins
CYP3A4 IC_{50}=0.8μM
CYP2D6 IC_{50}=34.6μM

UCP1106
$LogD_{7.4}$=1.44
MLM $t_{1/2}$=99mins
CYP3A4 IC_{50}>50μM
CYP2D6 IC_{50}>>50μM

Figure 4. Structure, LogD values, MLM half-life and CYP inhibition activity of UCP1104 and UCP1106.

UCP1104 and UCP1106, features pyridone and benzoic acid functional group at the distal biaryl system respectively, decrease LogD values at pH7.4 (2.57 and 1.44) compared to their pyrdine analogue (UCP1040 $logD_{7.4}$=3.44). With a pyridone group, UCP1104 shows small improvement in metabolic half-life of 16mins and potent CYP3A4 inhibition (IC_{50}=0.8 μM). A low CYP2D6 inhibition value was also observed (IC_{50}=34.6 μM). More excitingly, UCP1106, the zwitterion compound with a carboxylic acid at the meta position of the distal phenyl ring highlighted excellent ADME properties with MLM half-life of 99 mins, IC_{50} values against CYP3A4 and CYP2D6 both greater than 50μM (31% CYP3A4 inhibition and less than 5% CYP2D6 inhibition at 50 μM). In addition to its superb PK properties, UCP1106 also proved to have exceptional antibacterial activity (MIC=0.16 μg/mL) against MRSA. As the best lead compound so far, thorough

metabolite identification evaluation will be conducted and *in vivo* PK and efficacy assessment will also be performed.

7.5. Conclusions

Drugs that inhibit cytochome P450s may interfere with the PK profiles of other drugs co-administered and often cause drug-drug interactions. Pyridines containing lead propargyl-linked antifolates were confirmed potent inhibitors against CYP3A4 and CYP2D6. The strong CYP inhibition was also hypothesized to artificially prolonged the *in vitro* microsomal half-life tested with high substrate concentration. Further metabolic stability assessment with MLM using testing concentrations of at 0.5 μg/mL revealed dramatic decrease in half-life.

To diminish the CYP inhibition propensity and block metabolic soft spot, which may potentially increase *in vitro* microsomal stability, several approaches were implemented. A series of lead compounds with dimethyl protected pyridine functionality at the distal position were designed and synthesized. The hydrophobic groups next to the pyridyl nitrogen effectively reduced the non-specific metal chelating activity of pyridine resulting in decreased CYP inhibition liability. In addition, this modification also completely blocked pyridine *N*-oxidation, the primary biotransformation route of early propargyl-linked DHFR inhibitors. Despite the promising improvement of new lead compounds, their metabolic stability was still poor. UCP1115, the most stable lead in this series, has a 20 minute half-life with MLM. Thorough metabolite identification

evaluation will be performed and analogues with improved microsomal stability will be designed.

Another strategy to decrease CYP binding by reducing hydrophobicity was also explored. UCP1106, a zwitterion compound featuring a carboxylic acid group on the meta position of distal phenyl ring. This compound exhibited excellent ADME properties with MLM $t_{1/2}$=99 min and IC_{50} values of greater than 50 μM for both CYP3A4 and CYP2D6. In addition, UCP1106 also showed potent antibacterial activity with MRSA (MIC=0.15 μg/mL). As the best lead compound so far, UCP1106 will be further investigated.

7.6. Acknowledgements

I would like to thank Narendran Dayanan, Eric Scocchera, Dr. Kishore Viswanathan and Dr. Santosh Keshipeddy for compounds synthesis. Special thanks to Dr. Mike Lombardo for assistance on metabolic stability, CYP inhibition and metabolite identification testing; Stephanie Reeve for the antibacterial potency testing against *S. aureus*.

7.7. References

1. Branden, G., et al., *Structure-based ligand design to overcome CYP inhibition in drug discovery projects.* Drug Discov Today, 2014.
2. Wienkers, L.C. and T.G. Heath, *Predicting in vivo drug interactions from in vitro drug discovery data.* Nat Rev Drug Discov, 2005. **4**(10): p. 825-33.
3. Di, L., et al., *Comparison of cytochrome P450 inhibition assays for drug discovery using human liver microsomes with LC-MS, rhCYP450 isozymes with fluorescence, and double cocktail with LC-MS.* Int J Pharm, 2007. **335**(1-2): p. 1-11.
4. Kerns, E.H. and D. Li, *Drug-like Properties: Concepts, Structure Design and Methods.* Academic Press;, 2008.
5. Yamamoto, T., A. Suzuki, and Y. Kohno, *High-throughput screening to estimate single or multiple enzymes involved in drug metabolism: microtitre plate assay using a combination of recombinant CYP2D6 and human liver microsomes.* Xenobiotica, 2003. **33**(8): p. 823-39.

6. Yamamoto, T., A. Suzuki, and Y. Kohno, *High-throughput screening for the assessment of time-dependent inhibitions of new drug candidates on recombinant CYP2D6 and CYP3A4 using a single concentration method.* Xenobiotica, 2004. **34**(1): p. 87-101.
7. Orr, S.T., et al., *Mechanism-based inactivation (MBI) of cytochrome P450 enzymes: structure-activity relationships and discovery strategies to mitigate drug-drug interaction risks.* J Med Chem, 2012. **55**(11): p. 4896-933.
8. Sevrioukova, I.F. and T.L. Poulos, *Pyridine-substituted desoxyritonavir is a more potent inhibitor of cytochrome P450 3A4 than ritonavir.* J Med Chem, 2013. **56**(9): p. 3733-41.
9. Di, L., et al., *Experimental design on single-time-point high-throughput microsomal stability assay.* J Pharm Sci, 2004. **93**(6): p. 1537-44.
10. Eldrup, A.B., et al., *Structure-based optimization of arylamides as inhibitors of soluble epoxide hydrolase.* J Med Chem, 2009. **52**(19): p. 5880-95.
11. Nelson, S.D. and W.F. Trager, *The use of deuterium isotope effects to probe the active site properties, mechanism of cytochrome P450-catalyzed reactions, and mechanisms of metabolically dependent toxicity.* Drug Metab Dispos, 2003. **31**(12): p. 1481-98.
12. Tung, R., *The development of deuterium-containing drugs*, in *Concert Pharmaceuticals*. 2005.
13. Peglion, J.L., et al., *Improvement in the selectivity and metabolic stability of the serotonin 5-HT(1A) ligand, S 15535: a series of cis- and trans-2-(arylcycloalkylamine) 1-indanols.* J Med Chem, 2002. **45**(1): p. 165-76.

Chapter 8

In vitro PK properties of tropolone analogues assessment

8.1. Introduction

Hinokitiol (β-thujaplicin) (Fig 1.) is a natural product found in the heartwood of cupressaceous plants [1]. 2-hydroxy tropone (tropolone) (Fig 1.) is the prominent functional group in hinokitiol. Biological functions of tropolone derivatives include antibacterial [2], antiviral [3] and anticancer activities [4]. Strong metal chelation has been observed in tropolone analogues and is likely responsible for the various antiproliferative properties [5]. Unlike most natural products, hinokitiol is low molecular weight (MW=164), which allows extensive structural modification as a drug scaffold. A small library of tropolone analogues with substitutions at both α and β positions has been designed and synthesized in the Wright lab [6]. These tropolone-based compounds exhibit promising selective histone deacetylase (HDAC) enzymatic inhibition [7-8].

HDACs are responsible for deacetylating the amino-terminal tails of histones [9] using a zinc-catalyzed reaction. Abnormal recruitment of HDAC has been proved to be a key pathogenetic mechanism of acute promyelocytic leukemia (APL) [10]. The HDAC inhibitor vorinostat (Fig 2.) featuring a zinc-targeting hydroxamate group was approved by FDA for treatment of cutaneous T-cell lymphoma [11]. Lead compounds in the tropolone based HDAC inhibitor library display promising HDAC inhibition activity and

selectivity for HDAC2. Some lead compounds were also found to be highly potent against various T-cell lymphocyte cell lines [7].

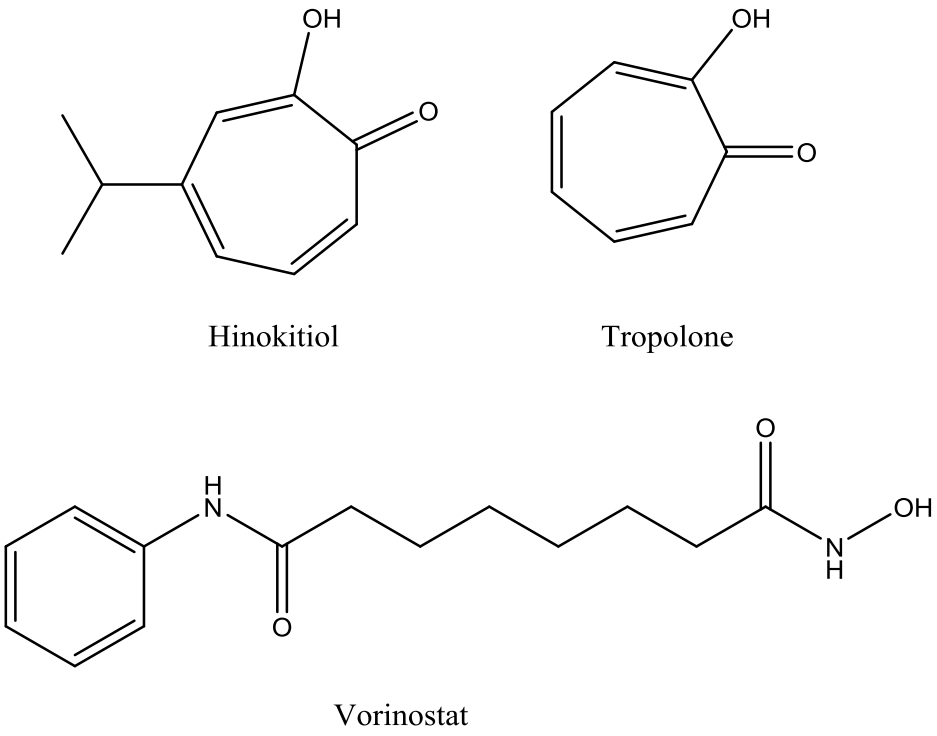

Figure 1. Structure of hinokitiol, tropolone and vorinostat.

8.2. HDAC inhibition and cytotoxicty of lead Tropolone analogues

Lead compounds alpha-phenyl tropolone and beta-phenyl tropolone (Fig 2.) both exhibited potent and selective HDAC-2 (IC_{50}=0.29 nM and 0.06 nM) and HDAC-8 inhibition (IC_{50}=1.09 nM and 1.47 nM) [7]. Promising anticancer activities were also observed in T-lymphocyte cancer cell line (Jurkat cells) with minimal cytotoxicity with non-malignant human dermal fibroblast line (hDF cells).

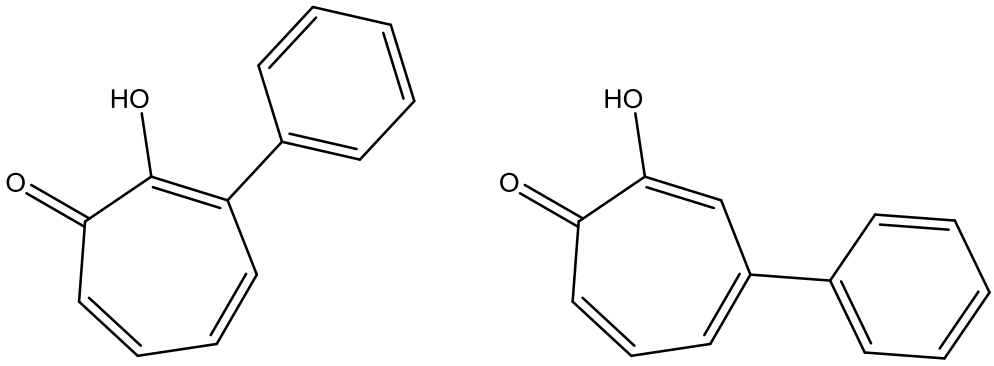

Alpha-phenyl tropolone
IC_{50} HDAC-2=0.26nM
IC_{50} HDAC-8=1.09nM
IC_{50} Jurkat cells=3.3μM
IC_{50} hDF cells=96μM

Beta-phenyl tropolone
IC_{50} HDAC-2=0.06nM
IC_{50} HDAC-8=1.47nM
IC_{50} Jurkat cells=0.67μM
IC_{50} hDF cells=>100μM

Figure 2. Structure and activity of alpha-phenyl tropolone and beta-phenyl troplone.

A recent study on the antiproliferative properties of tropolone analogues towards Jurkat cells suggested that similar to vorinostat, alpha-phenyl tropolone induced perforin overexpression and activated caspase-3/7. In contrast, alpha-phenyl tropolone modestly inhibited hyperacetylation and did not induce p21 overexpression. In addition, cell cycle arrest patterns from alpha-phenyl tropolone and vorinostat also appear different. Taken together, alpha-phenyl tropolone induced apoptosis of Jurkat cells through a mechanism distinct from vorinostat [8].

8.3. *In vitro* ADME property evaluation of lead tropolone analogues

To characterize the drug likeliness of tropolone analogues and potentially rank order compounds with better PK properties, kinetic solubility, Phase I and Phase II metabolic half-lives were evaluated with MLMs for key lead compounds.

8.3.1 Metabolic stability assessment of alpha-phenyl tropolone

Due to the strong metal chelating property, detection of unprotected tropolone analogues through HPLC fitted with reverse-phase columns is extremely difficult. Lead compound alpha-phenyl tropolone and its isomer beta-phenyl tropolone both tend to interact with the silico bead from C-18 column nonspecifically and cannot be eluted or generate strong tailing peaks, which are impossible to quantify. Multiple mobile phase and columns were tested. A protocol using both acid modifier (trifluoroacetic acid up to 0.1%) and metal chelating agent (acetylacetone up to 0.1%) were developed.

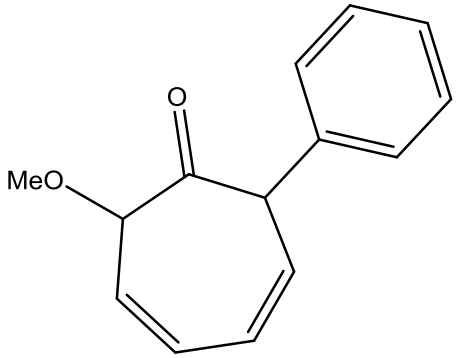

Protected Alpha-phenyl tropolone

Figure 3. Structure of protected alpha-phenyl tropolone

Alpha-phenyl tropolone, the most potent lead against various T-lymphocyte cancer cell lines, exhibits high metabolic stability with phase I half-life of 93mins and phase II of 60 mins. In contrast, the inactive version methoxyl-protected version of alpha-phenyl (Fig 3.) showed significantly faster metabolism with phase I half-life at 13 mins. Detailed metabolite identification is needed to thoroughly understand the metabolism of these tropolone analogues.

8.3.2 Solution solubility determination of alpha-naphthyl tropolone

With the evolution of tropolone analogues, a newer lead compound alpha-naphthyl tropolone exhibited promising cytotoxicity against various malignant cell lines. To assess the drug likeliness of these compounds and prepare for *in vivo* efficacy testing, kinetic solubility of the alpha-naphthyl tropolone was evaluated in water, RPMI medium and phosphate buffered saline (PBS). The calculated logD value at pH7.4 was 3.16 (Fig 4., estimated by software ChemAxon). The experimental solubility was determined as 240 µM in PBS and water, while significantly lower at 80 µM in RPMI medium. The solubility discrepancy was hypothesized to be due to ion strength or composition difference in buffer; however, thorough evaluation will be performed in the future. Lead compounds with better solubility are under preparation.

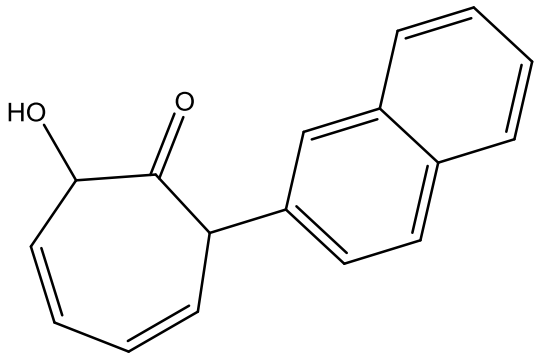

Naphthyl tropolone
$logD_{7.4}$=3.16

Figure 4. Structure and calculated logD value of alpha-naphthyl tropolone

8.4. Conclusions

A small library of tropolone based analogues was developed. These tropolone compounds exhibit promising HDAC inhibition and cytotoxicity to T-lymphocyte cancer cell lines. Initial ADME evaluation also suggested lead compound alpha-phenyl tropolone was more metabolically stable than the FDA approved hydroxamate containing HDAC inhibitor vorinostat. A detailed mechanic study revealed an anti-proliferative manner distinct from vorinostat [8]. Newer tropolone-based compounds with potent inhibition of the growth of hematological cell lines and better drug likeliness are under development.

8.5. Acknowledgements

I gratefully thank Dr. Sophia Ononye for all the biological testing of the tropolone analogues. Special thanks to Dr. Zack Oblak, Mike Van Heyst and Eric Falcone for compounds synthesis.

8.5. References

1. Gripenberg, J. and A.B. Anderson, *Antibiotic substances from the heart wood of Thuja plicata D.Don; the constitution of beta-thujaplicin.* Acta Chem Scand, 1948.
2. Arima, Y., et al., *Antibacterial effect of beta-thujaplicin on staphylococci isolated from atopic dermatitis: relationship between changes in the number of viable bacterial cells and clinical improvement in an eczematous lesion of atopic dermatitis.* J Antimicrob Chemother, 2003. **51**(1): p. 113-22.
3. Krenn, B.M., et al., *Antiviral activity of the zinc ionophores pyrithione and hinokitiol against picornavirus infections.* J Virol, 2009. **83**(1): p. 58-64.
4. Liu, S. and H. Yamauchi, *Hinokitiol, a metal chelator derived from natural plants, suppresses cell growth and disrupts androgen receptor signaling in prostate carcinoma cell lines.* Biochem Biophys Res Commun, 2006. **351**(1): p. 26-32.

5. Yamato, M., et al., *Synthesis and antitumor activity of tropolone derivatives. 7. Bistropolones containing connecting methylene chains.* J Med Chem, 1992. **35**(2): p. 267-73.
6. Oblak, E.Z., et al., *The furan route to tropolones: probing the antiproliferative effects of beta-thujaplicin analogs.* Org Biomol Chem, 2012. **10**(43): p. 8597-604.
7. Ononye, S.N., et al., *Tropolones as Lead-Like Natural Products: The Development of Potent and Selective Histone Deacetylase Inhibitors.* ACS Medicinal Chemistry Letters, 2013.
8. Ononye, S.N., et al., *Studies on the antiproliferative effects of tropolone derivatives in Jurkat T-lymphocyte cells.* Bioorg Med Chem, 2014. **22**(7): p. 2188-93.
9. Minucci, S. and P.G. Pelicci, *Histone deacetylase inhibitors and the promise of epigenetic (and more) treatments for cancer.* Nat Rev Cancer, 2006. **6**(1): p. 38-51.
10. Minucci, S., et al., *Histone deacetylases: a common molecular target for differentiation treatment of acute myeloid leukemias?* Oncogene, 2001. **20**(24): p. 3110-5.
11. Duvic, M., et al., *Phase 2 trial of oral vorinostat (suberoylanilide hydroxamic acid, SAHA) for refractory cutaneous T-cell lymphoma (CTCL).* Blood, 2007. **109**(1): p. 31-9.

Chapter 9

Summary and future directions

9.1. Summary of work

Dihydrofolate reductase (DHFR) is a key enzyme in the folate biosynthetic pathway and has been a popular drug target for over sixty years [1-3]. TMP is the sole FDA approved antibacterial DHFR inhibitor and remains clinicalally important [4-5]. However, acquired resistance by point mutations and natural enzymatic insensitivity limit its use [6-9].

During the past several years, a novel class of propargyl-linked DHFR inhibitors targeting MRSA, *Candida* and *Klebsiella* species was developed under the robust collaboration between Drs. Amy Anderson and Dennis Wright [10-13]. Early lead compounds in this library exhibit potent enzyme inhibition and promising antibacterial and antifungal activities [14-15]. Initial ADME assessment suggested some compounds were poorly water soluble and metabolically instable [16]. To improve the drug likeliness while maintaining high antimicrobial potency, a strategy of incorporating crystallographic insight and experimental evaluation of SAR to guide new compound generation was explored.

UCP111D, a lead compound within the biphenyl series, exhibited potent inhibition of *S. aureus* DHFR (IC_{50}=61 nM) and promising antibacterial activity (MIC=0.72 μg/mL) [14]. However, low water solubility (20 μg/mL) and precipitation in DMSO stock was also observed. Much effort was taken to improve the water solubility by introducing more

polar functional groups. UCP1006, featuring a pyridine substitution at the distal biaryl system, was synthesized and showed improved solubility (40 μg/mL) and striking antibacterial activity (MIC=0.08 μg/mL). A study of the metabolic stability of UCP1006 and its derivatives suggested a relatively short half-life with MLM. SPR analysis also indicated that the metabolic stability of these analogues was sensitive to substitutions at the propargylic and adjacent aryl methoxy positions. UCP1040, featuring a propargyl methyl and 2' methoxy group on the adjacent phenyl ring, showed increased metabolic half-life of 65mins at high substrate testing concentration.

To thoroughly investigate the DMPK properties of lead propargyl-linked compounds, multiple *in vitro* and *in vivo* assays were performed. Some early pyridine containing compounds were found to be strong CYP3A4 and CYP2D6 inhibitors. It was also hypothesized the prolonged *in vitro* microsomal half-life detected at the high substrate concentration were artificial effects from inhibition of CYP isoforms responsible for its own metabolism. Metabolic stability evaluation using lower substrate concentration (0.5 μg/mL) resulted in dramatically shorter half-lives.

To further improve metabolic stability while reducing the propensity for CYP inhibition, two approaches were implemented: one, blocking the metabolic "soft-spots" and preventing metabolite formation; two, decreasing the hydrophobicity of the compounds, thereby reducing CYP binding. Dimethyl pyridine substituted UCP1076 effectively diminished the primary metabolism route of pyridine-*N*-oxidation. In addition, the protected pyridine group also sharply decreased CYP3A4 inhibition by 80 folds.

However, the metabolic half-life of UCP1076 remained short (8 mins). A metabolite identification study suggested the only major metabolic route for UCP1076 was demethylation on the 2' methoxy group on the adjacent phenyl ring. Several attempts were made to improve microsomal stability by introducing a deuterium substituted methoxy group, dimethoxy, dioxolane or dioxane on the adjacent phenyl ring. However, little effect was observed. UCP1115, featuring an open phenyl on the adjacent position and a distal dimethyl pyridine, exhibited marginal improvement with a half-life of 20 minutes with MLM. Detailed metabolite identification and optimization of UCP1115 was under investigation.

UCP1106, a zwitterion compound featuring a carboxyl phenyl on the distal position with a propargylic hydrogen and 2' methoxy on the adjacent phenyl ring, was designed to improve metabolic stability with lower hydrophobicity. UCP1106 exhibited excellent ADME properties with $t_{1/2}$=99 mins against MLM and low inhibition for CYP3A4 and CYP2D6 (IC_{50} greater than 50 μM). Furthermore, UCP1106 was also proven to be a potent *S. aureus* inhibitor (MIC=0.02 μg/mL). More recent results also suggested that UCP1106 has low toxicity to mammalian cell lines. As the best lead compound so far, the *in vivo* PK properties and efficacy will be evaluated.

9.2. Future plans

9.2.1 Lead optimization of dimethyl pyridine series

Lead propargyl-linked antifolates featuring a distal dimethyl pyridine functional group (UCP1076, UCP1111, and UCP1115 etc.) are potent antibacterial agents. The

microsomal stability of these compounds is general low ($t_{1/2}$ between 8 to 20 mins), and initial metabolite identification assessment suggested the primary metabolic route was demethylation or hydroxylation on the adjacent phenyl ring (data not shown). Several new compounds are designed aiming to increase the *in vitro* metabolic half-life while maintaining high antibacterial and low CYP inhibition activity.

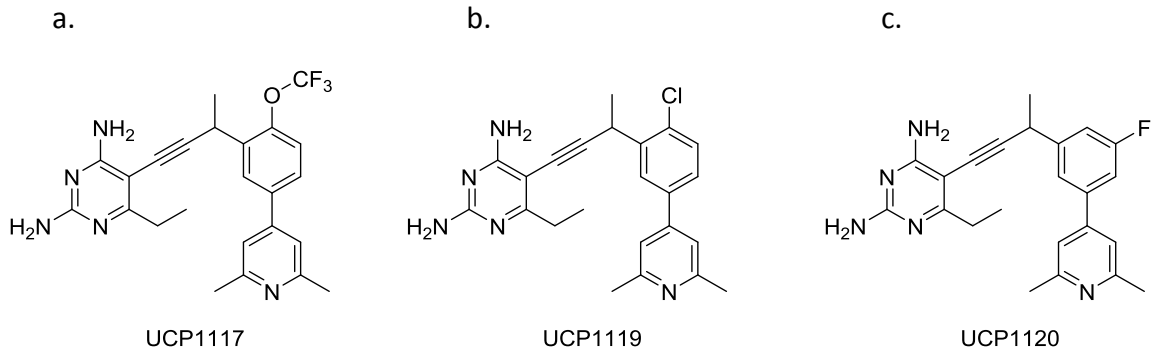

Figure 1. Structures of proposed dimethy pyridine compounds

UCP1117 (Fig 1a.), featuring a 2' trifluoromethoxy group on the adjacent phenyl, is proposed with similar DHFR inhibitory activity and low CYP inhibition as its trideuteromethoxy analogue (UCP1111). In addition, it is also generally believed that the fluorine substitution will also effectively diminish the demethylation route from cytochrome P450s [17-18]. With the only major metabolism route blocked, a significantly longer metabolic half-life is expected for UCP1117.

UCP1119 (Fig 1b) and UCP1120 (Fig 1c), featuring 2' chlorine and 3' fluorine on the adjacent phenyl ring, respectively, are also hypothesized to be potent antibacterial agents with promising ADME properties. With the major metabolite of UCP1115 tentatively assigned as hydroxylation on the adjacent phenyl ring, the blocking group

from the two new compounds should efficiently reduce the metabolism [19-21]. The electron withdrawing propensity of the halogen atoms may also contribute to decrease the strong CYP3A4 inhibition liability observed in UCP1115 (IC_{50}=0.5 μM).

These three compounds are all racemic mixtures with a chiral center at the propargylic position. Previous results suggested that the stereo chemical configuration at the position is important to both antibacterial potency and metabolic fate. Therefore, generation of the single enantiomers would be useful. It would be interesting to experimentally evaluate the *in vitro* ADME properties of these proposed compounds. With the expected improvement in microsomal stability, the *in vivo* drug exposure and residence time would also increase. Establishment of the *in vitro* and *in vivo* correlation of ADME properties would help better rank order compounds and selection for more comprehensive *in vivo* efficacy study using infected animal models.

9.2.2 Lead optimization of dioxolane series

Lead compounds featuring benzyl dioxolane at the adjacent biaryl system (UCP1038, UCP1070, and UCP1112 etc) are excellent antibacterial agents. UCP1070 and UCP1112 both highlight a deuterated dioxolane methylene group. Despite the protection of mechanism based inaction of CYPs, the two compounds remained strong CYP3A4 inhibitors and the metabolic half-life of the compounds in the dioxolane series is still short. Metabolite identification results indicated that the major metabolic route was hydroxylation on the dioxolane ring, subsequently generating dihydroxy phenyl metabolites. It is hypothesized that a fluorine substituted dioxolane (Fig 2a) on the

methylene group would completely block this reaction. It would be also valuable to understand if the fluorine substitution would also reduce the CYP3A4 inhibition.

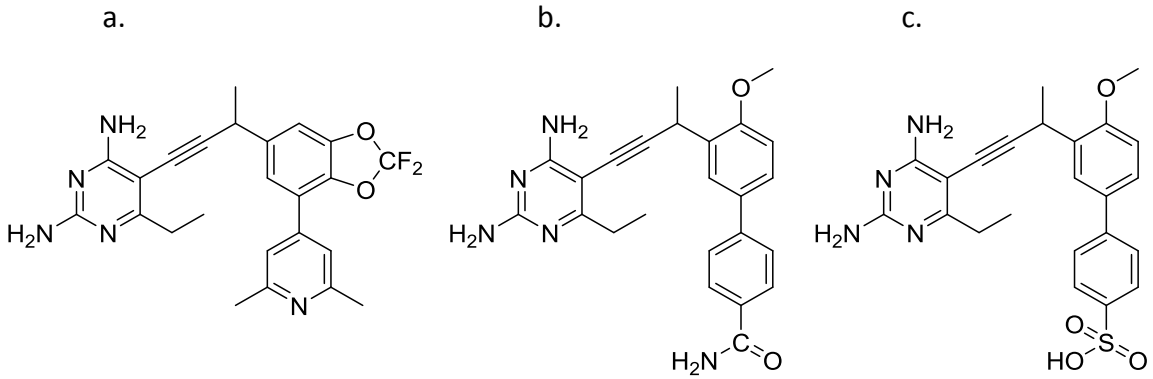

Figure 2. Structures of proposed dioxolane and zwitterions compounds

9.2.3 Lead optimization of zwitterion compounds series

UCP1106, a zwitterion compound featuring a distal benzoic acid on the biaryl system, exhibited superb antibacterial activity. *In vitro* ADME assessment also revealed superior metabolic stability, water solubility and low CYP inhibition. Initial assessment also suggested moderate toxicity to mammalian cell lines. Collectively, UCP1106 was the best compound in the library of propargyl-linked antifolate. *In vivo* PK and efficacy of UCP1106 will be thoroughly investigated. If an unexpected ADME liability was observed *in vivo*, possible derivatives of UCP1106 like benzamide (Fig 2b) or sulfonic acid (Fig2c) would be suitable alternatives. Previously described compounds in the para series were more active against *Candida glabrata* and *Candida albicans*[13], it is also advised to evaluated para-substituted versions of UCP1106 analogues for antifungal activities.

9.2.4 *In vivo* efficacy evaluation strategy

Through collaboration with Dr. Wielderhold's group in UTHSCSA, the *in vivo* antibacterial activity of UCP1006 was evaluated using a well characterized mice MRSA bacteremia model [22-23]. Although the compound did not effectively clear the bacterial infection, lessons were learned to better support the development of the antifolates.

With the improvement of *in vitro* metabolic stability and decrease in CYP inhibition, better *in vivo* drug exposure and less CYP induction are expected for newer lead compounds (UCP1106, UCP1117 etc.). More excitingly, the new compounds also exhibited better antibacterial potency and lower mammalian cell toxicity. Therefore, a possibly higher dosage would be tolerated and a higher drug concentration would be expected in targeted tissues. While the high thymidine level in murine plasma would be expected to bypass the DHFR inhibition and compromise the antibacterial activity of antifolates [24-25], a side-by-side *in vivo* efficacy study using a thymidine kinase (TK) knockout MRSA strain would be helpful to prove potency. In addition, to assess future efficacy for pathogens without TK knockout strains (*Candida* or *klebsiella* spp), a possible alternative strategy is to pre-treat animals with pegylated thymidine phosphorylase, which would reduce the circulating thymidine level to that similar to human during the treatment period [24].

9.3. Final acknowledgements

First, I must thank my advisor Dr. Amy Anderson for her guidance in research and also in life. I would like to thank Dr. Dennis Wright and Dr. Jose Manautou for their helpful advice and comments during my graduate career. I would like to acknowledge past and present members of the Anderson laboratory: Dr. Kathleen Frey for antibacterial activity determination, Dr. Jennifer Beierlein for compounds synthesis, Dr. Janet Paulsen for antifungal acitivity testing, Dr. Sophia Ononye for HDAC activity evaluation, Stephanie Reeve for antibacterial testing, Dr. Micheal Lombardo for antifungal evaluation and *in vitro* metabolism assays. I would also like to acknowledge past and present members in the Wight laboratory: Dr. Kishore Viswanathan, Dr. Santosh Keshipeddy, Narendran Dayanan and Eric Scocchera for compound synthesis.

9.4. References

1. Wilson, T. and J.F. Edeson, *Treatment of acute malaria with pyrimethamine.* Br Med J, 1953. **1**(4804): p. 253-5.
2. Bertino, J.R., *The Mechanism of Action of the Folate Antagonists in Man.* Cancer Res, 1963. **23**: p. 1286-306.
3. Gruneberg, R.N. and R. Kolbe, *Trimethoprim in the treatment of urinary infections in hospital.* Br Med J, 1969. **1**(5643): p. 545-7.
4. Reeves, D.S., et al., *Trimethoprim--sulphamethoxazole: comparative study in urinary infection in hospital.* Br Med J, 1969. **1**(5643): p. 541-4.
5. Warren, J.W., et al., *Guidelines for antimicrobial treatment of uncomplicated acute bacterial cystitis and acute pyelonephritis in women. Infectious Diseases Society of America (IDSA).* Clin Infect Dis, 1999. **29**(4): p. 745-58.
6. Dale, G.E., et al., *A single amino acid substitution in Staphylococcus aureus dihydrofolate reductase determines trimethoprim resistance.* J Mol Biol, 1997. **266**(1): p. 23-30.
7. Young, H.K., R.A. Skurray, and S.G. Amyes, *Plasmid-mediated trimethoprim-resistance in Staphylococcus aureus. Characterization of the first gram-positive plasmid dihydrofolate reductase (type S1).* Biochem J, 1987. **243**(1): p. 309-12.
8. Lyon, B.R., J.W. May, and R.A. Skurray, *Tn4001: a gentamicin and kanamycin resistance transposon in Staphylococcus aureus.* Mol Gen Genet, 1984. **193**(3): p. 554-6.
9. Zhou, W., et al., *Antifolates as effective antimicrobial agents: new generations of trimethoprim analogs.* MedChemComm, 2013.
10. Frey, K.M., et al., *Crystal structures of wild-type and mutant methicillin-resistant Staphylococcus aureus dihydrofolate reductase reveal an alternate conformation of*

NADPH that may be linked to trimethoprim resistance. J Mol Biol, 2009. **387**(5): p. 1298-308.
11. Liu, J., et al., *Towards new antifolates targeting eukaryotic opportunistic infections.* Eukaryot Cell, 2009. **8**(4): p. 483-6.
12. Paulsen, J.L., et al., *In vitro biological activity and structural analysis of 2,4-diamino-5-(2'-arylpropargyl)pyrimidine inhibitors of Candida albicans.* Bioorg Med Chem, 2009. **17**(14): p. 4866-72.
13. N, G.D., et al., *Propargyl-Linked Antifolates are Dual Inhibitors of Candida albicans and Candida glabrata.* J Med Chem, 2014. **57**(6): p. 2643-56.
14. Viswanathan, K., et al., *Toward new therapeutics for skin and soft tissue infections: propargyl-linked antifolates are potent inhibitors of MRSA and Streptococcus pyogenes.* PLoS One, 2012. **7**(2): p. e29434.
15. Paulsen, J.L., et al., *Structural analysis of the active sites of dihydrofolate reductase from two species of Candida uncovers ligand-induced conformational changes shared among species.* Bioorg Med Chem Lett, 2013. **23**(5): p. 1279-84.
16. Zhou, W., et al., *Acetylenic linkers in lead compounds: a study of the stability of the propargyl-linked antifolates.* Drug Metab Dispos, 2012. **40**(10): p. 2002-8.
17. Diana, G.D., et al., *Picornavirus inhibitors: trifluoromethyl substitution provides a global protective effect against hepatic metabolism.* J Med Chem, 1995. **38**(8): p. 1355-71.
18. Liu, Q., et al., *Discovery of 9-(6-aminopyridin-3-yl)-1-(3-(trifluoromethyl)phenyl)benzo[h][1,6]naphthyridin-2(1H)-one (Torin2) as a potent, selective, and orally available mammalian target of rapamycin (mTOR) inhibitor for treatment of cancer.* J Med Chem, 2011. **54**(5): p. 1473-80.
19. Tandon, M., et al., *The design and preparation of metabolically protected new arylpiperazine 5-HT1A ligands.* Bioorg Med Chem Lett, 2004. **14**(7): p. 1709-12.
20. Hester, J.B., et al., *Progress toward the development of a safe and effective agent for treating reentrant cardiac arrhythmias: synthesis and evaluation of ibutilide analogues with enhanced metabolic stability and diminished proarrhythmic potential.* J Med Chem, 2001. **44**(7): p. 1099-115.
21. Hutchinson, I., et al., *Antitumor benzothiazoles. 16. Synthesis and pharmaceutical properties of antitumor 2-(4-aminophenyl)benzothiazole amino acid prodrugs.* J Med Chem, 2002. **45**(3): p. 744-7.
22. Spellberg, B., et al., *The antifungal vaccine derived from the recombinant N terminus of Als3p protects mice against the bacterium Staphylococcus aureus.* Infect Immun, 2008. **76**(10): p. 4574-80.
23. Reyes, N., et al., *Efficacy of telavancin in a murine model of bacteraemia induced by methicillin-resistant Staphylococcus aureus.* J Antimicrob Chemother, 2006. **58**(2): p. 462-5.
24. Jackman, A.L., *Antifolate Drugs in Cancer Therapy*. 1999: Humana Press.
25. Jackman, A.L., et al., *Modulation of anti-metabolite effects. Effects of thymidine on the efficacy of the quinazoline-based thymidylate synthetase inhibitor, CB3717.* Biochem Pharmacol, 1984. **33**(20): p. 3269-75.

Chapter 10

Materials and methods

10.1. Metabolic stability determination [1]

10.1.1 High-performance liquid chromatography analysis

A Shimadzu Prominence 20 high-performance liquid chromatography (HPLC) instrument (Shimadzu, Kyoto, Japan) fitted with a Luna 5 µm C18 (2) 100 Å column (5 µM, 4.6 X 250 mm; Phenomenex, Torrance, CA) and a UV diode array detection at 254 nm was used to quantify compounds at 1µg/mL or above. The mobile phase consisted of 50% acetonitrile (ACN) and 50% potassium phosphate buffer (50 mM, pH 7.0), using an isocratic flow rate of 1.5 mL/min.

10.1.2 Metabolic half-life determination at high substrate concentration

Compounds were incubated with mouse liver microsomes or human liver microsomes (MLM or HLM; BD Biosciences, San Jose, CA) in 0.1 M potassium phosphate buffer (pH 7.4) and 200 µg/ml HPMC A4M in the presence of an NADPH regenerating system at 37°C. The final concentrations of inhibitor, microsomes, NADPH+, glucose 6-phosphate, glucose-6-phosphate dehydrogenase, and $MgCl_2$ were 5 µg/mL, 0.5 mg/mL, 1.3 mM, 3.3 mM, 0.5 U/mL, and 3.3mM, respectively. DMSO and compounds without MLM were used as negative controls. The reactions were initiated by the addition of microsomes and quenched by the addition of an equal volume of ice-cold ACN after 60 or 120 min.

The samples were subjected to centrifugation at 15,000 rpm for 10 min. 100µL of the diluted sample was injected on to the HPLC reversed-phase column. The concentration of compounds before and after metabolic incubation was calculated by standard curves obtained with each compound. Standard curves were performed multiple times and showed intraday and interday CV of less than 5%. To compare the metabolic stability of different compounds, the percentage of the parent compound remaining after incubation as compared with the amount before incubation was calculated. The *in vitro* metabolic half-life was calculated using a single time point approach following first-order kinetics as described previously.

10.1.3 Metabolic half-life evaluation and LC-MS analysis

A Shimadzu UPLC system equipped with LC-30AD gradient pump, CTO-30A column oven, CBM-20A UFLC coordinator, Prominence DGU-20A5 degasser and SIL-20AC auto-sampler was used for separation. Mass spectrometry was performed on a Shimadzu LCMS2020 system equipped with both electrospray ionization (ESI) and atmospheric-pressure chemical ionization (APCI) source. LC separation was achieved with a Phenomenex Kinetex 1.7µm C18 100Å column. Mobile phase A, consisting of 0.01% heptafluorobutyric acid (HFBA) in water, and mobile phase B, consisting of 0.01% HFBA in ACN, were used for a binary gradient elution as follows: 5 to 95% B in 7mins, hold at 95% B for 2mins, 95 to 5% B in 1min and hold at 5% B for 2mins. Diltiazem (500ng/mL) was used as internal control (IC).

MS was performed in the positive ion mode with EPI and APCI duel ionization mode. The interface temperature was set at 350°C, DL temperature was 250°C, nebulizing gas flow 1.5l/min, heat block temperature 400°C and drying gas flow at 15l/min. The analytes and IC were monitored at both scan mode and selected ion monitoring (SIM) mode. The scan mode was set from 50 to 500 m/z with scan speed 15000 u/sec and event time at 0.05sec.

The incubation condition was the same as described above expect the compound concentration was 0.5µg/mL. The reaction was initiated by the addition of microsomes. 100µL samples were withdrawn from mixture at 0, 10, 20, 30, 40 and 60 minutes after the start of incubation and protein precipitation was achieved by adding 100µL of ice cold ACN. The samples were subjected to centrifugation at 15,000 rpm for 10 min. 3 to 5µL of the supernatant was injected on to the UPLC-MS. The detection limit was estimated as 10ng/mL. The *in vitro* metabolic half-life was calculated using a multiple time points approach following first-order kinetics.

10.2. Kinetic solubility assay

Compounds were initially dissolved as 20 or 40 mg/mL dimethyl sulfoxide (DMSO) solutions and diluted in filtered water in the presence of 200 µg/mL methylcellulose (METHOCEL A4M; Dow Corning, Midland, MI). All samples were centrifuged for 10 min at 15,000 rpm, incubated at room temperature for 30 min, and analyzed by reversed phase HPLC-UV. Solubility was determined as the maximal concentration for which absorption is linearly related to the log of the concentration [2].

10.3. Solution stability assay

Compounds at 5 μg/mL were incubated with water, simulated gastric fluid and simulated intestinal fluid at 37°C for 24 h. All solutions contained 200 μg/mL hydroxypropylmethylcellulose (HPMC) A4M. Samples were collected before and after incubation. Assays were terminated by adding an equal volume of ice-cold ACN and centrifuging at 15,000 rpm for 10 min. One hundred microliters of supernatant was injected on the reversed-phase column of the HPLC-UV; solution stability was calculated using a ratio of area under the curve (AUC) (after incubation)/AUC (before incubation) [3].

10.4. Membrane permeability evaluation

Membrane permeability of propargyl-linked antifolates was evaluated with a PAMPA assay using Centrifree^{TM} ultrafiltration devices from Millipore (Billerica, MA). 30, 000 MWCO regenerated cellulose was selected. Testing compounds at 200 μM in PBS (1 mL total volume) was added into the sample reservoir. The devices were then capped and centrifuged at 2, 000 g using a fixed-angle centrifuge rotor with 17 X 100 mm adapters for 15 min. The filtrate cups were then removed and the ultrfiltrates were quantified by UV plate reader at 254 nm.

10.5. Metabolite identification assay

To identify phase I metabolites, compounds at 2 or 10μg/mL were incubated with MLM or HLM in the setup similar as described above. To identify both phase I and phase II

metabolites, compounds (at 2 μg/mL) were incubated with mouse or human S9 fractions in a Tris-HCl (pH7.5) buffer and 200 μg/mL HPMC A4M in the presence of an NADPH regenerating system and a UGT reaction mix for 2 hours at 37°C. The final concentrations of inhibitor, microsomes, NADPH+, glucose 6-phosphate, glucose-6-phosphate dehydrogenase, $MgCl_2$, alamethicin, and UDPGA were 5 μg/mL, 0.5 mg/mL, 1.3 mM, 3.3 mM, 0.5 U/mL, 8mM, 25 μg/mL and 2mM, respectively. Negative controls included 1) using the same volume of DMSO or 2) quenching the reaction with ACN immediately after adding microsomes or S9 fractions. Both samples and negative controls were incubated for 2 h, and the reaction was terminated with an equal volume (or 2X volumes for S9 fractions) of ice-cold ACN. After removal of protein precipitates by centrifugation, supernatant phase was purified using Oasis hydrophilic-lipophilic balanced sample extraction cartridges (Waters, Milford, MA) following the manufacturer's protocol. Methanol (1 mL) was used to elute the sample, which was further diluted 2-fold with water above.

10.6. Liquid chromatography/tandem mass spectrometry analysis and metabolite identification

An Agilent 1100 HPLC system fitted with a Zorbax-C18 (3μm, 1.0X150 mm) (Agilent Technologies, Santa Clara, CA) was used for separation. Mobile phase A, consisting of 0.01% heptafluorobutyric acid in water, and mobile phase B, consisting of 0.01% heptafluorobutyric acid in ACN, were used for a linear gradient elution as follows: 0 to 100% B in 17 min and isocratic hold at 100% B for 5 min. The flow rate was 75 μL/min,

and the injection volume was 8 µl. Mass spectrometric detection was performed on a Micromass Q-Tof-2 mass spectrometer from Waters, equipped with an electrospray ionization source. The mass spectrometer was operated in the positive ionization mode and was calibrated with Glu1-fibrinopeptide B on each experiment day. Capillary voltage and cone voltage were set at 3000 and 20 V, respectively. Source and desolvation temperatures were 100 and 150°C.

Nitrogen was used as a desolvation gas at a flow rate of 450 mL/h. Full-scan time-of-flight spectra were first acquired for parent compounds and metabolites in the mass spectrometry mode. Subsequently, collision-induced dissociation (CID) fragmentation spectra were obtained on the isolated protonated molecular ion of parent and metabolites in the tandem mass spectrometry mode. Argon or nitrogen was used as the collision gas, and the collision energy was optimized for each compound in the range of 20 to 40 eV. Accurate mass was calculated using fragments of the coanalyzed calibration standard lisinopril as described previously [4]. The distribution of metabolites was calculated by dividing the AUC of the individual metabolite by the total AUC for all metabolites within the same injection.

To achieve multiple-stage mass spectrometry (MS^n), additional metabolite identification work was conducted at Proteomics center at Yale school of medicine (New Haven, CT) with the help of Dr. Tukiet Lam. Samples were anlyzed using an Acquity Ultra Performance LC system (Waters) fitted a Restek Ultra AQ C18 column (3 µm, 100 mm X 1.0 mm, particle size 3 µm) connected with a LTQ orbittrap XL mass spectrometer from

Thermo Scientific [5]. Resolution was set at 30,000. The collision energy was set at 35eV with helium as collision gas. Full scan range was set at 200~2000.

The LC condition of mobile phase A, consisting of 0.01% heptafluorobutyric acid in water, and mobile phase B, consisting of 0.01% heptafluorobutyric acid in ACN, were used for a linear gradient elution as follows: 0 to 100% B in 17 min and isocratic hold at 100% B for 5 min, additional 8 min was allowed to re-equilibrate column. The flow rate was 75µL/min, and the injection volume was 8 µL.

Metabolism samples were prepared in house as described earlier and shipped to Yale for analysis. Experimental results were then sent back for further data process using software Mass++ 64-bit version 2.7.2 (supported by Shimadzu Corporation and Eisai Co., Ltd).

10.7. CYP inhibition assay

CYP3A4 and CYP2D6 inhibition was evaluated using a commercial fluorescence based high-throughput screening assay from BD Gentest (Worcester, MA) [6-7]. For CYP3A4 and CYP2D6, substrates BQ and AMMC were used generating fluorescent metabolites HQ and AHMC, respectively. Compounds were tested in the range 0.008µM-50uM. Incubation was initiated by adding Supersome enzymes and terminated by adding stop solution after 30min incubation. The IC_{50} values were calculated following a first order kinetics.

10.8. Plasma drug quantification by UPLC-MS

All plasma samples from *in vivo* efficacy study were removed from -80°C and thawed at room temperature. A 100µL sample was removed from each tube and mixed with 200 µL ice cold ACN. The samples were thoroughly mixed and centrifuged at 15,000 rpm for 10mins. The supernatants were then collected and analyzed by UPLC-MS. Diltiazem was used as internal control. The instrument setup was the same as described in section 10.1.3. PK data was processed by WinNonlin (Pharsight Corporation) using a one compartmental IV-bolus model.

10.9. Metabolic stability assay for tropolone analogues[8]

The Incubation conditions for the tropolone compounds was the same as described in section 10.1.2 expect that the substrate concentration was 1µM. The UPLC-MS assay used to quantify tropolone compounds was performed using the same mass spectrometer setup as described in the previous section (10.1.3). The LC condition used for tropolone compounds specifically was mobile phase A, consisting of 0.01% acetylacetone (ACAC) and 0.1% TFA in water, and mobile phase B, consisting of 0.01% ACAC and 0.1% TFA in ACN, with a binary gradient elution as follows: 5 to 95% B in 7mins, hold at 95% B for 2mins, 95 to 5% B in 1min and hold at 5% B for 2mins. The *in vitro* metabolic half-life was calculated using a single time point approach following first-order kinetics as described previously [2]. The detection limit was estimated as 50ng/mL.

10.10. Solution kinetic solubility assay for tropolone analogues

Tropolone compounds were initially dissolved as 100mM in DMSO solutions and diluted in filtered water, RPMI medium and phosphate buffered saline (PBS). All samples were incubated at room temperature for 30 min, centrifuged for 10 min at 15,000 rpm, and analyzed by reversed phase HPLC as described in section 10.1. The mobile phase consisted of 80% ACN and 20% potassium phosphate buffer (50 mM, pH 2.0), with 0.05% ACAC using an isocratic flow rate of 1.5 mL/min. Solubility was determined as the maximal concentration for which absorption is linearly related to the log of the concentration.

10.11. References

1. Zhou, W., et al., *Acetylenic linkers in lead compounds: a study of the stability of the propargyl-linked antifolates.* Drug Metab Dispos, 2012. **40**(10): p. 2002-8.
2. Kerns, E.H. and D. Li, *Drug-like Properties: Concepts, Structure Design and Methods.* Academic Press;, 2008.
3. Di, L. and E.H. Kerns, *Solution stability--plasma, gastrointestinal, bioassay.* Curr Drug Metab, 2008. **9**(9): p. 860-8.
4. Hill, D.W., et al., *Mass spectral metabonomics beyond elemental formula: chemical database querying by matching experimental with computational fragmentation spectra.* Anal Chem, 2008. **80**(14): p. 5574-82.
5. Ma, X.M., et al., *Nonenzymatic domains of Kalirin7 contribute to spine morphogenesis through interactions with phosphoinositides and Abl.* Mol Biol Cell, 2014. **25**(9): p. 1458-71.
6. Yamamoto, T., A. Suzuki, and Y. Kohno, *High-throughput screening to estimate single or multiple enzymes involved in drug metabolism: microtitre plate assay using a combination of recombinant CYP2D6 and human liver microsomes.* Xenobiotica, 2003. **33**(8): p. 823-39.
7. Stresser, D.M., et al., *Substrate-dependent modulation of CYP3A4 catalytic activity: analysis of 27 test compounds with four fluorometric substrates.* Drug Metab Dispos, 2000. **28**(12): p. 1440-8.
8. Ononye, S.N., et al., *Tropolones as Lead-Like Natural Products: The Development of Potent and Selective Histone Deacetylase Inhibitors.* ACS Medicinal Chemistry Letters, 2013.

Appendix

Chapter 4.

a.

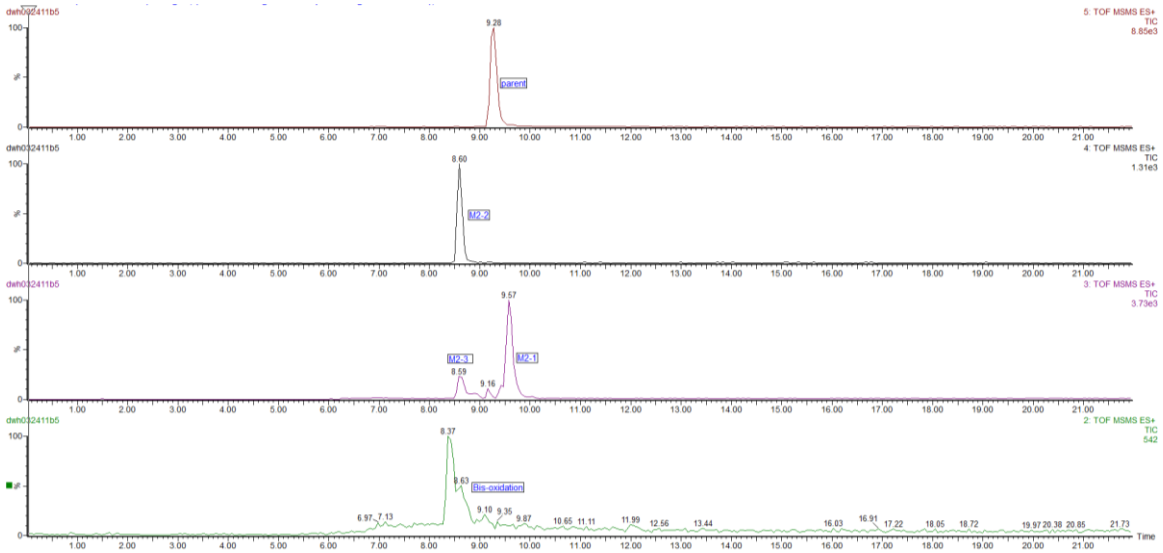

b.

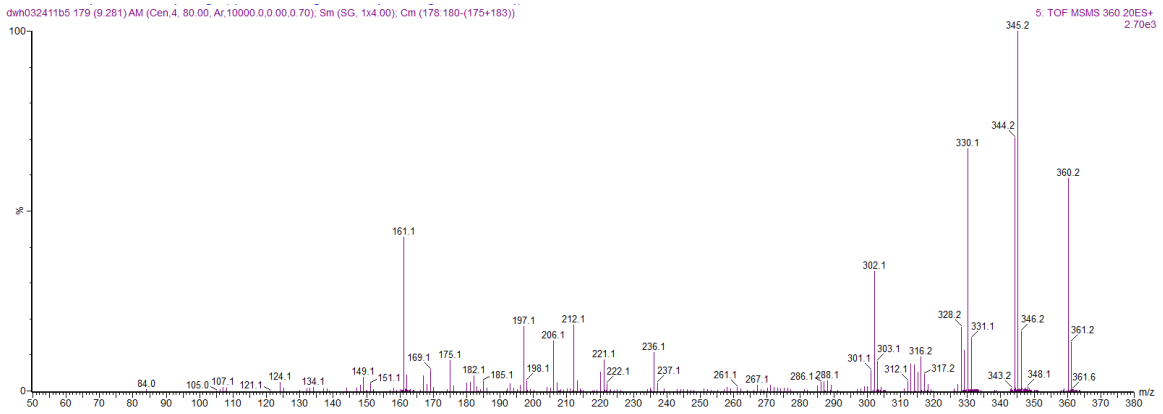

c.

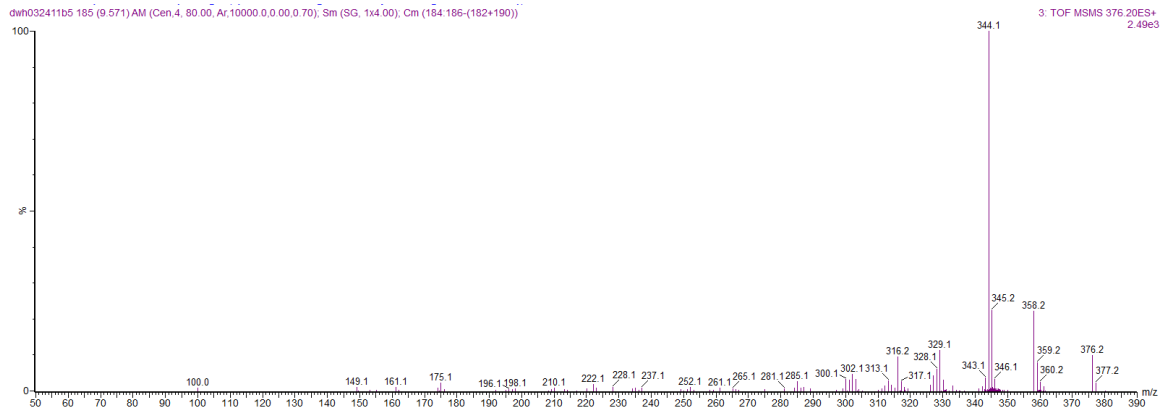

d.

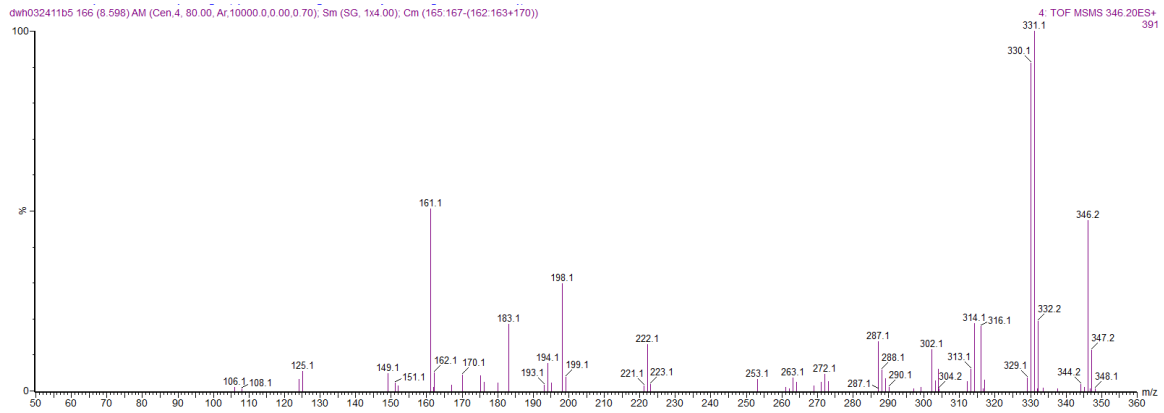

e.

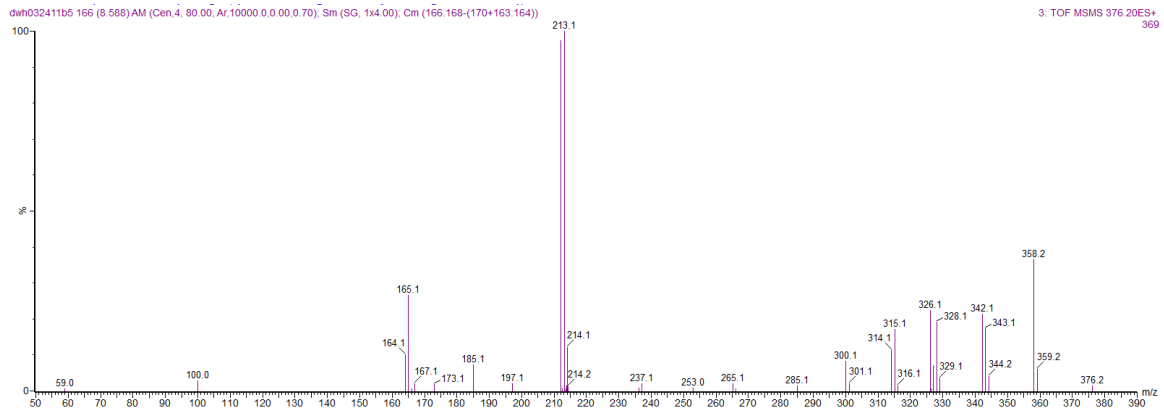

Figure 1. a, MS full scan of compound 2 (UCP1005) and metabolites; b, c, d, e, MS/MS spectrum of compound 2, M2-1, M2-2 and M2-3 (shown as Chapter 4, Fig 5.).

a.

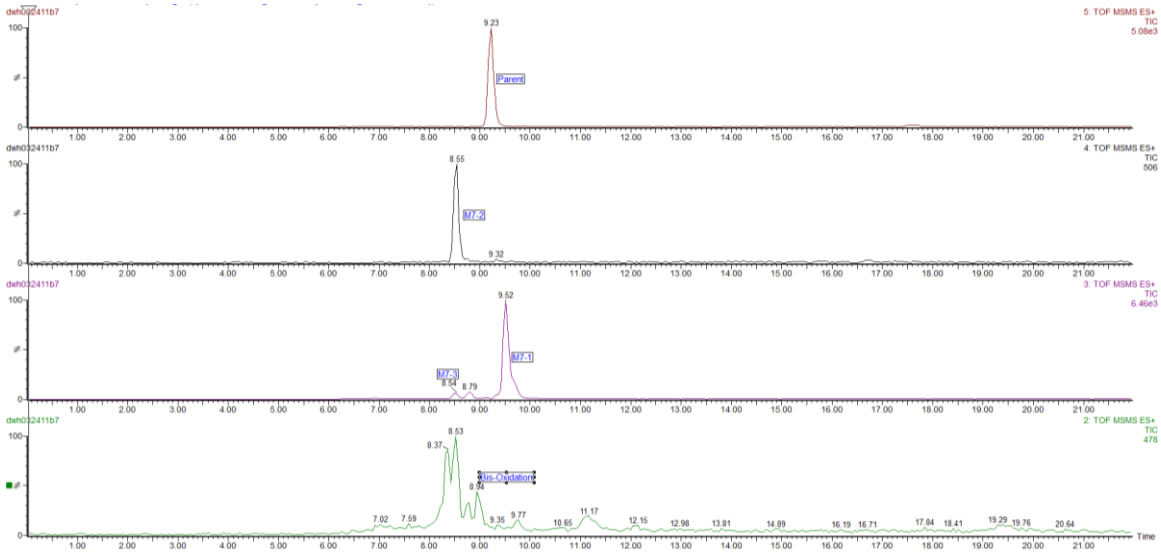
dwh032411b7
5: TOF MSMS ES+
TIC
5.08e3
9.23
Parent
4: TOF MSMS ES+
TIC
506
8.55
M7-2
9.32
3: TOF MSMS ES+
TIC
6.46e3
9.52
M7-1
M7-3
8.54
8.79
2: TOF MSMS ES+
TIC
478
8.63
8.37
M5-Oxidation
8.74
7.02
7.59
9.35
9.77
10.65
11.17
12.15
12.98
13.81
14.89
16.19
16.71
17.84
18.41
19.29
19.76
20.64
Time

b.

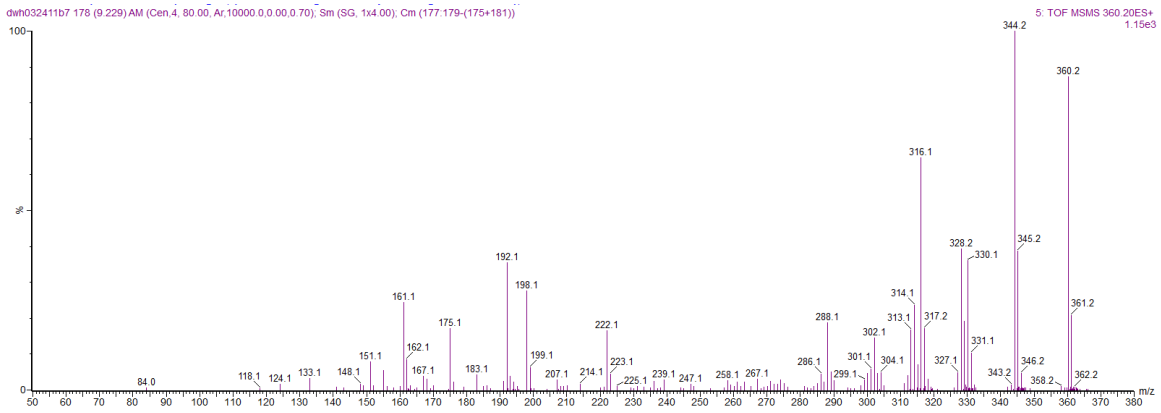
dwh032411b7 178 (9.229) AM (Cen,4, 80.00, Ar,10000.0,0.00,0.70); Sm (SG, 1x4.00); Cm (177:179-(175+181))
5: TOF MSMS 360.20ES+
1.15e3
344.2
360.2
316.1
328.2
345.2
330.1
192.1
198.1
314.1
361.2
161.1
313.1
317.2
288.1
175.1
222.1
302.1
331.1
162.1
151.1
199.1
327.1
346.2
167.1
183.1
223.1
84.0
343.2
362.2
m/z

c.

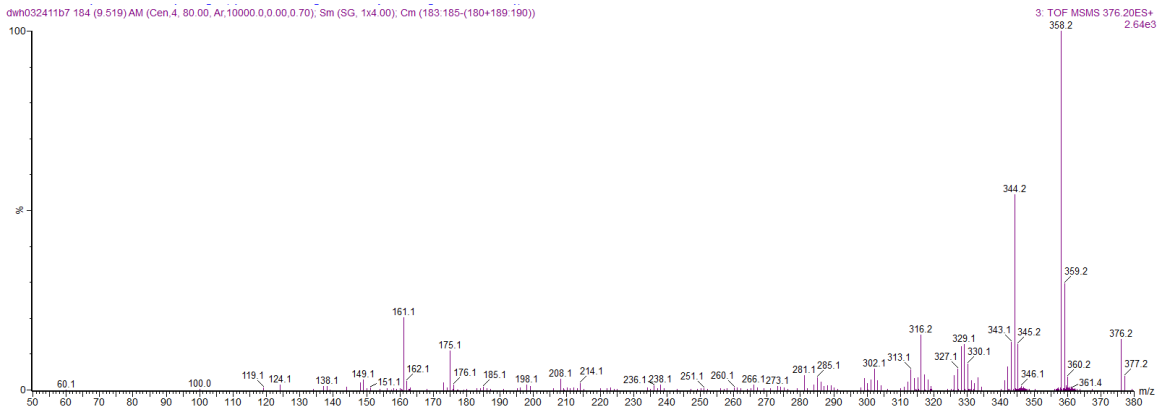
dwh032411b7 184 (9.519) AM (Cen,4, 80.00, Ar,10000.0,0.00,0.70); Sm (SG, 1x4.00); Cm (183:185-(180+189:190))
3: TOF MSMS 376.20ES+
2.64e3
358.2
344.2
359.2
161.1
316.2
175.1
343.1
345.2
376.2
329.1
327.1
330.1
162.1
377.2
176.1
360.2
60.1
100.0
346.1
361.4
m/z

d.

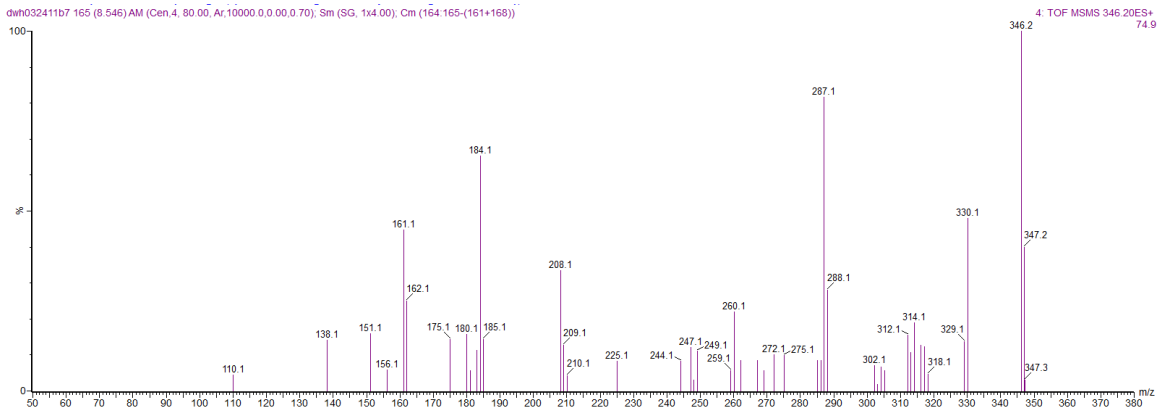

e.

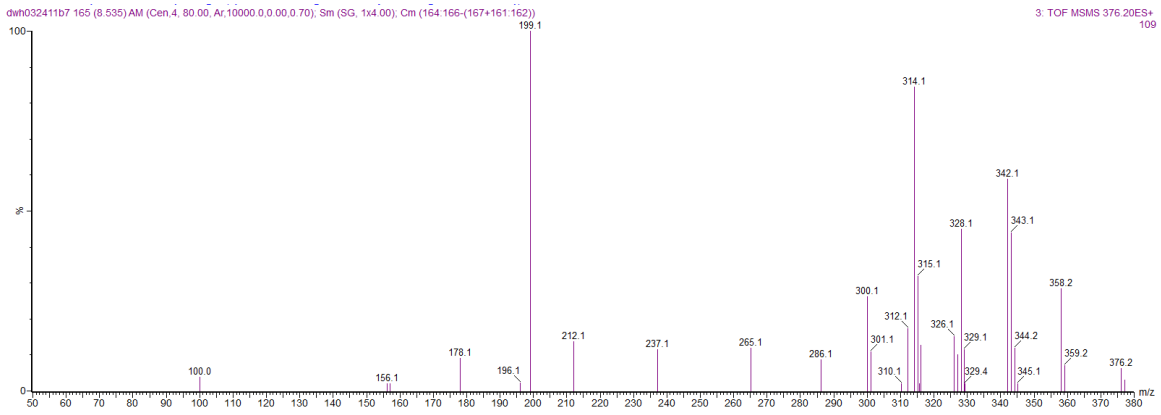

Figure 2. a, MS full scan of compound 7 (UCP1015) and metabolites; b, c, d, e, MS/MS spectrum of compound 7, M7-1, M7-2 and M7-3 (shown as Chapter 4, Fig 5.).

a.

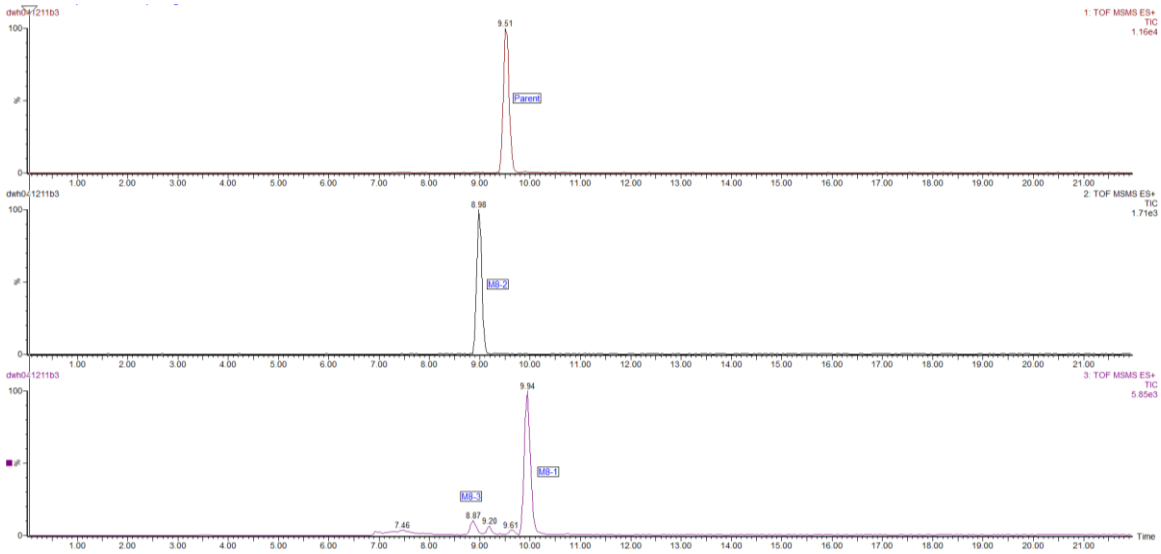
dwh041211b3
1: TOF MSMS ES+
TIC
1.16e4
9.51
Parent
dwh041211b3
2: TOF MSMS ES+
TIC
1.71e3
8.98
M8-2
dwh041211b3
3: TOF MSMS ES+
TIC
5.85e3
9.94
M8-1
M8-3
8.87
9.20
9.61
7.46
Time

b.

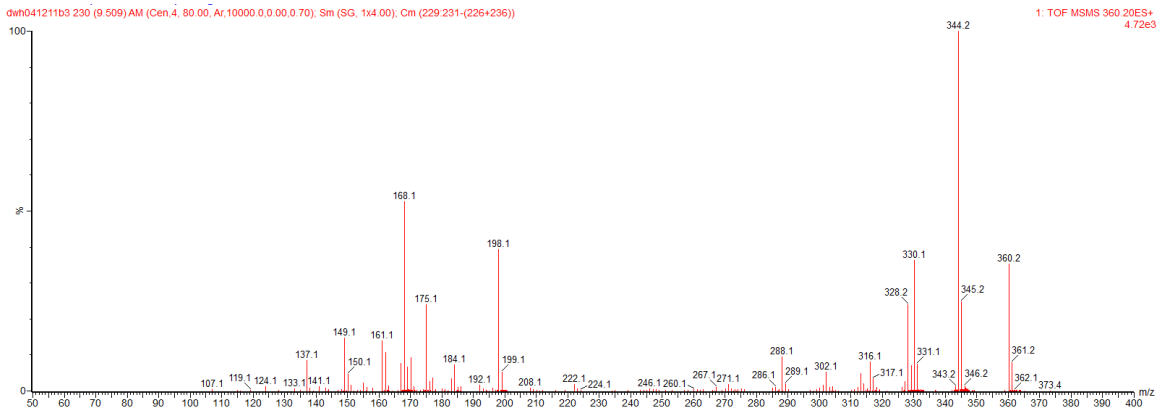
dwh041211b3 230 (9.509) AM (Cen,4, 80.00, Ar,10000.0,0.00,0.70); Sm (SG, 1x4.00); Cm (229:231-(226+236))
1: TOF MSMS 360.20ES+
4.72e3
344.2
168.1
198.1
330.1
360.2
175.1
328.2
345.2
149.1
161.1
137.1
150.1
184.1
199.1
331.1
361.2
288.1
316.1
302.1
289.1
317.1
343.2
346.2
362.1
373.4
m/z

c.

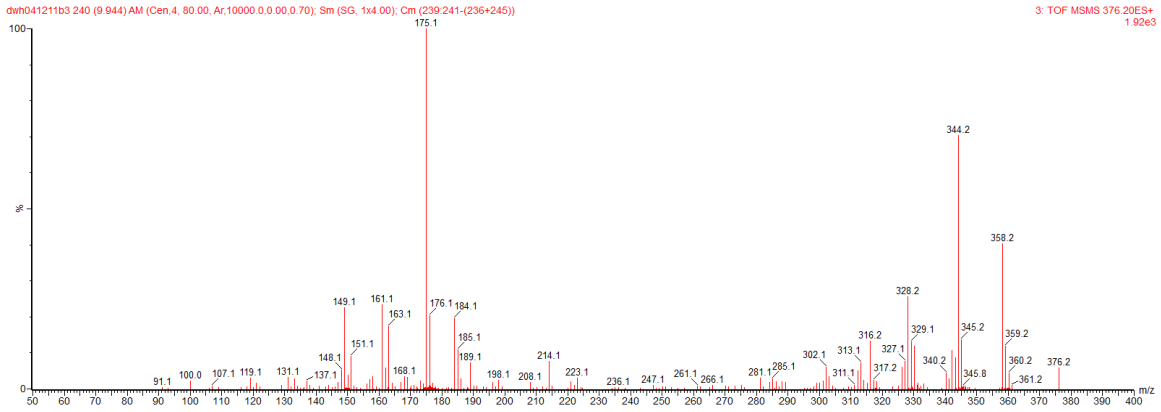
dwh041211b3 240 (9.944) AM (Cen,4, 80.00, Ar,10000.0,0.00,0.70); Sm (SG, 1x4.00); Cm (239:241-(236+245))
3: TOF MSMS 376.20ES+
1.92e3
175.1
344.2
358.2
328.2
149.1
161.1
176.1
184.1
163.1
329.1
345.2
316.2
359.2
185.1
151.1
327.1
340.2
360.2
376.2
189.1
214.1
302.1
313.1
317.2
345.8
361.2
m/z

d.

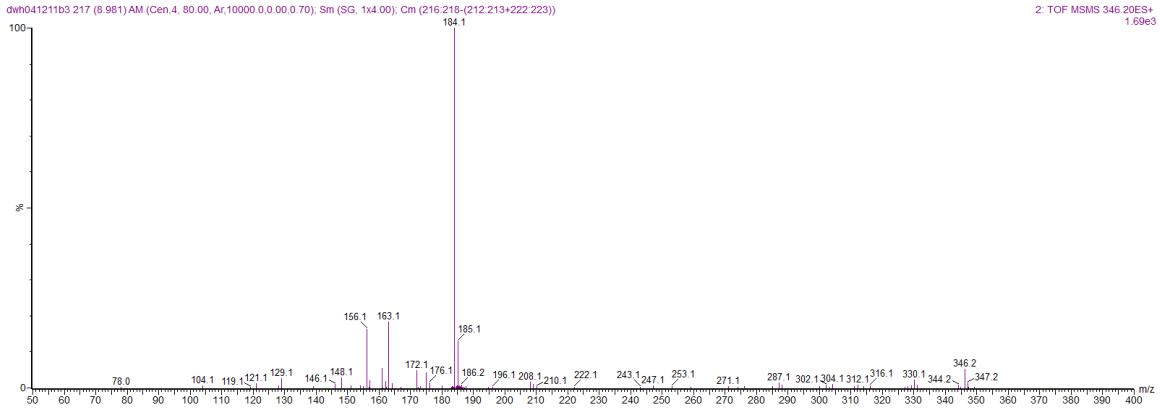

e.

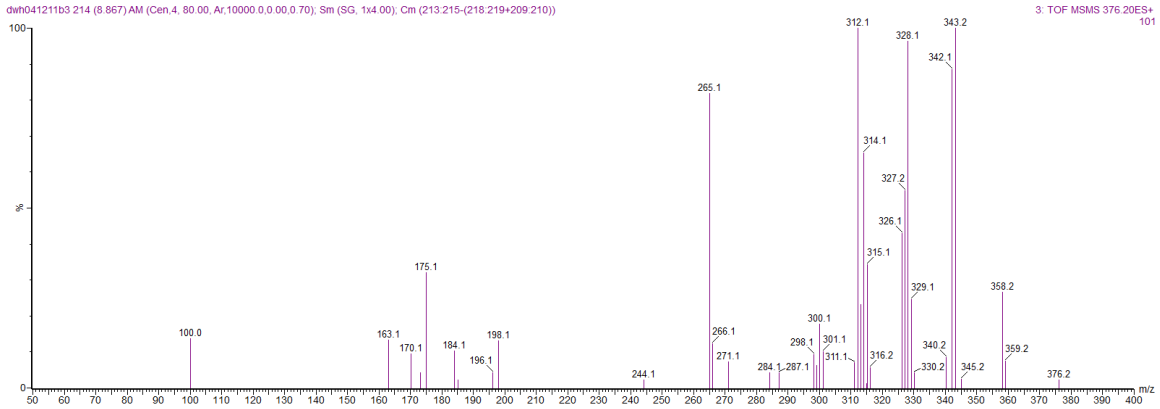

Figure 3. a, MS full scan of compound 8 (UCP1021) and metabolites; b, c, d, e, MS/MS spectrum of compound 8, M8-1, M8-2 and M8-3 (shown as Chapter 4, Fig 5.).

a.

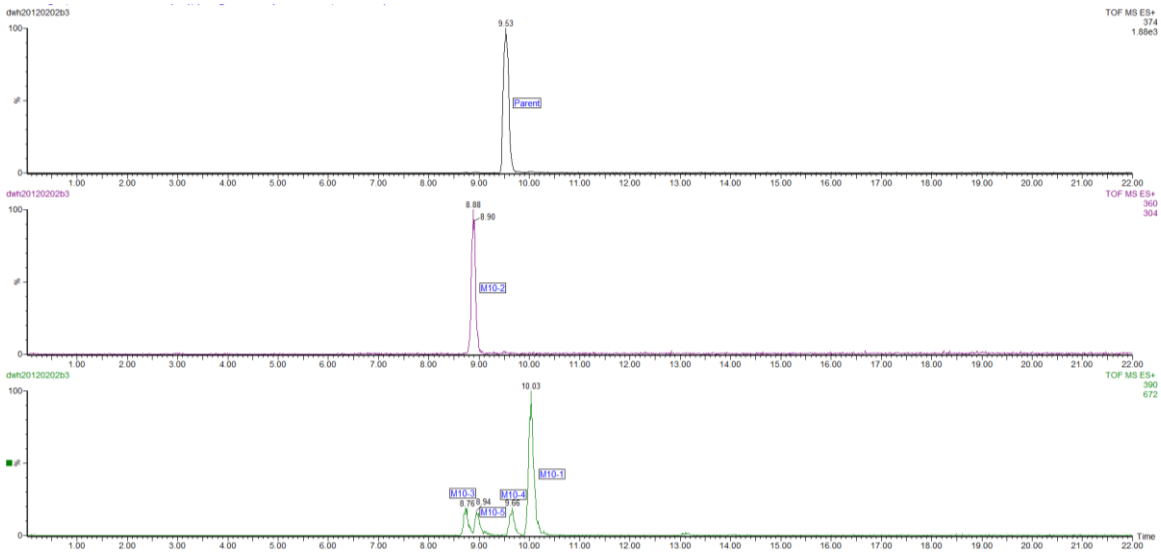
dwh20120202b3
TOF MS ES+
374
1.88e3
9.53
Parent
dwh20120202b3
TOF MS ES+
360
304
8.88
8.90
M10-2
dwh20120202b3
TOF MS ES+
390
672
10.03
M10-1
M10-3
8.76
8.94
M10-4
9.66
M10-5
Time

b.

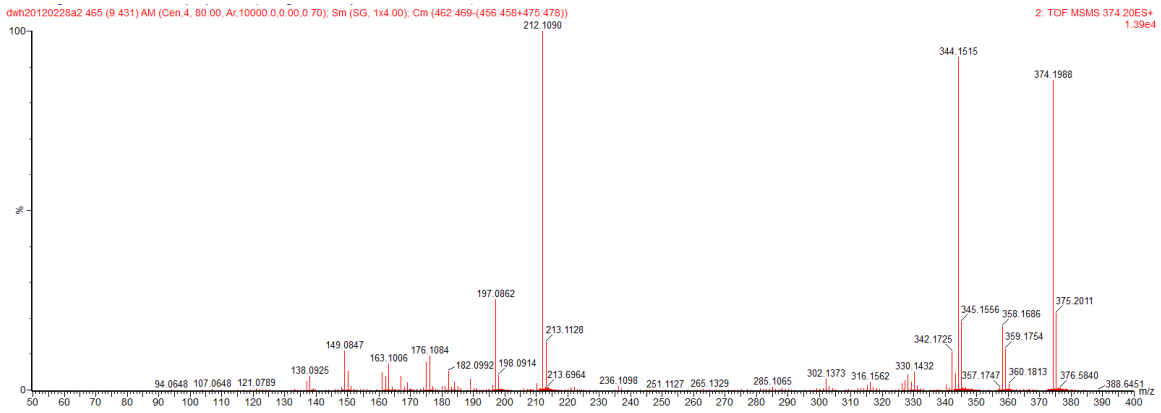
dwh20120228a2 465 (9.431) AM (Cen,4, 80.00, Ar,10000.0,0.00,0.70); Sm (SG, 1x4.00); Cm (462:469-(456:458+475:478))
2: TOF MSMS 374.20ES+
1.39e4
212.1090
344.1515
374.1988
197.0862
345.1556
358.1686
375.2011
213.1128
359.1754
342.1725
149.0847
176.1084
163.1006
138.0925
182.0992
198.0914
213.6964
330.1432
357.1747
360.1813
376.5840
388.6451
94.0648
107.0648
121.0789
236.1098
251.1127
265.1329
285.1065
302.1373
316.1562
m/z

c.

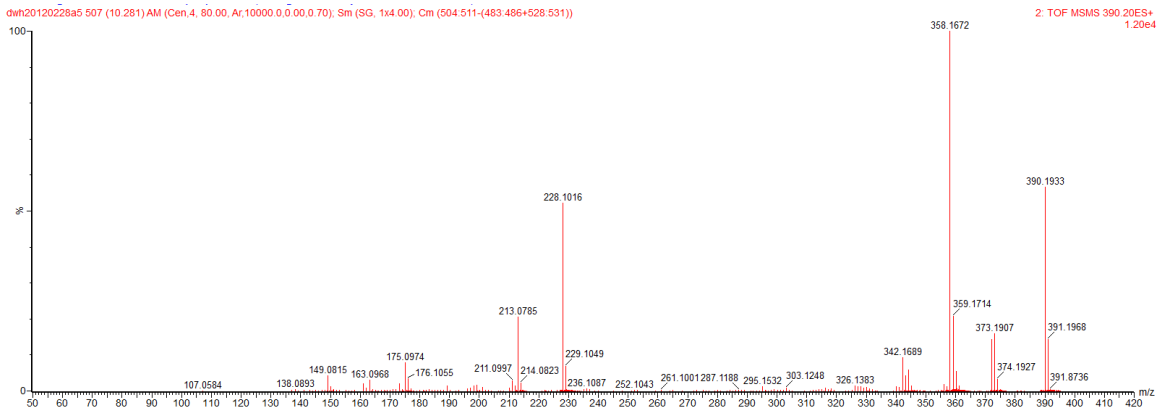
dwh20120228a5 507 (10.281) AM (Cen,4, 80.00, Ar,10000.0,0.00,0.70); Sm (SG, 1x4.00); Cm (504:511-(483.486+528:531))
2: TOF MSMS 390.20ES+
1.20e4
358.1672
390.1933
228.1016
359.1714
213.0785
373.1907
391.1968
229.1049
342.1689
175.0974
149.0815
163.0968
176.1055
211.0997
214.0823
374.1927
391.8736
107.0584
138.0893
236.1087
252.1043
261.1001
287.1188
295.1532
303.1248
326.1383
m/z

d.

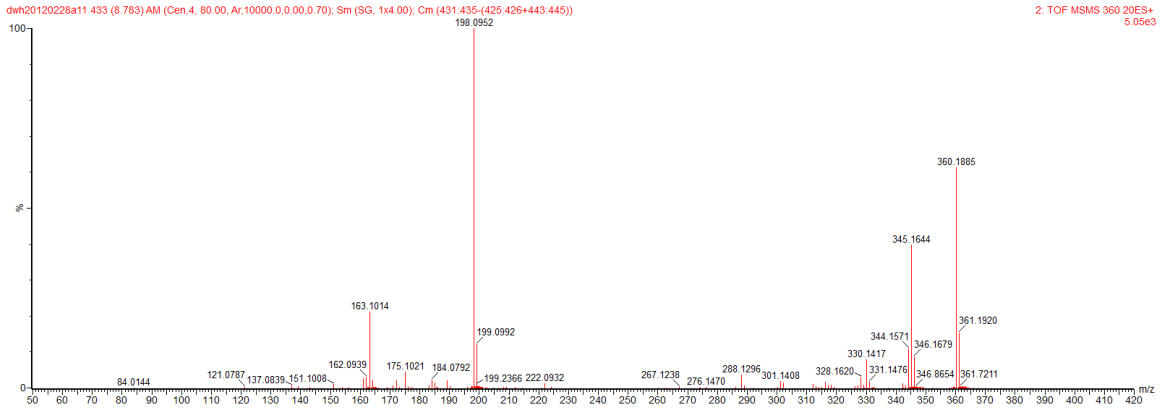
dwh20120228a11 433 (8.783) AM (Cen,4, 80.00, Ar,10000.0,0.00,0.70); Sm (SG, 1x4.00); Cm (431:435-(425:426+443:445))
2: TOF MSMS 360.20ES+
5.05e3
198.0952
360.1885
345.1644
163.1014
361.1920
199.0992
344.1571
346.1679
330.1417
162.0939
175.1021
184.0792
331.1476
121.0787
137.0839
151.1008
84.0144
199.2366
222.0932
267.1238
276.1470
288.1296
301.1408
328.1620
346.8654
361.7211
%
m/z

e.

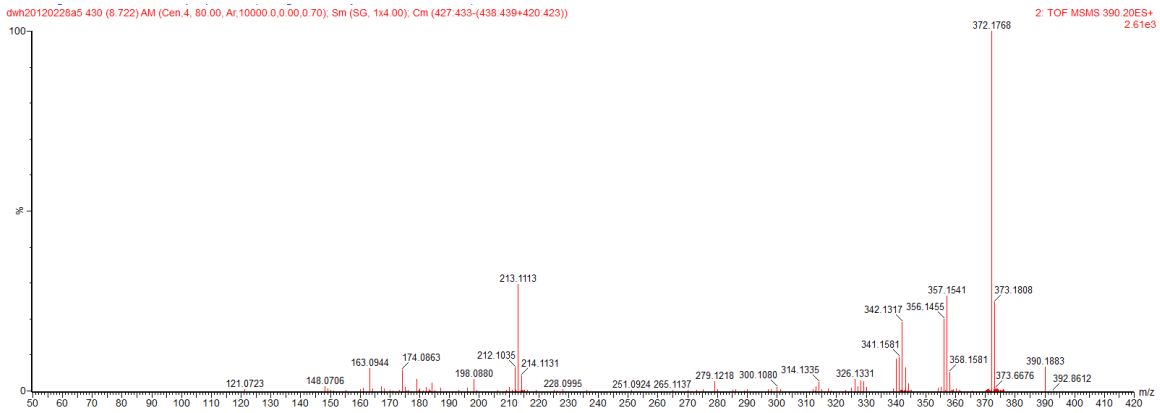
dwh20120228a5 430 (8.722) AM (Cen,4, 80.00, Ar,10000.0,0.00,0.70); Sm (SG, 1x4.00); Cm (427:433-(438:439+420:423))
2: TOF MSMS 390.20ES+
2.61e3
372.1768
213.1113
357.1541
373.1808
342.1317
356.1455
341.1581
358.1581
163.0944
174.0863
212.1035
214.1131
390.1883
121.0723
148.0706
198.0880
228.0995
251.0924
265.1137
279.1218
300.1080
314.1335
326.1331
373.6676
392.8612
%
m/z

f.

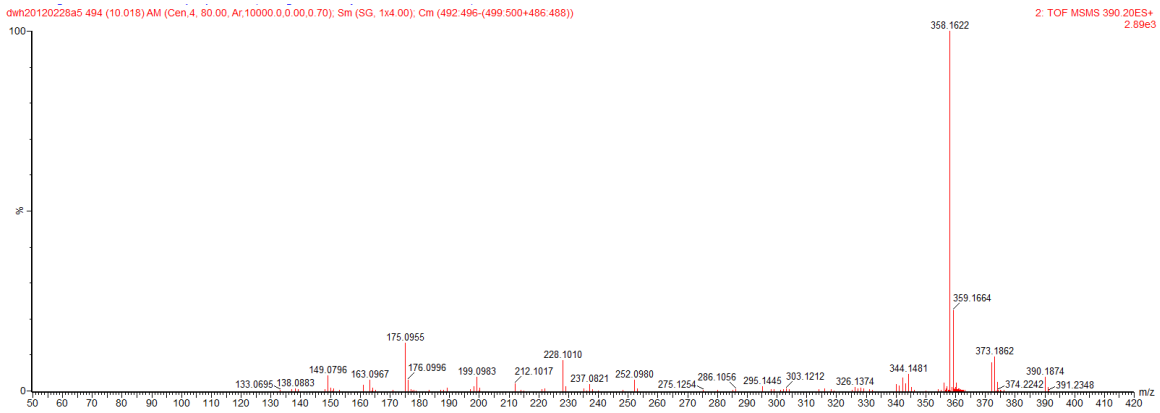
dwh20120228a5 494 (10.018) AM (Cen,4, 80.00, Ar,10000.0,0.00,0.70); Sm (SG, 1x4.00); Cm (492:496-(499:500+486:488))
2: TOF MSMS 390.20ES+
2.89e3
358.1622
359.1664
175.0955
373.1862
228.1010
149.0796
176.0996
163.0967
199.0983
212.1017
344.1481
133.0695
138.0883
237.0821
252.0980
275.1254
286.1056
295.1445
303.1212
326.1374
390.1874
374.2242
391.2348
%
m/z

g.

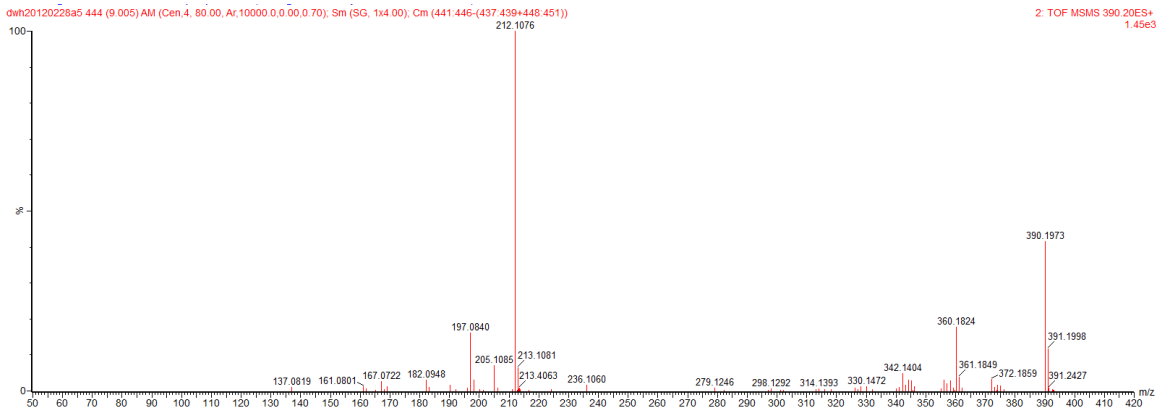

Figure 4. a, MS full scan of compound 10 (UCP1040) and metabolites; b, c, d, e,f, g, MS/MS spectrum of compound 10, M10-1, M10-2, M10-3, M10-4 and M10-5 (shown as Chapter 4, Fig 5.).

Chapter 5.

a.

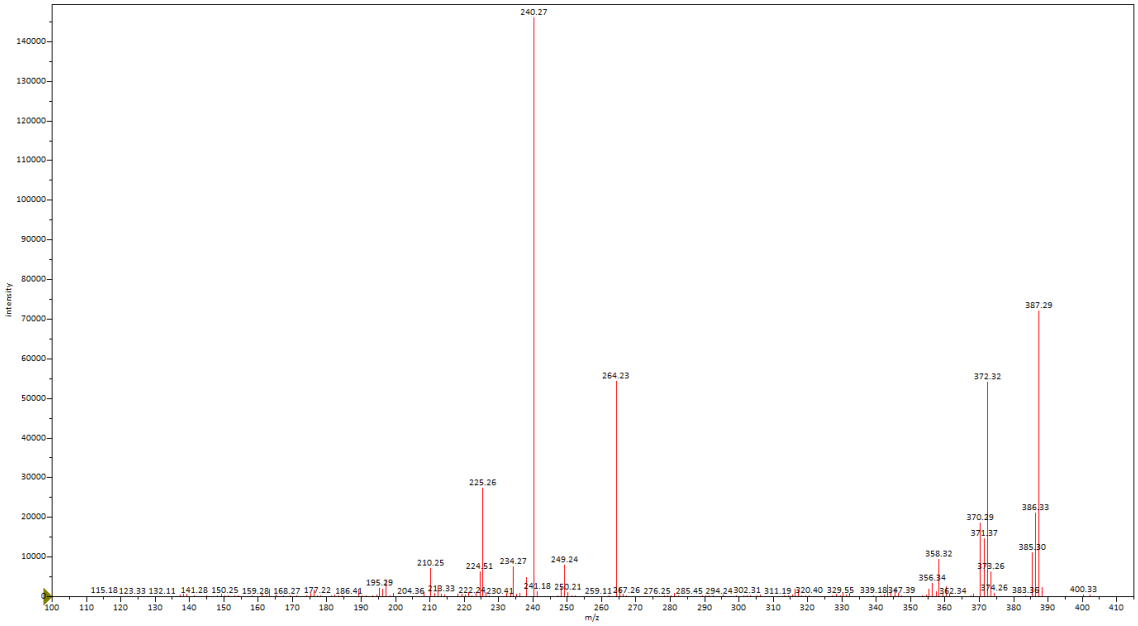
240.27
264.23
225.26
372.32
387.29
386.33
370.29
371.37
385.30
358.32
373.26
356.34
210.25
224.51
234.27
249.24
intensity
m/z

b.

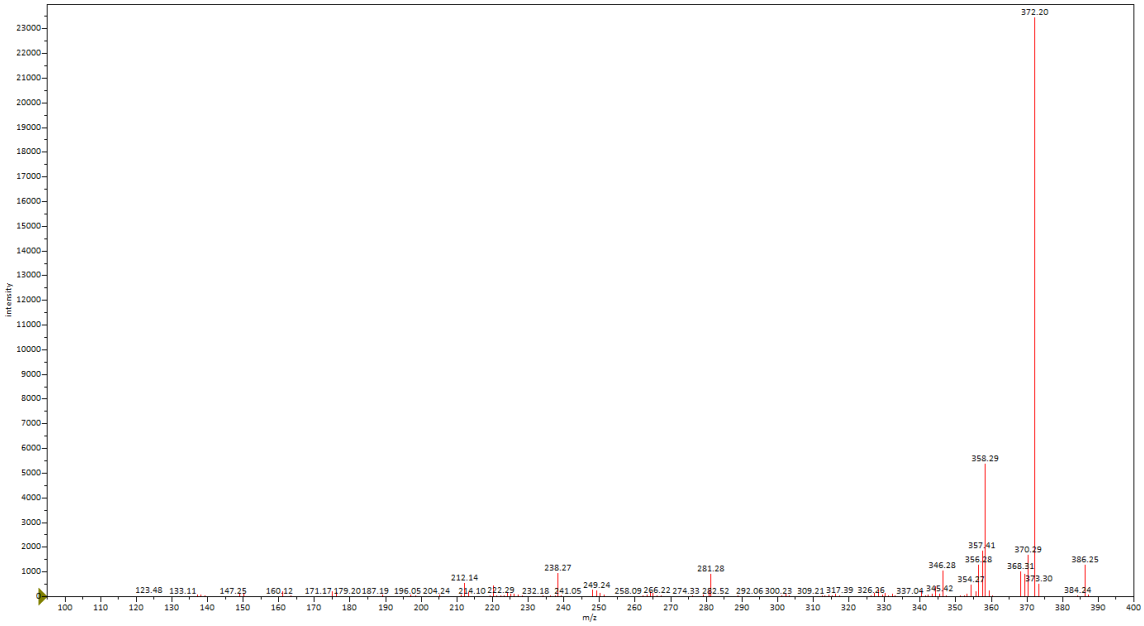
372.20
358.29
357.41
370.29
356.28
386.25
346.28
368.31
354.27
373.30
238.27
281.28
212.14
249.24
intensity
m/z

c.

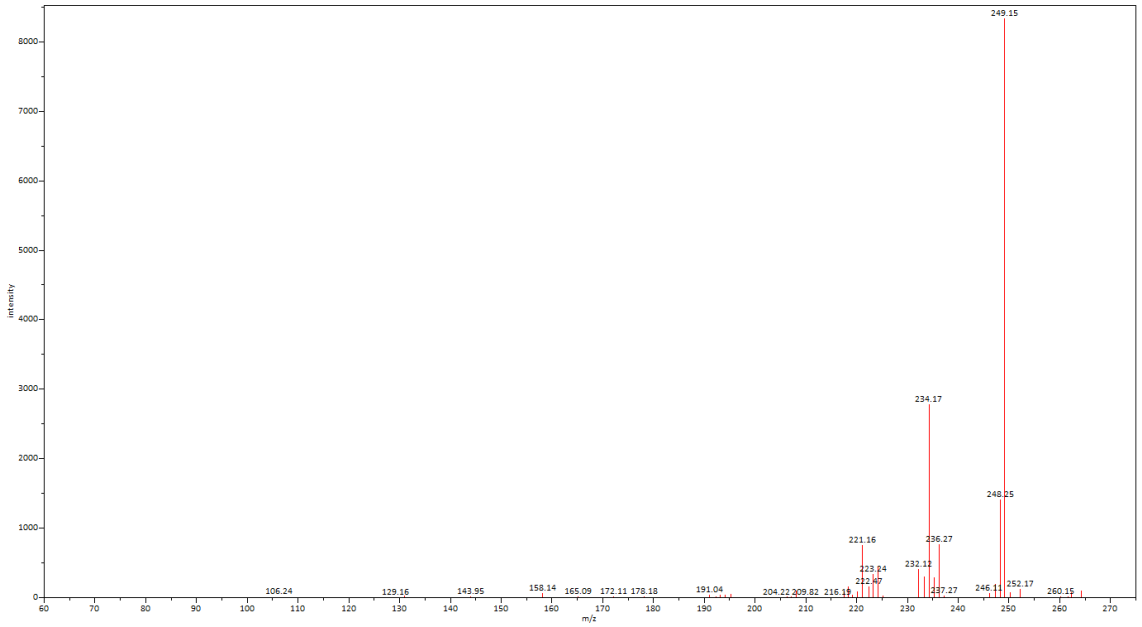

d.

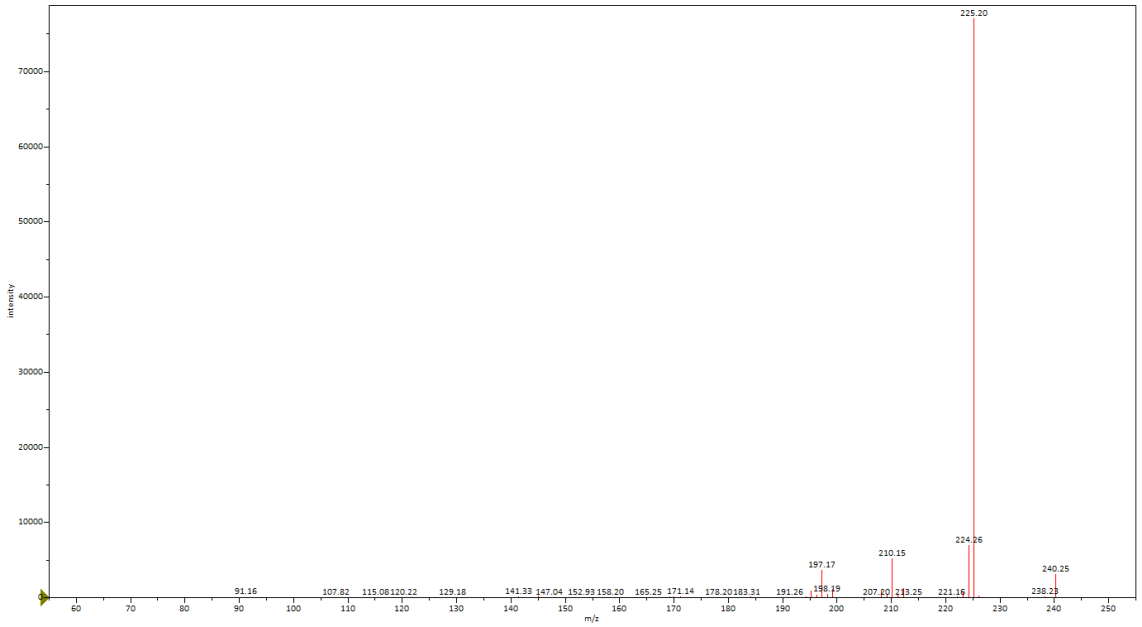

Figure 1. a, MS/MS spectrum of UCP1076; b, c, d, MS^3 spectrum of UCP1076 daughter ions at m/z=387.29, 264.23 and 240.27, respectively.

a.

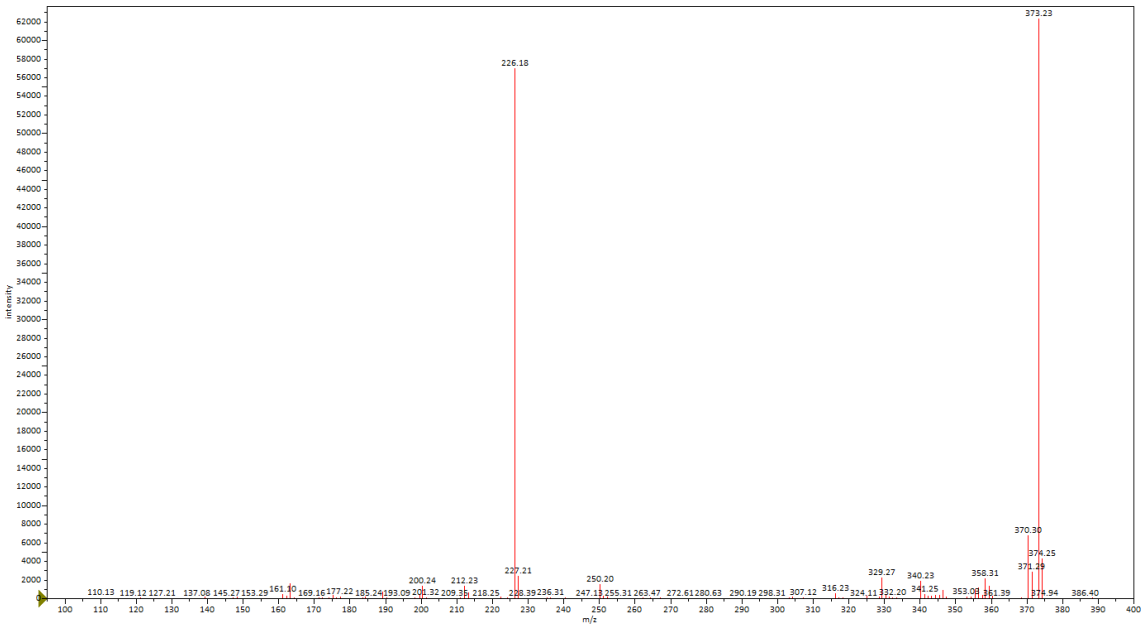
373.23
226.18
370.30
374.25
371.29
intensity
m/z

b.

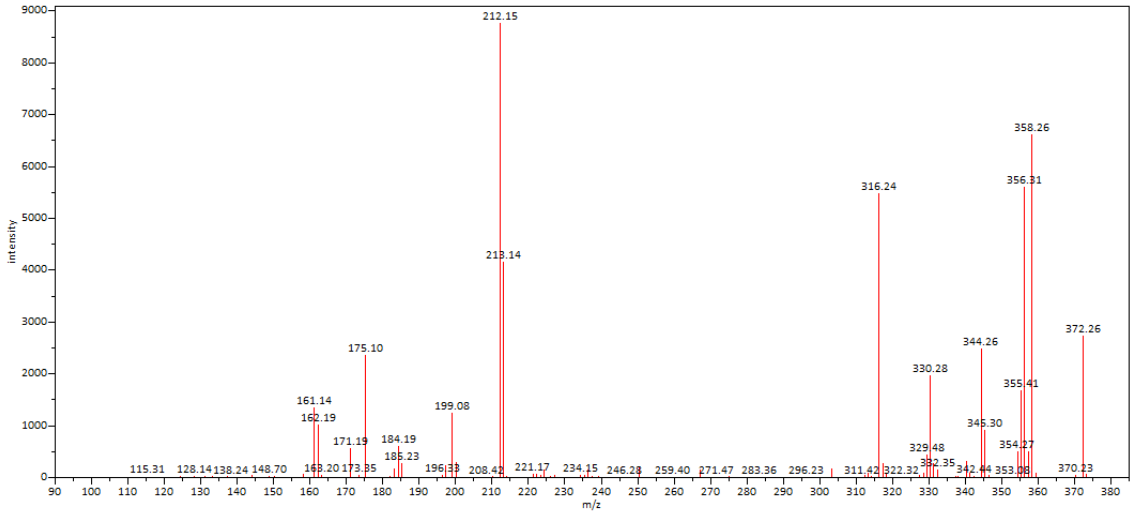
212.15
358.26
356.31
316.24
213.14
372.26
344.26
330.28
355.41
175.10
161.14
162.19
199.08
intensity
m/z

c.

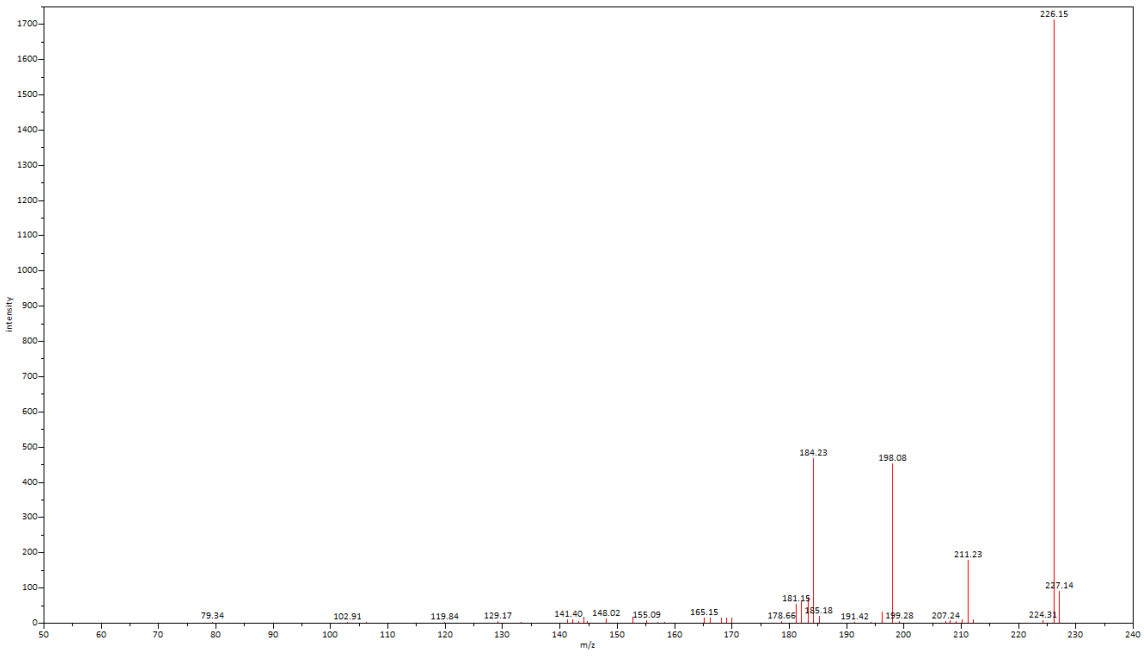

Figure 2. a, MS/MS spectrum of demethylation metabolite of UCP1076; b, c, MS^3 spectrum of daughter ions at m/z=373.22 and 226.18, respectively.

a.

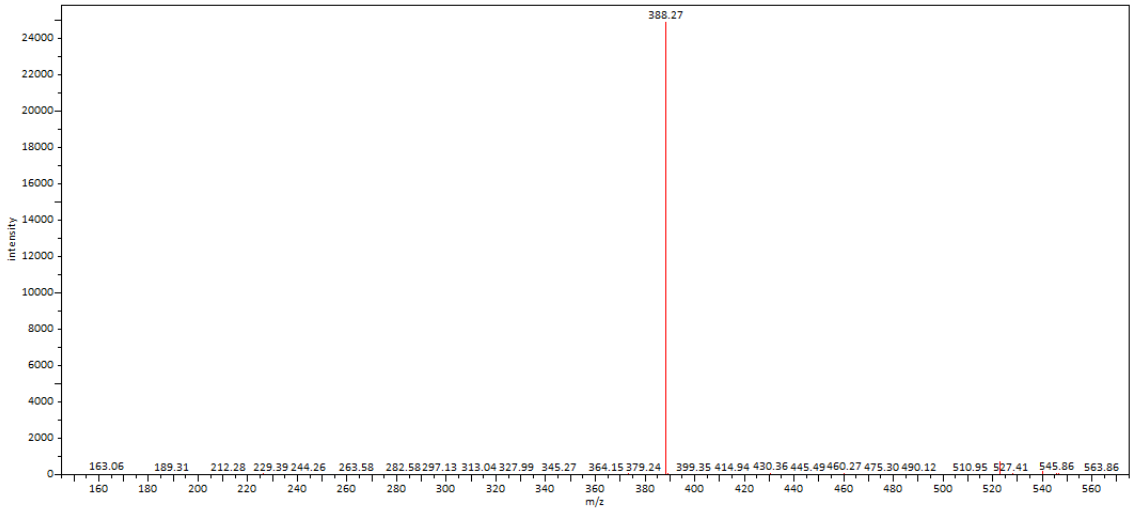

b.

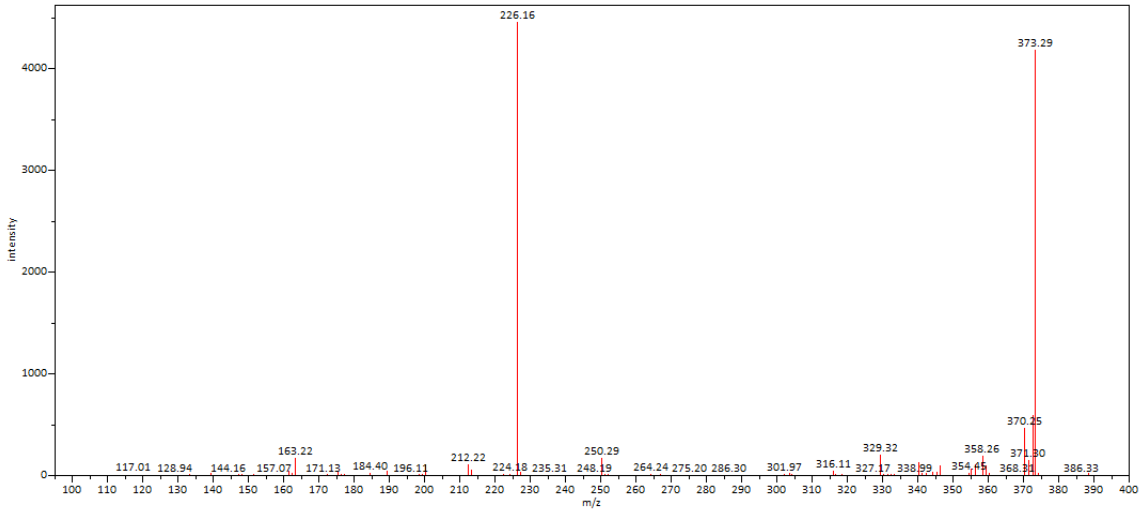

Figure 3. a, MS/MS spectrum of glucuronidation metabolite of UCP1076 (structure shown in Chapter 5. Fig 10); b, MS^3 spectrum of daughter ions at m/z=388.27.